

# Signal Processing for Interventional X-ray-based Coronary Angiography

Signalverarbeitung für die Koronarangiographie

Der Technischen Fakultät  
der Friedrich-Alexander-Universität  
Erlangen-Nürnberg

zur

**Erlangung des Doktorgrades Dr.-Ing.**

vorgelegt von

Mathias Unberath

aus

Zeiden, Rumänien

Als Dissertation genehmigt  
von der Technischen Fakultät  
der Friedrich-Alexander-Universität Erlangen-Nürnberg

Tag der mündlichen Prüfung:

Vorsitzender des Promotionsorgans: Prof. Dr.-Ing. R. Lerch

Gutachter: Prof. Dr.-Ing. habil. A. Maier  
Prof. N. Navab, PhD

## Abstract

Rotational angiography using C-arm scanners enables intra-operative 3-D imaging that has proved beneficial for diagnostic assessment and interventional guidance. Despite previous efforts, rotational angiography was not yet successfully established in clinical practice for coronary artery imaging but remains subject of intensive academic research. 3-D reconstruction of the coronary vasculature is impeded by severe lateral truncation of the thorax, as well as substantial intra-scan respiratory and cardiac motion. Reliable and fully automated solutions to all of the aforementioned problems are required to pave the way for clinical application of rotational angiography and, hence, sustainably change the state-of-care.

Within this thesis, we identify shortcomings of existing approaches and devise algorithms that effectively address non-recurrent object motion, severe angular under-sampling, and the dependency on projection domain segmentations. The proposed methods build upon [virtual digital subtraction angiography \(vDSA\)](#) that voids image truncation and enables prior-reconstruction-free respiratory motion compensation using both [Epipolar consistency conditions \(ECC\)](#) and [auto-focus measures \(AFMs\)](#). The motion-corrected geometry is then used in conjunction with a novel 4-D iterative algorithm that reconstructs images at multiple cardiac phases simultaneously. The method allows for communication among 3-D volumes by regularizing the [temporal total variation \(tTV\)](#) and thus implicitly addresses the problem of insufficient data very effectively. Finally, we consider symbolic coronary artery reconstruction from very few observations and develop generic extensions that consist of symmetrization, outlier removal, and projection domain-informed topology recovery. When applied to two state-of-the-art reconstruction algorithms, the proposed methods substantially reduce problems due to incorrect 2-D centerlines, promoting improved performance. Given that all methods proved effective on the same *in silico* and *in vivo* data sets, we are confident that the proposed algorithms bring rotational coronary angiography one step closer to clinical applicability.

## Kurzfassung

Die Verwendung interventioneller C-Bogen-Systeme ermöglicht die Rekonstruktion intra-operativer 3-D Bilder des Patienten. Diese erlauben Verbesserungen in der Diagnostik und bieten eine klare Orientierungshilfe für kathetergeführte Eingriffe. Trotz einschlägiger Versuche ist es bisher jedoch nicht geglückt, dieses Verfahren in der Koronarangiographie zu etablieren. Grund hierfür sind grundlegende Schwierigkeiten die der Herzbildgebung eigen sind. Diese bestehen zum Einen aus drastischer Trunkierung, und zum Anderen aus stetiger Atem- und Herzbewegung. Für einen erfolgreichen klinischen Einsatz der interventionellen 3-D Koronarbildgebung, müssen zuverlässige und voll automatisierte Lösungen für oben angeführte Probleme gefunden werden.

Wir identifizieren Unzulänglichkeiten derzeitiger Algorithmen und entwickeln Methoden die sich einerseits mit der Bewegungskompensation nicht-periodischer Bewegungsmuster und andererseits mit der 3-D Rekonstruktion beschäftigen. Dabei liegt der Fokus auf der tomographischen Rekonstruktion aus unterabgetasteten Daten, und der symbolischen Rekonstruktion aus unverlässlichen 2-D Segmentierungen. Wir verwenden virtuelle Subtraktionsbildgebung um Trunkierung zu umgehen und schließlich die Anwendung von bildbasierten Qualitätsmaßen, wie der Epipolar Konsistenz oder Autofokus Messungen, zu ermöglichen, welche wiederum die Atembewegungskorrektur ohne Vorwissen erlauben. Anschließend verwenden wir die atembewegungskorrigierte Geometrie zur tomographischen Rekonstruktion mittels eines neuen Algorithmus, der mehrere Herzphasen gleichzeitig rekonstruiert aber Informationsaustausch zwischen den Volumen zulässt, und damit implizit die Unterabtastung geschickt umgeht. Zuletzt widmen wir uns der 3-D Mittellinienrekonstruktion von Koronararterien aus sehr wenigen Ansichten und entwickeln Methoden zur Erweiterung bestehender Rekonstruktionsalgorithmen. Die Erweiterungen beschäftigen sich sowohl mit der Identifikation und Beseitigung von Ausreißern, als auch der Herstellung von Punktkonnektivität, die auf 2-D Mittellinien basiert. Anhand von zwei Methoden, die den Stand der Technik repräsentieren, wird nachgewiesen, dass die Erweiterungen eine Robustheit gegenüber inkorrekten Segmentierungen in 2-D mit sich bringen und damit schlußendlich zu besserer Rekonstruktionsqualität führen.

In Anbetracht der durchweg vielversprechenden Ergebnisse in *in silico* und *in vivo* Studien, sind wir zuversichtlich, dass die hier vorgeschlagenen Methoden einen positiven Einfluss auf die klinische Anwendbarkeit der 3-D Koronarbildgebung haben.



## Acknowledgment

I would like to thank a subset of people that in one way or another supported me during the last two and a half years.

First and foremost, I would like to thank Prof. Dr. Ing. habil. Andreas Maier for his continued support throughout both my Master's and PhD. I am grateful for his trust in my ability to follow research interests independently, knowing that he would provide the necessary guidance and support whenever needed.

Many thanks to Prof. Dr. Nassir Navab for welcoming me in his group and supporting me in finishing this thesis in such a focused manner.

Further, I would like to express my gratitude to Prof. Dr. Stephan Achenbach and Dr. Michaela Hell for providing the clinical data used within this thesis.

I enjoyed our *Herz jours fixes* and would like to thank Dr. Günter Lauritsch for his thought-provoking questions and valuable feedback.

Albeit not directly involved in the work presented here, I would like to thank Dr. Rebecca Fahrig, Dr. Christian Riess, and Prof. Dr. Erica Cherry Kemmerling for providing advice and guidance during my time at Stanford, that I consider an important element in the development of my academic incentive.

Many thanks to the Erlangen Graduate School in Advanced Optical Technologies for funding my PhD fellowship, many conference trips, and my stay at Johns Hopkins. Moreover, I would particularly like to thank Dr. Andreas Bräuer, Christina Ort, and Anja Nelson for providing prompt assistance whenever needed.

I would like to thank André and Oliver for their valuable contributions to many of my publications. Further, I am very fond of my "extended office" namely Tobias, Frank, Oliver, André, Basti, Martin, Jenny, Marco, Jens, Shiyang, Katharina, Lennart, and Bernhard, and would like to thank all of you for fruitful discussions, unexpected office visits, and for making the 9th floor a very enjoyable place to be.

Throughout the last years I have supervised several students that have contributed vastly to research, and I would like to thank them for that.

Finally, I would like to thank my friends and colleagues at CAMP@JHU for welcoming me with warmth and hospitality, and for supporting me in what is yet to come.

People that know me outside of work may know that some of my achievements come at the price of me being cranky. Consequently, I want to express my gratitude towards all of my friends and family, particularly to my wife Iris, who dealt with my nagging and put me back on track.

Many thanks to all of you.

Mathias Unberath



# Contents

<b>Contents</b>	<b>i</b>
<b>Chapter 1 Introduction</b>	<b>1</b>
1.1 Motivation . . . . .	1
1.2 Contributions . . . . .	1
1.2.1 Data Corruption . . . . .	2
1.2.2 Tomographic Reconstruction . . . . .	2
1.2.3 Symbolic Reconstruction . . . . .	3
1.2.4 Other Contributions to Angiography and CBCT Imaging . . . . .	3
1.3 Organization of the Thesis . . . . .	4
<b>Chapter 2 Background and Generic Concepts</b>	<b>7</b>
2.1 Clinical Context . . . . .	7
2.1.1 Cardiac Anatomy and Physiology . . . . .	7
2.1.2 Cardiovascular Disease and Coronary Interventions . . . . .	7
2.2 Rotational Angiography . . . . .	9
2.2.1 Image Formation . . . . .	10
2.2.2 CBCT Imaging Geometry and Reconstruction . . . . .	11
2.3 Reconstruction from Uncorrupted Data . . . . .	14
2.3.1 Filtered Backprojection Based Reconstruction . . . . .	15
2.3.2 Iterative Reconstruction . . . . .	15
2.4 Data Corruption in Coronary CBCT Angiography . . . . .	16
2.4.1 Truncation . . . . .	17
2.4.2 Intra-scan Motion . . . . .	17
2.5 Image-based Data Corruption Metrics . . . . .	19
2.5.1 Epipolar Consistency Conditions . . . . .	19
2.5.2 Auto-focus Measures . . . . .	20
<b>Chapter 3 State-of-the-art in Cardiovascular Imaging</b>	<b>23</b>
3.1 Introduction . . . . .	23
3.2 Truncation . . . . .	23
3.2.1 Background Subtraction . . . . .	23
3.2.2 Background Suppression . . . . .	25
3.3 Cardiac Motion . . . . .	25
3.4 Respiratory Motion . . . . .	27
3.5 Vasculature Reconstruction Algorithms . . . . .	28
3.5.1 Tomographic Reconstruction . . . . .	28
3.5.2 Symbolic Reconstruction . . . . .	29

<b>Chapter 4 Rotational Angiography Data and Preprocessing</b>	<b>33</b>
4.1 Introduction . . . . .	33
4.2 Phantom Data . . . . .	33
4.3 Clinical Data . . . . .	34
4.4 Preprocessing . . . . .	35
4.4.1 Vessel Segmentation and Centerline Extraction . . . . .	35
4.4.2 Background Estimation . . . . .	37
4.5 Experiments . . . . .	38
4.6 Results and Discussion . . . . .	40
4.7 Conclusion . . . . .	40
 <b>Chapter 5 DCM-based Respiratory Motion Compensation</b>	 <b>41</b>
5.1 Introduction . . . . .	41
5.2 Methods . . . . .	41
5.2.1 ECC-based Correction . . . . .	41
5.2.2 AFM-based Correction . . . . .	42
5.2.3 Implementation Details . . . . .	45
5.2.4 Experiments and Evaluation Metrics . . . . .	45
5.3 Results . . . . .	50
5.4 Discussion . . . . .	50
5.5 Conclusion . . . . .	52
 <b>Chapter 6 Tomographic Coronary Artery Reconstruction</b>	 <b>53</b>
6.1 Introduction . . . . .	53
6.2 Methods . . . . .	54
6.2.1 Gating . . . . .	54
6.2.2 Truncation correction . . . . .	54
6.2.3 Limited Grid Size Correction . . . . .	54
6.2.4 Spatially and Temporally Regularized Reconstruction . . . . .	55
6.2.5 Primal-Dual Optimization . . . . .	55
6.2.6 Experiments . . . . .	56
6.3 Results . . . . .	58
6.3.1 Phantom Data . . . . .	58
6.3.2 Clinical Data . . . . .	61
6.4 Discussion . . . . .	61
6.5 Conclusion . . . . .	63
 <b>Chapter 7 Symbolic Coronary Artery Reconstruction</b>	 <b>65</b>
7.1 Introduction . . . . .	65
7.2 Methods . . . . .	66
7.2.1 Gating and Projection Domain Centerline Extraction . . . . .	66
7.2.2 Asymmetric Reconstruction and Challenges . . . . .	66
7.2.3 Symmetrization . . . . .	66
7.2.4 Outlier Removal . . . . .	67
7.2.5 Vascular Tree Extraction . . . . .	67
7.2.6 Pruning . . . . .	69

7.2.7 Experiments . . . . .	70
7.3 Results . . . . .	75
7.4 Discussion . . . . .	77
7.4.1 Phantom Study . . . . .	77
7.4.2 Clinical Data . . . . .	80
7.4.3 Limitations and Challenges. . . . .	80
7.5 Conclusion. . . . .	81
<b>Chapter 8 Outlook</b>	<b>83</b>
<b>Chapter 9 Summary</b>	<b>85</b>
<b>List of Acronyms</b>	<b>89</b>
<b>List of Symbols</b>	<b>93</b>
<b>List of Figures</b>	<b>99</b>
<b>List of Tables</b>	<b>101</b>
<b>Bibliography</b>	<b>103</b>



# Introduction

1.1 Motivation.....	1
1.2 Contributions.....	1
1.3 Organization of the Thesis.....	4

## 1.1 Motivation

To date, C-arm-based X-ray angiography is the workhorse modality for minimally invasive, catheter-based procedures [Wall 08, Orth 08, Klei 11, Cime 16a]. Traditionally, single- or biplane scanners supply 2-D image sequences that are acquired with a static geometry. However, these images suffer from the effects of projective simplification, such as foreshortening and overlapping, that compromise their value for interventional planning and guidance. Direct assessment of the underlying 3-D anatomy is, therefore, considered beneficial [Mess 00, Laur 06, Jand 09, Hett 10, Cime 16a].

It is well known that rotational angiography using motorized C-arm scanners allows for interventional 3-D reconstruction [Siew 05, Fahr 06], yet, its application in clinical practice is limited to largely static anatomies, such as the cerebral [Rooi 08, Boge 16] or hepatic vasculature [Wall 07]. Although 3-D reconstruction in cardiac interventional procedures has received considerable academic attention [Cime 16a], it was not yet successfully established in clinical practice. The reason is, that 3-D reconstruction from rotational acquisitions of the cardiac anatomy is substantially more challenging due to severe corruption by lateral truncation of the thorax, and more importantly, intra-scan cardiac and respiratory motion.

Solutions to some of the aforementioned challenges exist, others have not yet been addressed satisfactorily. Within this thesis, we seek to develop novel, fundamental concepts for some of the open problems in rotational coronary angiography, with a particular focus on respiratory motion compensation.

## 1.2 Contributions

In the course of this thesis, several contributions to the state-of-the-art in respiratory motion correction and vasculature reconstruction from rotational coronary angiography have been made. Many of these contributions are part of publications in national and international conferences but also in well known journals. The main achievements are introduced in the following, accompanied with the corresponding reference to the

literature.

Altogether, the contributions were part of eight journal articles and 21 conference publications, some of which are still in the peer review process.

### 1.2.1 Data Corruption

Vasculature reconstruction from C-arm cone-beam computed tomography (CBCT) rotational angiography is challenging, as the acquisitions are severely corrupted by truncation, and intra-scan respiratory and cardiac motion. To overcome truncation, we propose a **virtual digital subtraction angiography (vDSA) preprocessing pipeline** that separates the contrasted lumen from the truncated background. The proposed method enables the application of **data corruption metrics (DCMs)** that allow for **prior-image-free respiratory motion estimation**. We devise algorithms based on the optimization of **Epipolar consistency conditions (ECC)** and **auto-focus measures (AFMs)** to robustly estimate displacements due to respiration. The methods are detailed in Chap. 4 and Chap. 5, and were presented at three conferences and in a journal article:

- [Unbe 16c] M. Unberath, A. Aichert, S. Achenbach, and A. Maier. “Virtual Single-frame Subtraction Imaging”. In: *Proc. 4th International Meeting on image formation in X-ray Computed Tomography*, pp. 89–92, 2016
- [Unbe 17a] M. Unberath, A. Aichert, S. Achenbach, and A. Maier. “Consistency-based Respiratory Motion Estimation in Rotational Angiography”. *Medical Physics*, 2017. (in press)
- [Unbe 17d] M. Unberath, O. Taubmann, B. Bier, T. Geimer, M. Hell, S. Achenbach, and A. Maier. “Respiratory Motion Compensation in Rotational Angiography: Graphical Model-based Optimization of Auto-focus Measures”. In: *Proc. International Symposium on Biomedical Imaging (ISBI) 2017*, 2017. (to appear)
- [Unbe 17b] M. Unberath, M. Berger, A. Aichert, and A. Maier. “Fourier Consistency-Based Motion Estimation in Rotational Angiography”. In: *Bildverarbeitung für die Medizin 2017*, pp. 110–115, Springer, 2017

### 1.2.2 Tomographic Reconstruction

Strict **electrocardiogram (ECG)-gating** as well as **left ventricle (LV)-twist lead to angular undersampling**, inhibiting straight-forward 3-D reconstruction. We investigate the applicability of a **spatio-temporally regularized 4-D reconstruction model** that effectively handles the substantial undersampling associated with a strict gating setup without the need for cardiac motion compensation. We use both the proposed and a state-of-the-art analytic method to perform **task-based validation**



of aforementioned **DCM-based respiratory motion correction schemes**. Details of the described methods are presented in Chap. 6 and were published in two conference. Moreover, we are currently preparing a journal article that summarizes the results presented in Chap. 5 and Chap. 6.

- [Unbe 15c] M. Unberath, K. Mentl, O. Taubmann, S. Achenbach, R. Fahrig, J. Hornegger, and A. Maier. “Torsional heart motion in cone-beam computed tomography reconstruction”. In: *Proc. International Meeting on Fully Three-Dimensional Image Reconstruction in Radiology Nuclear Medicine*, pp. 651–654, 2015
- [Taub 17c] O. Taubmann, M. Unberath, G. Lauritsch, S. Achenbach, and A. Maier. “Spatio-temporally regularized 4-D Cardiovascular C-arm CT Reconstruction Using a Proximal Algorithm”. In: *Proc. International Symposium on Biomedical Imaging (ISBI) 2017*, 2017. (to appear)
- [Unbe 17c] M. Unberath, O. Taubmann, S. Achenbach, and A. Maier. “Prior-free Respiratory Motion Estimation in Rotational Angiography”. *IEEE Transactions on Medical Imaging*, 2017. (in preparation)

### 1.2.3 Symbolic Reconstruction

In contrast to tomographic methods, symbolic coronary artery centerline reconstruction algorithms are fit to handle severe angular undersampling. However, the performance of such methods critically depends on accurate projection domain centerlines, that are unavailable in practice. We address this shortcoming by proposing **generic postprocessing methods** that consist of **symmetrization**, **removal of inconsistent 3-D points** using the reprojection error, and **projection domain-informed geodesic computation**. A detailed description of the algorithms can be found in Chap. 7. The proposed methods were published as a conference and a journal article:

- [Unbe 16a] M. Unberath, S. Achenbach, and A. Maier. “Exhaustive Graph Cut-based Vasculature Reconstruction”. In: *Proc. International Symposium on Biomedical Imaging (ISBI) 2016*, pp. 1143–1146, 2016
- [Unbe 17e] M. Unberath, O. Taubmann, M. Hell, S. Achenbach, and A. Maier. “Symmetry, Outliers, and Geodesics in Coronary Artery Centerline Reconstruction from Rotational Angiography”. *Medical Physics*, 2017. (under revision)

### 1.2.4 Other Contributions to Angiography and **CBCT** Imaging

A series of contributions to the current state of angiography and **CBCT** literature have been made, that are in close connection to this thesis. The main developments include:

- the organization of *CoronARe*, a Coronary Artery Reconstruction challenge as a satellite event of the 19th International Conference on Medical Image Computing and Computer Assisted Intervention (MICCAI) 2017 [Cime 17].
- a fully automated method for curved and multiplanar reformation of coronary arteries in accelerated magnetic resonance angiography (MRA) [Stim 17a, Stim 17b].
- a fully automated method for deformable respiratory motion compensation in liver perfusion imaging using discrete optimization that is currently in internal revision [Klug 17].
- methods for coronary artery segmentation refinements in 2-D based on consistency conditions (CC) [Unbe 16b] and material decomposition [Lu 15], and in 3-D based on entropy [Unbe 16d].
- a study on artifact propagation due to periodic object motion [Schi 17].
- algorithms for motion compensation and image quality improvements for CBCT imaging of the knee joint under weight-bearing conditions [Unbe 15a, Berg 16, Berg 17, Bier 16, Bier 17a, Bier 17c].
- methods for dense respiratory motion field estimation from low dimensional surrogates [Geim 16, Geim 17a, Geim 17b].

### 1.3 Organization of the Thesis

We will briefly summarize the structure and contents of this thesis, a graphical overview of which is provided in Fig. 1.1.

Chap. 1 provides motivation for the work presented in this thesis, highlights the main contributions to the state-of-the-art, and concludes with a brief outline of the thesis. In Chap. 2, we then provide information on the clinical context including a brief description of the cardiac anatomy, invasive coronary artery imaging, and rotational angiography. This is followed by a revision of X-ray image formation, the imaging geometry, 3-D image reconstruction from uncorrupted acquisitions, and image-based metrics to quantify inconsistencies. Finally, we describe the main sources of sequence corruption, i.e., truncation and intra-scan motion, that will then be addressed in greater detail in the subsequent chapters. We proceed with an in-depth review on the current state-of-the-art in cardiovascular imaging, that can be found in Chap. 3. We present existing solutions to the problems targeted within this thesis, namely truncation removal, respiratory motion compensation, and 3-D tomographic and symbolic reconstruction. This chapter concludes the introductory part.

The methodological section of this thesis begins in Chap. 4, where we present details on the two *in silico* phantom data sets and the three clinical acquisitions that will be used for the evaluation of all proposed methods. Moreover, we describe the common preprocessing pipeline consisting of lumen segmentation, centerline extraction, and background estimation. The chapter is concluded with a qualitative evaluation of the preprocessing algorithms. We then use the preprocessed data as input to

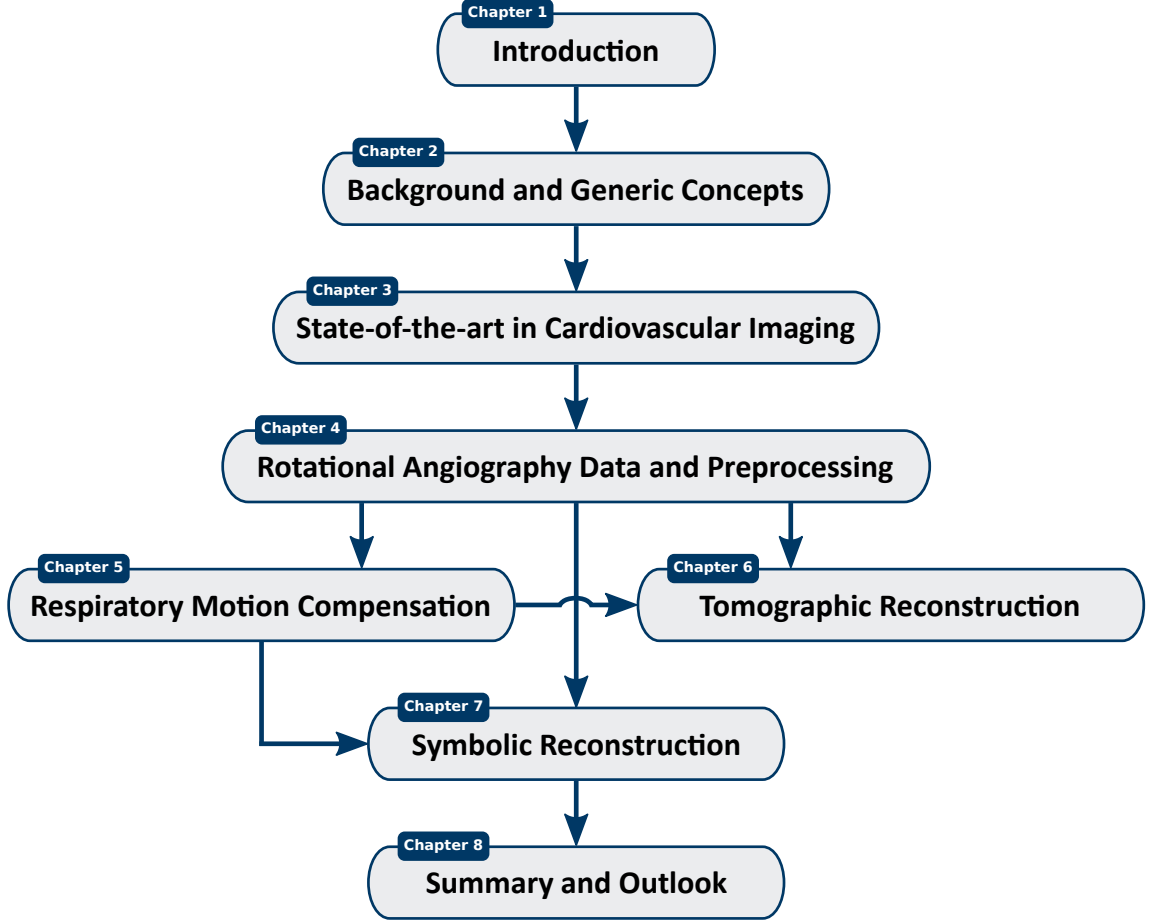


Figure 1.1: Organizational structure of this thesis.

the DCM-based respiratory motion correction methods introduced in Chap. 5. We provide details on the optimization of ECC and AFM, and evaluate the proposed methods quantitatively on both phantom and clinical data based on projection and reconstruction domain errors. Chap. 6 introduces a novel approach to dynamic tomographic reconstruction of cardiac vasculature from rotational angiograms using spatio-temporal regularization. The evaluation assesses reconstruction quality and comprises a comparison to an analytic state-of-the-art method. All experiments are carried out using the results obtained from Chap. 5, a strategy that allows for the task-based evaluation of the proposed respiratory motion compensation schemes. In Chap. 7, we consider symbolic coronary artery reconstruction from projection domain centerlines. Specifically, we address the dependency of these methods on 2-D segmentation quality, a limitation that severely inhibits their practical use. We propose simple yet effective extensions targeting symmetrization, outlier removal, and topology recovery. As the methods are generic, we demonstrate improvements for two state-of-the-art reconstruction algorithms based on explicit and implicit correspondence matching.

The final chapter (Chap. 9) provides an overview of the scientific contributions of the work carried out in this thesis. Finally, we discuss limitations of the presented methods and indicate directions for future research.



# Background and Generic Concepts

2.1 Clinical Context .....	7
2.2 Rotational Angiography.....	9
2.3 Reconstruction from Uncorrupted Data .....	14
2.4 Data Corruption in Coronary CBCT Angiography .....	16
2.5 Image-based Data Corruption Metrics.....	19

## 2.1 Clinical Context

### 2.1.1 Cardiac Anatomy and Physiology

The heart consists of four chambers (left and right atria, and left and right ventricles, respectively) that are compressed by the contraction of the surrounding muscles in the myocardium. Asynchronous contractions of the atria and ventricles results in pressure differences that induce blood circulation through the body (deoxygenation) and the lungs (oxygenation) [Gray 18]. The contractions result from stimulations of the muscles by electric signals that first trigger atrial and subsequently ventricular contraction. The electric signals can be recorded on an ECG and allow for the diagnosis of several pathologies [Romh 68, Hoss 06]. Moreover, the ECG signal provides information about the current cardiac phase (i. e., motion state) during image acquisition, the importance of which will be emphasized later.

The left coronary artery (LCA) and right coronary artery (RCA) run on the surface of the heart, the epicardium, and represent the only source of blood supply to the myocardium. The LCA consists of the left anterior descending artery (LAD) and left circumflex artery (LCX), the anatomy of which is shown in Fig. 2.1. As there is very little redundant blood supply, partial or total occlusion of these vessels is particularly critical.

### 2.1.2 Cardiovascular Disease and Coronary Interventions

Due the vital importance of tissue oxygenation, the consequences of cardiovascular disease (CVD) are devastating. With 17.5 million fatalities in 2012, CVDs are the number one cause of death globally [Worl 16]. Among these, coronary heart disease

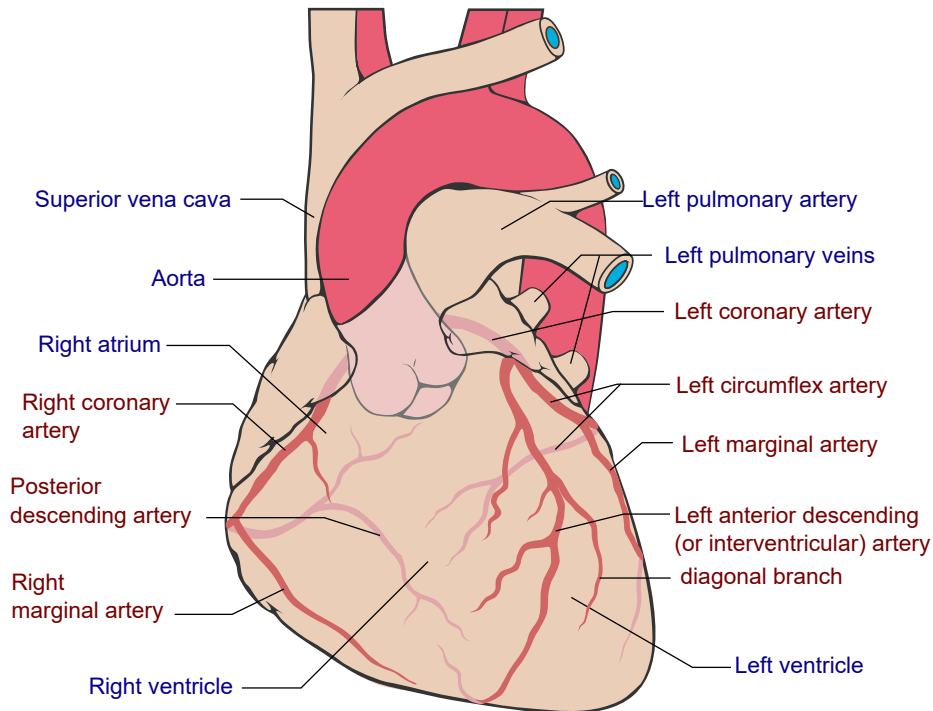


**Figure 2.1:** Schematic illustration of the cardiac anatomy including the coronary arteries. Image taken from [Lync 10].

(CHD) are particularly fatal, as the coronary arteries are critical in ensuring functionality of the circulatory system by supplying the myocardium with oxygenated blood. Consequently, CHD is a primary cause of death and accounted for 7.4 million deaths in 2012 [Worl 16]. CHD is often caused by atherosclerosis that is correlated, among others, with tobacco use, physical inactivity, and obesity [McGi 08, Moza 16]. Atherosclerosis leads to coronary stenosis, which describes the narrowing of the coronary artery lumen due to obstructive lesions (see Fig. 2.2). Partial or total occlusions of the lumen reduces the blood supply of the myocardium and leads to impaired cardiac function. Atherosclerosis is asymptomatic for decades but, once severe, may lead to angina (chest pain), shortness of breath, nausea, and arrhythmias [Nati 16]. Current clinical practice for diagnosis and treatment of CHD is based on cardiac catheterization [Mohr 13]. During percutaneous coronary interventions (PCI) (also referred to as coronary angioplasty), a catheter is inserted into the femoral artery through a sheath and advanced to the ostium of the diseased coronary artery [Land 94]. To detect narrowings of the lumen, an iodine-based solution is injected that selectively contrasts the investigated artery tree. To treat stenoses, a guide catheter is navigated across the stenosis. Once the guide catheter is in place, a deflated balloon catheter is advanced over the wire and positioned at the stenosis. Subsequently, the balloon is inflated with a mixture of saline and contrast agent, thereby dilating the stenosis [Land 94]. Moreover, stents can be introduced to further reduce the risk of re-stenosis and the need for repeated intervention that is associated with balloon angioplasty [Serr 06, Arms 06].

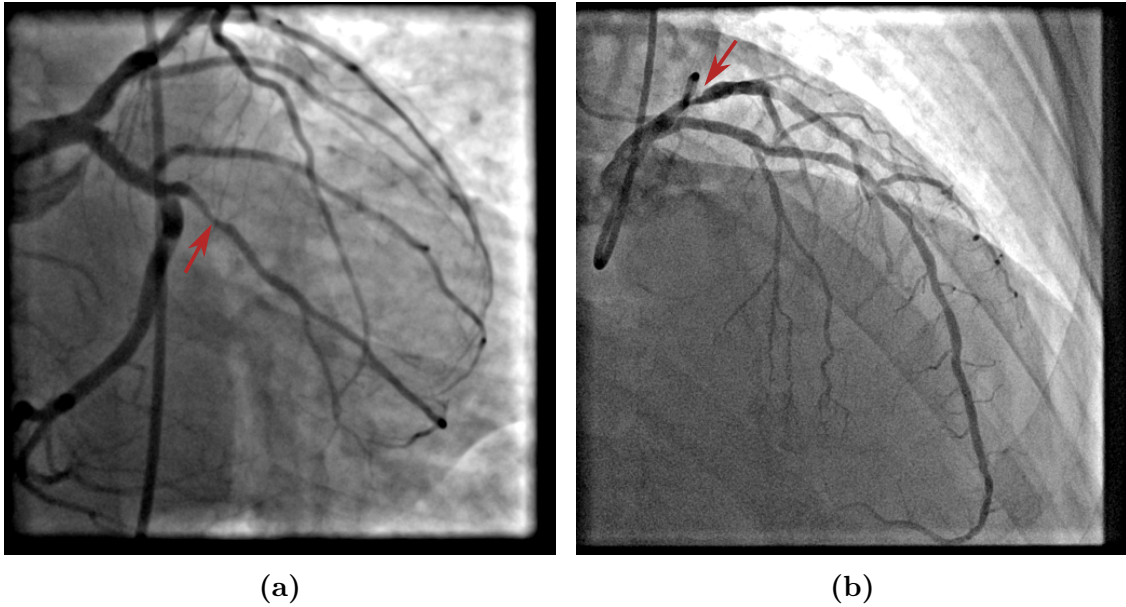


**Figure 2.2:** Traditional 2-D fluoroscopic views of contrasted [LCA](#) trees. Stenoses, i. e., partial occlusions, are highlighted using red arrows. The images exhibit high details but assessment of the tree topology is impeded due to overlap and foreshortening. Clinical data was provided by Dr. med. Michaela Hell and Prof. Dr. med. Stephan Achenbach, Department of Cardiology, Friedrich-Alexander-Universität Erlangen-Nürnberg.

## 2.2 Rotational Angiography

The procedures described in Sec. 2.1.2 are performed using X-ray guidance to confirm the correct positioning of catheters and devices. To this end, physicians rely on single- or biplane C-arm angiography systems that supply 2-D image sequences acquired with a static geometry of the scanner. Exemplary images are shown in Fig. 2.2. Unfortunately, these images suffer from the effects of projective simplification, such as foreshortening and overlapping, that complicate their interpretation [[Andr 08](#)]. Direct assessment of the underlying 3-D anatomy is, therefore, considered beneficial [[Mess 00](#), [Jand 09](#), [Hett 10](#), [Schw 13a](#), [Cime 16a](#)].

To enable tomographic and symbolic 3-D reconstruction, multiple projections from particular viewing directions have to be acquired [[Buzu 08](#), [Zeng 10](#)]. To this end, the C-arm gantry rotates around the patient on a circular orbit while contrast agent is injected into the arteries of interest. Rotational angiography, especially when paired with [digital subtraction angiography \(DSA\)](#), has been particularly successful in cerebrovascular imaging and is today considered clinical state-of-the-art [[Abe 02](#), [Rooi 08](#)]. In the context of cardiac and coronary angiography, however, reconstruction is still subject to intensive academic research [[Cime 16a](#)], as the rotational acquisitions are heavily corrupted by intra-scan motion.

The remainder of this chapter is concerned with the basics of image formation, the [CBCT](#) imaging geometry and standard reconstruction, sources of image sequence



corruption in coronary CBCT angiography, and image-based measures to assess data quality.

## 2.2.1 Image Formation

The concepts presented in the following two sections are based on [Buzu08, Kak01, Zeng10].

### 2.2.1.1 X-ray Photon Generation

In conventional tubes, X-ray radiation is generated by deceleration of electrons, a process that is commonly referred to as *bremssstrahlung*. A filament (the cathode) is heated thereby emitting electrons in thermionic emission. The free electrons are then accelerated towards the anode using an electric field that results from a large potential difference  $U_{\text{Tube}}$  between the cathode and the anode, creating the tube current  $I_{\text{Tube}}$ . When impinging on the anode, the electrons are abruptly decelerated by different scattering processes emitting electromagnetic radiation, i.e., photons, in the process. The energy  $E_P$  of a particular photon is bounded by the tube voltage  $U_{\text{Tube}}$  such that  $0 \leq E_P \leq E_{\text{max}} = e_{\text{Phot}} U_{\text{Tube}}$ , where  $e_{\text{Phot}}$  is the elementary charge. Consequently, modulation of the tube current alters the amount of created photons  $N_0$  of the emitted radiation while modulation of the tube voltage affects the energy distribution  $N_0(E_P)$ .

### 2.2.1.2 Attenuation in Matter

Photons traversing matter are absorbed, scattered, or pass unaffected. These processes are dependent on material properties and the photon energy and attenuate the impinging radiation. The attenuation of a certain object is expressed by its object function  $f(\mathbf{x}, E_P) : \mathbb{R}^{N \times 1} \rightarrow \mathbb{R}$ , where  $\mathbf{x} \in \mathbb{R}^N$  is a point, and  $N$  is the dimension of the object domain. A X-ray beam that propagates through the object on a straight line can be expressed in terms of the X-ray source position  $\mathbf{o} \in \mathbb{R}^N$  and a unit vector  $\mathbf{r} \in \mathbb{R}^N$  that expresses the direction. The number of photons  $N_P$  that pass through the object unaffected is given by Beer-Lambert's law

$$N_P = \int_0^{E_{\text{max}}} N_0(E_P) \left( e^{-\int_0^\infty f(\mathbf{o} + \beta \mathbf{r}, E_P) d\beta} \right) dE_P. \quad (2.1)$$

Eq. (2.1) is commonly referred to as the polychromatic X-ray transform. Most reconstruction algorithms that are currently known in literature assume that the object function  $f(\mathbf{x}, E_P)$  is independent of the photon energy. This allows a less complex description of image formation and, consequently, its inversion. The monochromatic X-ray transform reads

$$N_P = N_0 \cdot e^{-\int_0^\infty f(\mathbf{o} + \beta \mathbf{r}) d\beta}, \quad (2.2)$$

where a fixed energy is assumed implicitly. As polychromatic attenuation is not of particular interest for the work presented in this thesis, we limit our considerations to a monochromatic model.



### 2.2.1.3 Detection

Energy integrating detectors count the number of photons incident on a particular detector pixel. The photon count as such is a relative measure as it depends on the number of emitted photons. Image reconstruction relies on line integrals that only depend on the object function and the imaging geometry. These can be easily obtained from Eq. (2.2) by

$$-\log \frac{N_P}{N_0} = \int_0^\infty f(\mathbf{o} + \beta \mathbf{r}) d\beta. \quad (2.3)$$

Unless stated otherwise, references made to projection and sinogram domain data refer to line integrals rather than photon counts.

## 2.2.2 CBCT Imaging Geometry and Reconstruction

### 2.2.2.1 Mathematical Notation

If not explicitly mentioned otherwise, the following mathematical notation will be used in this thesis. We use upper-case, bold letters (e.g.,  $\mathbf{A} \in \mathbb{R}^{N \times N}$ ) to denote matrices and lower-case, bold letters to denote vectors (e.g.,  $\mathbf{a} \in \mathbb{R}^N$ ). Elements of matrices and vectors are denoted by the same letter but in regular font with a subscript describing the location. As an example,  $A_{i,j}$  corresponds to the element of  $\mathbf{A}$  in the  $i$ -th row and the  $j$ -th column. Lower-case and upper-case, regular font letters (e.g.,  $a \in \mathbb{R}$ ,  $A \in \mathbb{N}_+$ ) can also refer to scalar values, constants, or control variables and will be introduced accordingly. Sets are denoted by upper-case, calligraphic letters (e.g.,  $\mathcal{A}$ ) and images are denoted by upper-case, italic letters (e.g.,  $\mathcal{A}$ ).

Several variables are defined w.r.t. to a certain reference frame that is denoted by a superscript. For example, image  $\mathcal{A}^i$  is the  $i$ -th image in the set of images  $\mathcal{A} = \{\mathcal{A}^j | j = 1, \dots, N\}$ . Moreover, the following notation will be used to define an explicit connection between projection and reconstruction domain points: Given a point on the detector  $\mathbf{a} \in \mathbb{R}^N$ , its reconstruction will be denoted by  $\hat{\mathbf{a}} \in \mathbb{R}^{N+1}$ . Moreover, the reprojection of  $\hat{\mathbf{a}}$  in the detector domain of image  $j$  is denoted by  $\check{\mathbf{a}}^j \in \mathbb{R}^N$ .

Finally, rotation matrices are defined by rational numbers, i.e.,  $\mathbf{R} \in \mathbb{R}^{N \times N}$ . All rotation matrices fulfill  $\mathbf{R}\mathbf{R}^\top = \mathbf{1}_N$ , and  $|\mathbf{R}| = 1$ , where  $\mathbf{1}_N$  is an  $N$ -dimensional identity matrix and  $|\mathbf{R}|$  is the determinant.

### 2.2.2.2 Imaging Geometry

The CBCT geometry and the corresponding X-ray transform have their roots in the parallel-beam geometry that is omitted from this thesis as it is not relevant in practice. Detailed information on connections between parallel-beam, fan-beam and cone-beam geometry can be found in [Buzu 08], [Zeng 10], and [Horn 16].

Fig. 2.3 illustrates the CBCT geometry with a two dimensional flat panel (FP) detector. An X-ray source  $\mathbf{o}$  rotates around the isocenter on a circular trajectory with a source-isocenter-distance (SID) of  $D_{\text{SI}}$ . The detector rotates opposite to the source with a detector-isocenter-distance (DID) of  $D_{\text{DI}}$ . The source-detector-distance (SDD) is given by  $D_{\text{SD}} = D_{\text{SI}} + D_{\text{DI}}$ . The projection image  $\mathcal{I}$  is spanned by the unit

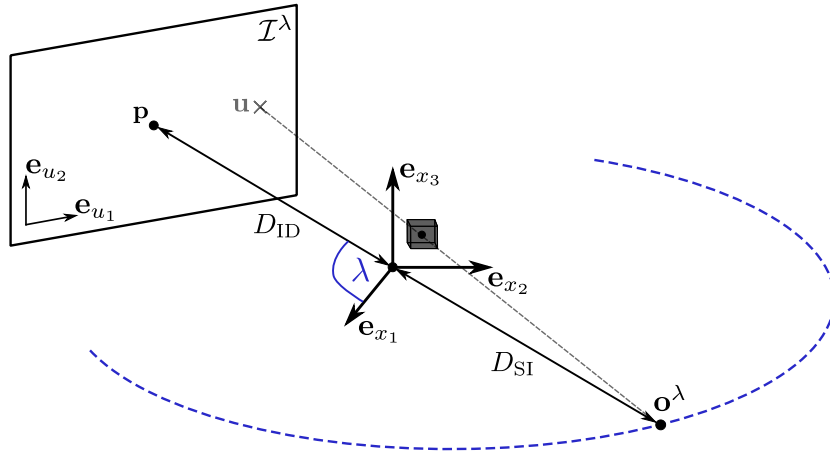


**Figure 2.3:** Schematic representation of the CBCT imaging geometry. The X-ray source rotates around the isocenter on a circular orbit and acquires 2-D projection images  $\mathcal{I}$  at several rotation angles  $\lambda$ .

vectors  $\mathbf{e}_{u_1}$  and  $\mathbf{e}_{u_2}$  in horizontal and vertical direction, respectively. The world coordinate system is spanned by the unit vectors  $\mathbf{e}_{x_1} = (1, 0, 0)^\top$ ,  $\mathbf{e}_{x_2} = (0, 1, 0)^\top$ , and  $\mathbf{e}_{x_3} = (0, 0, 1)^\top$ . We assume, that the principal ray intersects the detector at  $\mathbf{p}^c = (u_1^c = 0, u_2^c = 0)^\top$  and that the rotation axis coincides with  $\mathbf{e}_{x_3}$ . In this case, the cone-beam geometry degenerates to the fan-beam case in the central slice where  $u_2^c = 0$ .

Using aforementioned definitions and given a particular rotation angle  $\lambda$ , the image formation process in cone-beam geometry is defined by the X-ray transform stated in Eq. (2.3):

$$\mathcal{I}^\lambda(\mathbf{u}^c) = \int_0^\infty f(\boldsymbol{\sigma}^\lambda + \beta \mathbf{r}^\lambda(\mathbf{u}^c)) \, d\beta \quad (2.4)$$

$$\boldsymbol{\sigma}^\lambda = -D_{\text{SI}} \cdot \mathbf{R}_{x_3}(\lambda) \cdot \mathbf{e}_{x_1} \quad (2.5)$$

$$\mathbf{r}^\lambda(\mathbf{u}^c) = \mathbf{R}_{x_3}(\lambda + \gamma_f(\mathbf{u}^c)) \cdot \mathbf{R}_{x_2}(\lambda + \gamma_c(\mathbf{u}^c)) \cdot \mathbf{e}_{x_1}, \quad (2.6)$$

where  $\mathbf{R}_{x_3}(\Phi) : \mathbb{R} \rightarrow \mathbb{R}^{3 \times 3}$  and  $\mathbf{R}_{x_2}(\Phi) : \mathbb{R} \rightarrow \mathbb{R}^{3 \times 3}$  yield matrices that describe a rotation of angle  $\Phi$  around the  $\mathbf{e}_{x_3}$  and  $\mathbf{e}_{x_2}$  axis, respectively. Moreover, we made use of the fan-angle  $\gamma_f(\mathbf{u}^c) = \arctan\left(\frac{u_1^c}{D_{\text{SD}}}\right) \in [-\gamma'_f, \gamma'_f]$  and the cone-angle  $\gamma_c(\mathbf{u}^c) = \left(\frac{u_2^c}{D_{\text{SD}}}\right) \in [-\gamma'_c, \gamma'_c]$ .

An angular scan range of  $\lambda \in [0, 2\pi[$  implies a complete scan, where every ray of the central slice is measured exactly twice. In order to obtain a minimal set of views that is still complete, the trajectory must satisfy Tuy's condition [Tuy 83]. It states that the data for a particular object domain point  $\mathbf{x}$  is complete, if all possible planes passing through the respective point intersect the source trajectory at least once. When considering circular trajectories, it can be shown that Tuy's condition can only be satisfied in the central slice but not for off-center slices [Buzu 08, Zeng 10]. To achieve data completeness in the central slice an angular scan range of  $\lambda \in [0, \pi + 2\gamma'_f[$  is

necessary, a trajectory that is commonly referred to as a short scan [Park 82].

### 2.2.2.3 Projection Matrices

The image formation in cone-beam geometry introduced in Sec. 2.2.2 is based on several geometric assumptions, such as the perfect orthogonality of the detector  $u_1$  and  $u_2$  axes or the location of the principal point  $\mathbf{p}$ . Moreover, the relations are given in continuous domain. Unfortunately, neither of aforementioned assumptions are met in real world CBCT scanners. To account for imperfect detector coordinate systems, deviations in the source trajectory, and the finite sampling of both the detector and the angular range, more complex models are needed. Within this thesis, we employ the concepts of projective geometry, i. e., projection matrices and homogeneous coordinates, to describe mappings from 3-D object- to 2-D projection domain. The presented concepts are based on [Hart 04].

As mentioned earlier, both the rotation angle  $\lambda$  as well as the measurement locations along the detector axes  $u_1$  and  $u_2$  are not continuous but discrete. We define  $\Delta\lambda$  as the angular increment, or spacing, between two successive projections, and  $N_\lambda$  denotes the number of projection images. Further, let  $\Delta u_1$  and  $\Delta u_2$  be the pixel spacing and  $U_1$  and  $U_2$  be the number of pixels in detector  $u_1$  and  $u_2$  direction, respectively.

We now introduce homogeneous coordinates that allow for the linearization of projective mappings. Given a point  $\mathbf{a} \in \mathbb{R}^N$ , we define its homogeneous representation by  $\underline{\mathbf{a}} = (\mathbf{a}^\top, 1)^\top \equiv (c\mathbf{a}^\top, c)^\top$  for some non-zero value  $c$ . Aforementioned equivalence relation reveals that points in projective spaces are defined up to scale. When  $\underline{\mathbf{a}}_{N+1} \neq 0$ , the homogeneous mapping can be reverted. We define the transformation  $h(\underline{\mathbf{a}}) : \mathbb{P}^N \rightarrow \mathbb{R}^N$  from projective to Euclidean domain as

$$h(\underline{\mathbf{a}}) = \frac{1}{\underline{\mathbf{a}}_{N+1}} (\underline{\mathbf{a}}_1, \dots, \underline{\mathbf{a}}_N)^\top. \quad (2.7)$$

The inversion is not defined if  $\underline{\mathbf{a}}_{N+1}$  is zero, corresponding to a point at infinity. For the applications of homogeneous coordinates discussed here, it can be ensured that this limitation is not problematic.

Using the homogeneous representation of Euclidean coordinates allows to model the projection from world to detector domain as a simple matrix multiplication. A projection matrix  $\mathbf{P} \in \mathbb{R}^{3 \times 4}$  encodes extrinsic and intrinsic parameters that determine the mapping. The six extrinsic parameters describe the position and orientation of the world coordinate system and consist of a rotation  $\mathbf{R} \in \mathbb{R}^{3 \times 3}$  and a translation  $\mathbf{t} \in \mathbb{R}^3$ , while the five intrinsic parameters determine the mapping  $\mathbf{K} \in \mathbb{R}^{3 \times 3}$  from world to detector coordinate system. The projection matrix incorporating this information is built as

$$\mathbf{P} = \mathbf{K} \begin{pmatrix} 1 & 0 & 0 & 0 \\ 0 & 1 & 0 & 0 \\ 0 & 0 & 1 & 0 \end{pmatrix} \begin{pmatrix} \mathbf{R} & \mathbf{t} \\ \mathbf{o}^\top & 1 \end{pmatrix}. \quad (2.8)$$

The matrix  $\mathbf{K}$  takes the form

$$\mathbf{K} = \begin{pmatrix} \frac{D_{SD}}{\Delta u_1} & k_s & p_1 \\ 0 & \frac{D_{SD}}{\Delta u_2} & p_2 \\ 0 & 0 & 1 \end{pmatrix}, \quad (2.9)$$

where  $k_s$  is a parameter to model skewness between the detector  $u_1$  and  $u_2$  axis, and  $\mathbf{p} = (p_1, p_2)^\top$  denote the location of the principal point in pixel coordinates.

Applying  $\mathbf{R}$  and  $\mathbf{t}$  to the X-ray source  $\mathbf{o}$  yields a configuration where, by definition,  $\mathbf{o}$  is in the world coordinate origin and points in  $\mathbf{e}_{x_3}$  direction [Hart 04]. We seek to adapt the notation presented in Eq. (2.8) to the trajectory definition in Sec. 2.2.2.2, where the initial source location and viewing direction is  $-D_{SI}\mathbf{e}_{x_1}$  and  $\mathbf{e}_{x_1}$ , respectively. To this end, we introduce a rotation matrix  $\mathbf{A} \in \mathbb{R}^{3 \times 3}$  that maps the initial view direction of the X-ray source from  $\mathbf{e}_{x_3}$  to  $\mathbf{e}_{x_1}$  and aligns the  $u_2$ - with the rotation, i.e., the  $\mathbf{e}_{x_3}$ , axis. For a particular viewing angle  $\lambda$ , the rotation and translation to be used in Eq. (2.8) read

$$\mathbf{A} = \begin{pmatrix} 0 & 1 & 0 \\ 0 & 0 & 1 \\ 1 & 0 & 0 \end{pmatrix} \quad (2.10)$$

$$\mathbf{R} = \mathbf{A}\mathbf{R}_{x_3}(\lambda)^\top \quad (2.11)$$

$$\mathbf{t} = \mathbf{A}D_{SI}\mathbf{e}_{x_1} = D_{SI}\mathbf{A}\mathbf{e}_{x_1} = D_{SI}\mathbf{e}_{x_3}. \quad (2.12)$$

In real world applications, the extrinsic and intrinsic camera parameters and, hence, the projection matrices, are determined by a system calibration using dedicated phantoms [Hopp 08, Maie 11, Hart 04].

For the remainder of this thesis, we define the projection matrices  $\mathbf{P}^i$  as the projection matrix corresponding to the primary angle  $\lambda^i = (i - 1) \cdot \Delta\lambda$  with elements  $\mathbf{K}^i$ ,  $\mathbf{R}^i$ , and  $\mathbf{t}^i$ , where  $i = 1, \dots, N_\lambda$ . Projection matrices as defined here map 3-D world coordinates to 2-D detector coordinates  $\mathbf{u} = (u_1, u_2)^\top$  that are expressed in terms of pixels. This is different to the continuous projection domain coordinates  $\mathbf{u}^c = (u_1^c, u_2^c)^\top$  used in Sec. 2.2.2.2 that are stated in mm. They are related by

$$\mathbf{u} = h \left( \mathbf{K} \begin{pmatrix} \mathbf{u}^c \\ D_{SD} \end{pmatrix} \right). \quad (2.13)$$

Projection images  $\mathcal{I}^i(\mathbf{u})$  are discretized on a pixel grid, however, data readout at non-integer, sub-pixel locations is possible via interpolation. If not mentioned otherwise, bilinear interpolation is used [Pras 09, Keck 14].

## 2.3 Reconstruction from Uncorrupted Data

Given a set of images  $\mathcal{I}^i, i = 1, \dots, N_\lambda$  acquired on a short scan trajectory together with the corresponding projection matrices  $\mathbf{P}^i$ . Then, tomographic reconstruction is possible using *filtered backprojection* (FBP) type or iterative reconstruction algorithms, respectively.

### 2.3.1 Filtered Backprojection Based Reconstruction

FBP based methods, such as the well known Feldkamp-Davis-Kress (FDK) algorithm [Feld 84] and its derivatives, are one-shot algorithms and can still be considered the main work horse for tomographic image reconstruction [Zeng 14]. This is particularly true in interventional settings where short run times are critical [Sche 07, Wu 16]. Although most one-shot algorithms, including the FDK algorithm, are known to be approximate for circular trajectories (see also Sec. 2.2.2.2) [Feld 84, Zeng 10, Sidk 08], they perform adequately well when the cone-angle is small and there are a large number of projections [Sidk 08].

Using the projection matrices, FBP type reconstruction reads

$$\underline{u} = \mathbf{P}^i \underline{x} \quad (2.14)$$

$$f(\underline{x}) = \sum_{i=1}^{N_\lambda} \frac{1}{(\underline{u}_3)^2} w_{\text{red}}^i(\underline{u}) \cdot \widetilde{\mathcal{I}}^i(h(\underline{u})) , \quad (2.15)$$

where we exploit the convenient property that  $\underline{u}_3$  encodes the depth of  $\underline{x}$  w.r.t. the X-ray source and the principal ray. This property depends on the scaling of the projection matrix and the encoded view direction, but holds for the definition of  $\mathbf{P}$  presented here [Hart 04]. Moreover,  $w_{\text{red}}^i$  are redundancy weights that account for multiple sampling of particular rays [Park 82, Ries 13], and  $\widetilde{\mathcal{I}}^i$  is the projection image after cosine weighting [Kak 01] and row-wise ramp filtering [Rama 71, Kak 01].

### 2.3.2 Iterative Reconstruction

When the projection data is sufficient, one-shot algorithms derived from analytic inversion formulas are usually effective [Sidk 08]. When data is incomplete, e. g., under-sampled, such algorithms may implicitly impose unrealistic assumptions resulting in severe artifacts in the reconstructed images [Chen 08, Sidk 06, Sidk 08, Ries 13]. Conversely, iterative algorithms make weaker assumptions on missing data and allow for the incorporation of prior knowledge in the form of regularizers targeting positivity constraints or image appearance. Many iterative algorithms model the reconstruction problem as a discrete linear system, where the projection data is understood as a weighted sum over the image voxels:

$$\mathcal{I} = \mathbf{M} \mathbf{f} , \quad (2.16)$$

where  $\mathcal{I} \in \mathbb{R}^{(N_u \cdot N_\lambda)}$  and  $\mathbf{f} \in \mathbb{R}^{N_x}$  are discrete, vectorized versions of the set of projection images  $\{\mathcal{I}^i\}$  and the object function  $f$ , respectively. Further,  $N_u = U_1 \cdot U_2$  and  $N_x = X_1 \cdot X_2 \cdot X_3$  are the number of discrete samples in a projection image and the reconstruction volume. The system matrix  $\mathbf{M}$  encodes the geometry and is a discrete model for Eq. (2.1) and Eq. (2.3). Inverting Eq. (2.16) is impossible even under ideal conditions due to the sheer size and ill-conditionedness of  $\mathbf{M} \in \mathbb{R}^{(N_u \cdot N_\lambda) \times N_x}$  that arises from, e. g., under-sampling. However, from Eq. (2.16) we can specify an optimization problem that is then solved in an iterative procedure. The minimization problem is given by

$$\underset{\mathbf{f}}{\operatorname{argmin}} D(\mathbf{f}) + R(\mathbf{f}) , \quad (2.17)$$

where  $D(\mathbf{f})$  is a data fidelity term and  $R(\mathbf{f})$  may encode additional regularizers [Sidk 08, Cond 14].

We chose the squared residual  $D(\mathbf{f}) = \frac{1}{2} \|\mathbf{M}\mathbf{f} - \mathcal{I}\|_2^2$  as the data fidelity term. Typically, the regularization terms consist of a non-negativity constraint  $\iota_{\mathbb{R}_+}(\mathbf{f})$  and the spatial total variation (sTV) norm  $\|\mathbf{f}\|_{\text{sTV}}$  [Song 07, Chen 08, Sidk 08, Rits 11, Huan 16, Taub 16]. The sTV norm  $\|\mathbf{f}\|_{\text{sTV}} = \|\mathbf{D}_s \mathbf{f}\|_{1,2}$  is defined as the sum ( $L^1$  norm) of the magnitudes ( $L^2$  norm) of the spatial image gradient that is computed using

$$\mathbf{D}_s : f_{x_1, x_2, x_3} \mapsto \begin{bmatrix} f_{x_1+1, x_2, x_3} - f_{x_1, x_2, x_3} \\ f_{x_1, x_2+1, x_3} - f_{x_1, x_2, x_3} \\ f_{x_1, x_2, x_3+1} - f_{x_1, x_2, x_3} \end{bmatrix}, \quad (2.18)$$

the element-wise spatial forward difference operator and zero boundary conditions. For brevity of notation,  $f_{x_1, x_2, x_3}$  denotes the element of  $\mathbf{f}$  at location  $\mathbf{x} = (x_1, x_2, x_3)^\top$ . Then, the target function for reconstruction becomes

$$\underset{\mathcal{I}}{\operatorname{argmin}} = \frac{1}{2} \|\mathbf{M}\mathbf{f} - \mathcal{I}\|_2^2 + \mu_s \|\mathcal{I}\|_{\text{sTV}} + \iota_{\mathbb{R}_+}(\mathcal{I}), \quad (2.19)$$

where  $\mu_s \geq 0$  is the regularizer weight.

Many strategies have been proposed for the optimization of Eq. (2.19) [Song 07, Sidk 08]. Recently, convex optimization methods involving variable splitting and proximal operators have received increasing attention due to their desirable convergence properties [Cham 11, Taub 17a]. Eq. (2.19) consists of a smooth, differentiable part  $D(\mathbf{f})$  but also of non-smooth but proximable parts, a type of function that is ideally suited for optimization using the proximal primal-dual split algorithm [Cond 13] that was later refined to efficiently tackle regularized imaging problems [Cond 14]. Put concisely, the algorithm iteratively finds the optimal solution for  $\mathbf{f}$  (in primal domain) and  $\mathbf{D}_s \mathbf{f}$  (in dual domain), respectively, using alternating updates. We refer to Chap. 6 and [Cond 13, Cond 14] for a more detailed discussion of the optimization strategy. As mentioned previously, minimization of Eq. (2.19) using [Cond 14, Algorithm 1] is guaranteed to converge if the update step lengths are chosen appropriately.

## 2.4 Data Corruption in Coronary CBCT Angiography

Both one-shot and iterative reconstruction algorithms as described in Sec. 2.3 have been successfully applied to various reconstruction problems in C-arm CBCT imaging. However, they assume consistent input data. This means, that a) all images  $\mathcal{I}$  are projections of the same, static object that b) does not extend beyond the field of view (FOV) defined by the accurately known acquisition geometry [Ohne 00]. Unfortunately, neither of the two aforementioned requirements is met in rotational coronary angiography, as will be discussed in the following sections.

It is worth mentioning, that other effects such as beam hardening [Broo 76], photon starvation [Barr 04], and scatter [Zbij 06, Bier 17b] also tend to result in inconsistent projection data, but are neglected within this thesis as inconsistencies introduced by imaging of dynamic objects and heavy truncation are predominant.

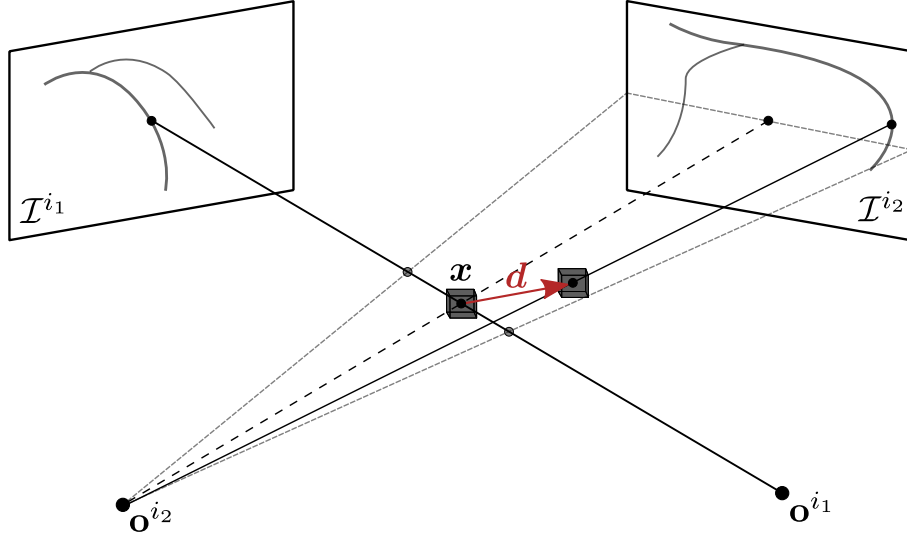


**Figure 2.4:** Illustration of intra-scan motion between two subsequent projection images  $\mathcal{I}^{i_1}$  and  $\mathcal{I}^{i_2}$ . The world point  $x$  is displaced by  $d$  between the acquisition of images  $i_1$  and  $i_2$ . Such displacements corrupt the acquisition by introducing inconsistencies that need to be accounted for during reconstruction.

### 2.4.1 Truncation

Angiography scanners are operated during interventions and, therefore, cannot be fitted with very large detectors as they would obstruct access to the patient and could lead to high radiation doses [Maie12]. Conventionally, active detector sizes are limited to  $382\text{ mm} \times 296\text{ mm}$  with typical values for SID and SDD being 785 mm and 1200 mm [Siem14]. For reconstruction, this geometry results in a cylindrical 3-D FOV with a diameter of 240 mm and a height of 185 mm [Siem17].

As the FOV clearly is too small to accommodate the whole thorax of an adult, projection images of the thorax acquired using a short scan trajectory (see Sec. 2.2.2.2) are truncated. The average heart is 120 mm in length, 80 mm in width, and 60 mm in height [Bett13, pp. 787–846]. Consequently, the heart and particularly the coronary arteries do not extend beyond the central FOV and are, therefore, not truncated. This observation will be of particular importance in later sections.

### 2.4.2 Intra-scan Motion

Assuming that projections arise from a static scene is justified for certain imaging problems, e. g., for cerebrovascular rotational angiography [Rooi08] or supine CBCT scanning of extremities [Choi14, Berg16]. In most cases, however, at least parts of the imaged object are dynamic. If intra-scan motion occurs the acquired projection images do not agree with the calibrated geometry, which leads to artifacts in uncompensated reconstructions [Rit09b, Rohk10b, Schw13a, Siss16b]. A schematic of these relationships is shown in Fig. 2.4.

Intra-scan motion is of particular relevance when imaging the thoracic region, due to constant cardiac and respiratory motion [Wang99, Shec06].



**Table 2.1:** Maximum displacements of landmarks on the two main branches (left anterior descending artery (LAD) and left circumflex artery (LCX)) of the LCA in left-right (L-R), posterior-anterior (P-A), and superior-inferior (S-I) direction taken from [Shec 06]. Positive values indicate motion towards the left, posterior, and superior, respectively.

	L-R	P-A	S-I
LAD	$(0.1 \pm 3.5) \text{ mm}$	$(-0.7 \pm 1.9) \text{ mm}$	$(4.7 \pm 1.8) \text{ mm}$
LCX	$(0.3 \pm 2.8) \text{ mm}$	$(-0.6 \pm 1.9) \text{ mm}$	$(5.6 \pm 1.5) \text{ mm}$

#### 2.4.2.1 Cardiac Motion

Cardiac motion is highly complex but repetitive with a high frequency. Resting state heart rates are between 60 and 100 beats per minute (bpm) (1.0 Hz to 1.7 Hz) [Guyt 11, Ostc 11] which suggests that 5.0 to 8.3 recurrences are observed within a standard 5 s short scan. The coronary arteries are attached to the myocardial surface and, therefore, follow cardiac movement. The motion consists of longitudinal and circumferential contraction, and twist around the LV long axis [Naka 11, Unbe 15c]. Typical 3-D displacements for landmarks on the LAD and the LCX during the cardiac cycle are  $(9.6 \pm 1.3) \text{ mm}$  and  $(12.1 \pm 2.4) \text{ mm}$ , respectively [Shec 06]. In general, this motion is oriented towards the patient’s left inferior and anterior [Shec 06] but it is highly non-rigid.

#### 2.4.2.2 Respiratory Motion

In contrast to cardiac motion, respiratory motion is low frequency. The average ventilation rate among elderly adults is  $(0.33 \pm 0.08) \text{ Hz}$  [Rodr 13], suggesting that respiratory motion is quasi non-recurrent for standard interventional imaging protocols [Rohk 10b, Unbe 16c, Unbe 16c]. Displacement of the coronary arteries during tidal breathing occurs mostly along the superior-inferior axis of the patient as the pericardium, a conical fibro-serous sac containing the myocardium, is attached to the diaphragm [Gray 18] and, therefore, largely follows diaphragm motion [Wang 95, Shec 04, Shec 06]. Maximum displacements of the LAD and the LCX in left-right (L-R), posterior-anterior (P-A), and superior-inferior (S-I) direction are stated in Tab. 2.1. The form of presentation in Tab. 2.1 suggests that respiratory motion induced displacements of the coronary arteries are sufficiently described by a single 3-D translation. However, there is evidence that more flexible motion models need to be considered if a very accurate description is needed [Shec 04], particularly, when a larger region of the thorax is of interest [McCl 13, Geim 17b].

#### 2.4.2.3 Conclusion

In conclusion, the corruption due to cardiac and respiratory intra-scan motion is substantial and cannot be neglected during reconstruction due to large motion amplitudes. Moreover, unfortunate combination of cardiac and respiratory motion patterns may yield situations where a certain motion state is imaged only once. These



observations suggest the need for motion detection and management strategies to enable 3-D reconstruction.

## 2.5 Image-based Data Corruption Metrics

As motivated in Sec. 2.4, the sources of image sequence corruption and the respective severity is highly diverse. While inconsistencies due to scatter are largely neglected in practice, corruption resulting from patient motion tends to render 3-D reconstruction impossible. Consequently, metrics that quantify the level of corruption, i. e., inconsistencies, within an acquisition are of high relevance.

We categorize DCMs in two categories.

1. DCMs that arise from the image formation process and geometry. These DCMs are often referred to as CC. Famous representatives include:
  - Helgason-Ludwig consistency conditions (HLCC) [Helg 80, Ludw 66],
  - Fourier consistency conditions (FCC) [Edho 86, Natt 86, Mazi 10, Berg 17], and
  - Epipolar consistency conditions (ECC) [Debb 13, Maas 14, Aich 15a, Frys 15].
2. DCMs that assess image characteristics based on prior knowledge of favorable properties, often referred to as an auto-focus measure (AFM). These DCMs are heuristic but prove effective in practice. Favorable characteristics include:
  - Gabor texture features [Wick 12],
  - Gradient magnitudes, such as sTV and temporal total variation (tTV) [Wick 12, Sisin 16a, Taub 17a], and
  - Histogram entropy [Wick 12, Sisin 16a].

Using CC for the assessment of inconsistencies seems convenient, as they do not impose any assumptions on the imaged object. Unfortunately, Helgason-Ludwig consistency conditions (HLCC) have not yet been extended to the CBCT geometry, and Fourier consistency conditions (FCC) require a full scan [Berg 17] that is not available in practice. Consequently, the focus within this thesis is on ECC and AFMs as they are fit to handle clinical CBCT acquisitions.

### 2.5.1 Epipolar Consistency Conditions

ECC builds upon the epipolar geometry, that describes the geometric relation between two views  $i_1$  and  $i_2$ , where  $i_{1/2} \in \{1, \dots, N_\lambda\}$  and  $i_1 \neq i_2$ . The epipolar geometry allows for the definition of corresponding lines  $\underline{l}_{i_1}^{i_2}$  and  $\underline{l}_{i_2}^{i_1}$  in the images  $\mathcal{I}^{i_1}$  and  $\mathcal{I}^{i_2}$ , respectively. The lines arise from the intersection of a particular epipolar plane  $\underline{e}_{i_1}^{i_2} \in \mathbb{R}^4$ , which is a homogeneous 3-vector, with the two image planes. A schematic of the described relations is given in Fig. 2.5. The resulting lines in the domain of the respective images are defined by a signed distance  $t$  to the principal point and an angle  $\beta$  measured with respect to the  $u_1$  axis, such that  $\underline{l} = (-\sin(\beta), \cos(\beta), -t)^\top$ .

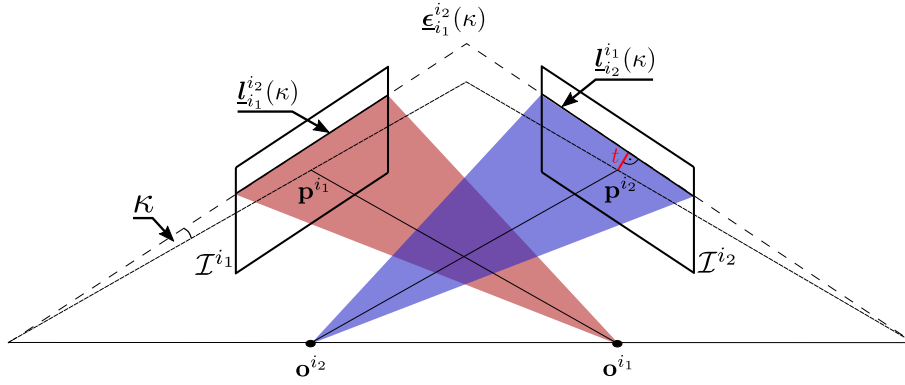


**Figure 2.5:** Schematic drawing of the geometric relations between two calibrated views  $i_1$  and  $i_2$ . The epipolar lines  $\underline{l}_{i1}^{i2}$  and  $\underline{l}_{i2}^{i1}$  are the intersections of an epipolar plane  $\underline{\epsilon}_{i1}^{i2}$  with the respective image plane.

Assuming an orthogonal acquisition geometry, integration over corresponding epipolar lines  $\underline{l}_{i1}^{i2}$  and  $\underline{l}_{i2}^{i1}$  gives two redundant ways of computing the integral over the epipolar plane  $\underline{\epsilon}$  through the 3-D object. It holds

$$\rho_{i1}(\underline{l}_{i1}^{i2}) - \rho_{i2}(\underline{l}_{i2}^{i1}) = 0, \quad (2.20)$$

where  $\rho_i(\underline{l}_i)$  denotes integration over the line  $\underline{l}_i$  in image  $\mathcal{I}^i$ .

For cone-beam projections aforementioned equality does not apply as integrals over epipolar lines differ by a weighting with the distance to the camera center [Aich 15a]. Yet, they carry redundant information. Aichert et al. use Grangeat's theorem to cancel out the weighting and derive consistency conditions similar to Eq. (2.20) for cone-beam geometries:

$$\frac{\partial}{\partial t} \rho_{i1}(\underline{l}_{i1}^{i2}) - \frac{\partial}{\partial t} \rho_{i2}(\underline{l}_{i2}^{i1}) \approx 0. \quad (2.21)$$

In Eq. (2.21),  $t$  is the distance of the line to the principal point. There exists a pencil of epipolar planes  $\underline{\epsilon}_{i1}^{i2}(\kappa)$  around the baseline, where  $\kappa$  is the angle of the epipolar plane and the principal ray, and the baseline is the join of the two camera centers [Aich 15a]. This allows for the definition of a global metric EC that quantifies overall sequence corruption. The measure is obtained by summation over all ordered image pairs:

$$\begin{aligned} \text{EC}(\{\mathcal{I}^i\}) &= \sum_{i_1=1}^{N_\lambda} \sum_{i_2 < i_1} \text{EC}_{i_1}^{i_2}(\mathcal{I}^{i_1}, \mathcal{I}^{i_2}) \\ &= \sum_{i_1=1}^{N_\lambda} \sum_{i_2 < i_1} \int_{-\pi/2}^{\pi/2} \left( \left( \frac{\partial}{\partial t} \rho_{i_1}(\underline{l}_{i_1}^{i_2})(\kappa) \right) - \left( \frac{\partial}{\partial t} \rho_{i_2}(\underline{l}_{i_2}^{i_1})(\kappa) \right) \right) d\kappa, \end{aligned} \quad (2.22)$$

where  $\kappa$  is still considered continuous.

## 2.5.2 Auto-focus Measures

**Auto-focus Measures (AFMs)** can be considered an image optimality criterion that, in contrast to traditional CC, does not immediately follow from the image formation

process. The term auto-focus is most commonly used in the context of digital photography, where an image-based measure is evaluated locally to determine whether an object of interest is in or out of focus. However, such measures have received increasing attention in medical imaging as they map an image to a single scalar value that represents the quality of the image [Wick 12, Mir 14]. To do so, AFM exploit prior knowledge of the imaged object. Popular measures, both in photography and medical imaging, are based on gradient magnitudes or properties of the gray value histogram [Wick 12, Mir 14, Mari 16, Siss 16a, Unbe 17d] and favor piecewise constant images. For the remainder of this thesis, we denote the scalar describing the focus of an image  $f$  by  $AF(f)$ .



# State-of-the-art in Cardiovascular Imaging

3.1	Introduction .....	23
3.2	Truncation .....	23
3.3	Cardiac Motion .....	25
3.4	Respiratory Motion .....	27
3.5	Vasculature Reconstruction Algorithms .....	28

## 3.1 Introduction

This chapter provides information on the current state-of-the-art in vasculature reconstruction from C-arm CBCT rotational angiography. We focus on related work targeting the major sources of corruption in coronary angiography, namely truncation (Sec. 3.2), intra-scan motion (Sec. 3.3 and Sec. 3.4), and 3-D reconstruction from very few consistent views (Sec. 3.5).

## 3.2 Truncation

Truncation correction has been studied intensively in the context of CBCT image reconstruction [Sour05, Maie12, Denn13, Xia14, Xia15]. Many of these methods seek to mitigate the effects of lateral truncation by clever decomposition of the standard FDK algorithm [Feld84, Denn13, Xia15]. Despite effective for CBCT reconstruction, aforementioned algorithms cannot be employed within this thesis, as we explicitly require non-truncated projection images to enable the application of CCs.

### 3.2.1 Background Subtraction

As mentioned previously, projections of the whole thorax are truncated as it extends far beyond the 3-D FOV of conventional clinical C-arm angiography systems. The coronary arteries, however, occupy a central region of interest (ROI) only and thus do not extend beyond the FOV implying that separation of the contrasted coronary arteries from the remaining thorax would yield non-truncated projections.

A straight-forward method to achieve material decomposition in projection domain is background removal via digital subtraction [Chil81]. For DSA, projections of the

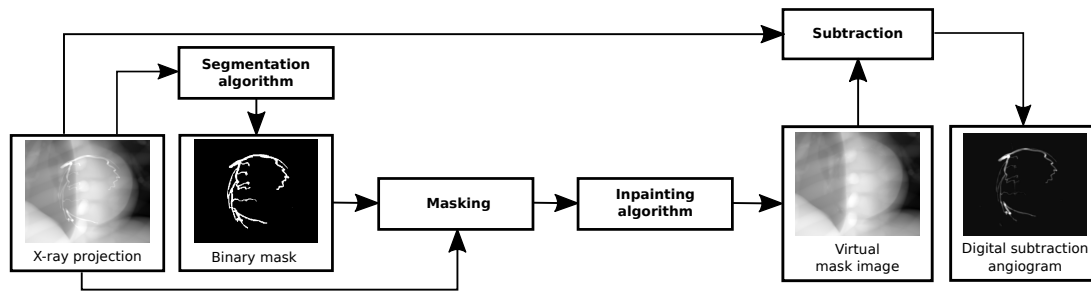


**Figure 3.1:** Truncation removal using virtual single frame material decomposition in the background subtraction sense. A binary segmentation of the object is used to identify positions subject to background estimation via an inpainting method. Finally, the estimated background is subtracted from the original projection yielding a **virtual digital subtraction angiography (vDSA)** image.

scene without contrast agent (mask scan) are digitally subtracted from projections acquired during contrast injection (fill scan), yielding images of the contrasted lumen only. Unfortunately, **DSA** can only be applied successfully to invariant anatomies, such as the cerebral vasculature [Gao 16, Yi 17]. Object motion between the acquisition of mask and fill scan introduces misalignment artifacts that deteriorate diagnostic value and require compensation [Bent 02]. For cardiac imaging, this requirement is particularly problematic as the coronary arteries are subject to constant cardiac and respiratory motion (cf. Sec. 2.4.2).

For imaging in a static acquisition geometry, misalignments introduced by inter-scan motion may be compensated for by image registration [Fitz 88, Neja 14]. Other methods seek to avoid the problems induced by the acquisition of two subsequent images as a whole. Such approaches estimate mask images from fill scans [Blon 06, Zhou 08, Hu 12, Bros 15], a technique that we will refer to as **virtual digital subtraction angiography (vDSA)**. All methods are similar in that they require vessel segmentation to identify regions for image inpainting, i.e., background estimation. Brosig et al. assume a static scanner geometry and temporal angiography sequences to estimate background images using guided inpainting [Bros 15].

However, this method is not applicable in rotational angiography, where the moving gantry introduces yet another source of inconsistency. In this context, methods operating on a single image are essential. An outline of such algorithms is presented in Fig. 3.1. While the methods employed for vessel segmentation differ, the variation in inpainting algorithms is rather limited. Brosig et al. use bilinear interpolation, whereas Blondel et al. and Zhou et al. use morphological closure to estimate the background image [Blon 06, Zhou 08]. These methods work well for small ROIs but usually perform poorly when large areas need to be estimated [Aach 01, Berg 14].

Recently, methods from machine learning based on **denoising auto-encoders (DAEs)** and **convolutional neural networks (CNNs)** have received increasing attention, and were applied successfully to image inpainting [Xie 12, Kohl 14, Cai 15]. These approaches are of substantial interest, as they potentially allow for background estimation without the need for segmentation, an approach that is commonly referred to as **blind inpainting**. State-of-the-art results on natural images are impressive [Kohl 14, Cai 15], however, the applicability to medical images, particularly to **vDSA**

has yet to be demonstrated.

It is worth mentioning that material decomposition, particularly the separation of contrast agent and background, is also possible with photon counting detectors [Roes 07, Maas 09, Lu 15]. These methods exploit the energy dependence on the attenuation coefficients introduced in Sec. 2.2.1.2, but require dedicated detectors [Tagu 13] that are not yet ready for commercial deployment [Mull 16].

### 3.2.2 Background Suppression

The methods specified in Sec. 3.2.1 approximate detector domain material decomposition. If accurate, these methods yield projection images that are still valid in the image formation sense (cf. Sec. 2.2.1) which should be preferred for tomographic reconstruction and CC. Unfortunately, this benefit most often comes at the cost of highly sophisticated algorithms that require thorough parameter tuning to perform well [Berg 14, Unbe 17a].

For the sake of completeness, we would like to mention that simple background suppression, albeit theoretically incorrect, proved highly beneficial for both one-shot [Rohk 10b, Schw 13a] and iterative tomographic reconstruction [Hans 08b, Liu 14]. Rather than estimating a complete background image, all aforementioned methods rely on simple, morphological image processing techniques. They apply top-hat filters [Soil 04] to the projection images that are, in essence, an erosion followed by a dilation with a particular structuring element. Consequently, such filters suppress all structures that are larger than the, usually circular, structuring element.

Simple preprocessing algorithms, such as top-hat filtering, are attractive as they are readily applicable to unseen data sets. Moreover, the benefit of sparse projection images seems to outweigh the error introduced by rough background reduction in tomographic reconstruction [Hans 08b, Rohk 10b, Cime 16a]. Whether these advantages also apply in the context of DCMs has yet to be discussed.

## 3.3 Cardiac Motion

Cardiac motion is usually addressed in terms of retrospective gating or binning using surrogate signals. An illustration is provided in Fig. 3.2. The idea is to select subsets of images that correspond to the same cardiac phase. It becomes obvious from Fig. 3.2 that the amount of available images is dependent on the number of observed cardiac cycles, i. e., the heart rate; high heart rates are preferable in order to obtain as many images as possible for reconstruction. However, for clinical single-sweep rotational angiograms (cf. Sec. 2.2.1 and Sec. 2.4.2.1), the reconstruction problem is known to remain ill-posed [Laur 06, Cime 16a].

Gating approaches are generic in the sense that they can be employed in both symbolic and tomographic reconstruction algorithms. Moreover, the choice of low-dimensional surrogate signal, that is used to determine the cardiac phase of a specific projection image, is unrestricted. Most methods rely on the simultaneously acquired ECG signal [Laur 06, Rohk 10b, Schw 13a, Cime 16b, Cime 16a] and define the cardiac phase of a particular image by its relative distance to the two neighboring R peaks (see Fig. 3.2).

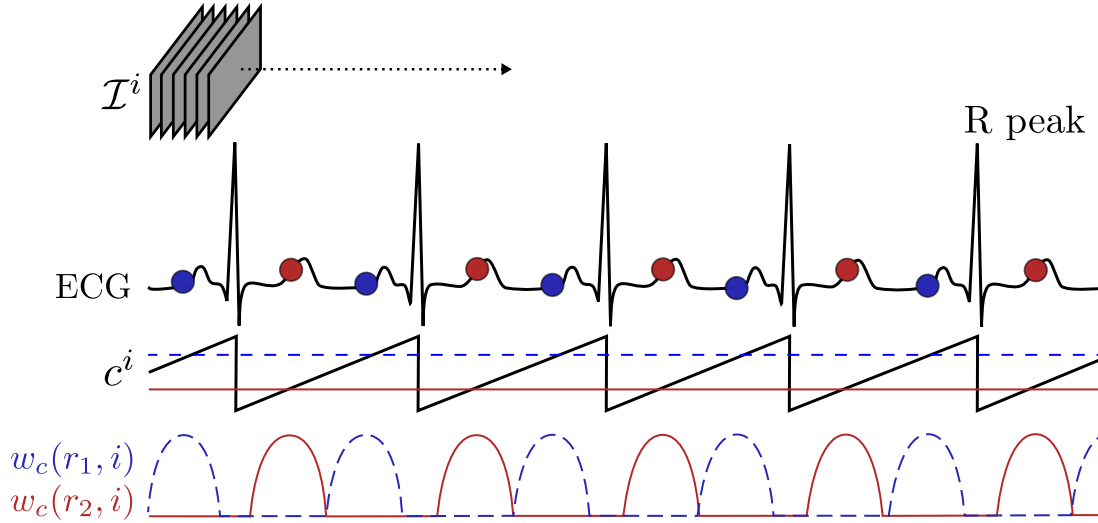


**Figure 3.2:** During acquisition of projection images  $\mathcal{I}^i$  an electrocardiogram (ECG) signal is recorded (top row), and converted to cardiac phases  $c^i \in [0, 1]$  using the relative distance to the two neighboring R peaks (middle row, sawtooth signal). We select two exemplary reference phases  $c^{r1}$  and  $c^{r2}$  at end diastole and end systole, respectively, to demonstrate restrictive nearest neighbor gating (middle row) and continuous phase weighting (bottom row).

Although usage of the ECG should be considered state-of-the-art, image-based surrogates are known in literature and may be preferable as they encode the motion state rather than the electro-physiologic activation [Blon 06, Lehm 06, Unbe 17a]. These approaches usually assume that the predominant displacement in axial direction results from the superior-inferior motion of the heart during contraction [Blon 06, Lehm 06]. Extrema in such displacement sequences are then used analogously to the R peaks in the ECG. To define the surrogate, Lehmann et al. and Blondel et al. make use of horizontal line integrals of subsequent X-ray images [Lehm 06, Blon 06]. These approaches are highly similar to the well known Amsterdam Shroud (AS) [Zijp 04] and fail in presence of non-cardiac axial motion, such as respiration, or for non-circular trajectories, such as dual axis rotational angiography (DARCA) [Klei 11, Grec 12] or saddle trajectories [Pack 04].

Once a cardiac phase is assigned to each projection image, quasi-stationary subsets can be determined using nearest neighbor or continuous gates, depending on the reconstruction algorithm. Nearest neighbor gating selects one image from each cardiac cycle that is closest to the reference  $c^r$  in terms of cardiac phase  $c^i$ , such that the weighting function  $w_c(r, i)$  is unity for each nearest neighbor and zero everywhere else. It is primarily deployed for symbolic reconstruction methods [Blon 06, Jand 09, Liao 10, Cime 16b], as it severely undersamples the available projection data which may lead to streaking artifacts [Sidk 06, Scha 06] in tomographic reconstruction. Another option is to use cosine-based weighting functions that retain more data but increase the residual motion within each gate [Scha 06, Rohk 10b, Schw 13b, Schw 13a].



Following Rohkohl et al. [Rohk08], the gating weight  $w_c(r, i)$  of image  $\mathcal{I}^i$  at cardiac phase  $c^i$  with respect to a reference phase  $c^r$  is given by

$$w_c(r, i) = \begin{cases} \cos^{a_g} \left( \frac{|c^r - c^i|}{w_g} \pi \right) & \text{if } |c^r - c^i| < \frac{w_g}{2} \\ 0 & \text{else} \end{cases}, \quad (3.1)$$

where  $a_g$  and  $w_g$  are constants controlling shape and width of the bell-shaped function, that can be tuned automatically [Rohk10a].

It is known in literature, that the reconstruction quality depends on the target heart phase [Scha06] due to different amount of residual motion within gates. Typically, a reference heart phase at end diastole is selected heuristically [Shec06, Husm07], yet algorithms exist that determine the optimal reference phase for each data set individually [Rasc06a, Hans08a].

## 3.4 Respiratory Motion

Due to the low frequency of respiratory motion (cf. Sec. 2.4.2.2) only very few recurrences are observed during a standard acquisition. Respiratory gating strategies based on surrogate signals [Fisc15, Sand16] similar to Sec. 3.3 followed by cyclic registration proved robust in image-guided radiation therapy [Sonk05, Li07, Geim17b]. Unfortunately, in the context of rotational angiography respiratory phase gating is impossible as it would result in a highly ill-posed problem, impeding the application of aforementioned methods.

A prominent solution is to avoid the problem as a whole by requiring patients to hold their breath throughout the acquisition. If breath-hold is impossible or imperfect, motion estimation techniques must be applied to mitigate the corruption due to respiration and, finally, enable 3D reconstruction.

Virtually all state-of-the-art methods for respiratory motion compensation in standard protocols require an initial 3-D reconstruction of the structure of interest, that enables 3-D/2-D registration of the model to subsequent motion states. In bi-plane angiography it has been shown that this strategy allows for the estimation of 3-D rotations and translations [Bros10] but even dense 3D displacement fields can be recovered [Shec03, Shec06]. Reconstruction of a prior 3-D model in presence of respiratory motion may also be possible from multiple views of single-plane rotational angiography. Blondel et al. use alternating symbolic reconstruction and bundle adjustment steps to estimate detector shifts to account for respiratory motion [Blon04, Blon06]. In the context of rotational angiography, however, motion estimation is far more challenging as supposedly consistent frames are acquired successively rather than simultaneously. Hence, there is no guarantee that a particular motion state is observed more than once. In the most general case, the reconstruction of such initial model is challenging or even impossible, making its requirement a limiting factor for the applicability of the methods.

As of yet, the only method fully acknowledging this problem was proposed by Rohkohl et al. [Rohk09]. Respiratory motion is expressed in terms of 3-D affine transforms between subsequent frames. The motion parameters are determined by optimization of a cost function, that evaluates the correlation between the acquired projections

and maximum intensity projections (MIPs) of compensated reconstructions. As the optimization relies on stochastic gradient descent [Rohk09, Rohk10b], the method still requires a sufficiently meaningful initial reconstruction.

## 3.5 Vasculature Reconstruction Algorithms

We limit our summary to the methods most relevant to the topics discussed here and provide in depth information on four particularly important algorithms: symbolic reconstruction using 3-D cost maps [Li11], explicit and implicit correspondence matching [Blon06, Liao10], and streak-reduced, ECG gated tomographic reconstruction [Schw13b]. This course of action seems justified, considering the excellent and very recent review on the topic by Çimen et al. [Cime16a].

### 3.5.1 Tomographic Reconstruction

Tomographic reconstruction algorithms produce a volume representing the coronary artery lumen. In general, these methods neither require nor impose prior information on the coronary artery tree [Cime16a] (particularly the shape of the lumen), making them highly suitable for the reconstruction of anomalies [Scho09]. Compared to symbolic algorithms, tomographic methods usually require more consistent projection images over a large angular range in order to reduce the violations of Tuy's data completeness condition [Tuy83, Zeng10].

Straight-forward tomographic reconstruction in the FBP-sense as described in detail in Sec. 2.3.1 is possible by modification of Eq. (2.14). Using  $\underline{u}^i = \mathbf{P}^i \underline{x}$ , the 3-D tomographic reconstruction at cardiac phase  $c^r$  is given by

$$f^r(\mathbf{x}) = \sum_{i=1}^{N_\lambda - 2N_{\text{ign}}} \frac{1}{(\underline{u}_3^i)^2} w_c(r, i) \cdot \widetilde{\mathcal{I}}^i(h(\underline{u}^i)) , \quad (3.2)$$

where  $w_c(r, i)$  denotes the gating weight of image  $\mathcal{I}^i$  at cardiac phase  $c^i$  w. r. t. to the target heart phase  $c^r$ . To mitigate streaking artifact introduced by residual motion and severe undersampling, the  $N_{\text{ign}}$  smallest and largest contributions to each point  $\mathbf{x}$  are omitted [Rohk08, Schw13b]. Analytic one-shot reconstruction methods similar to Eq. (3.2) as employed in [Scha06, Rasc06b, Mova07, Rohk08, Rohk10b, Schw13a] are attractive as they exhibit low run times, however, the reconstruction quality may not be sufficient for diagnostic purposes [Cime16a].

Analytic methods are highly susceptible to angular undersampling yielding severe image artifacts that drastically impair the image quality and clinical value. In iterative reconstruction schemes these artifacts can be suppressed effectively by incorporating prior knowledge on image appearance (cf. Sec. 2.3.2), such as sparsity in intensity [Li02, Li04, Hans08b] or gradient domain [Zhou08, Wu11, Hu12].

Despite yielding superior image quality, these methods still operate on a subset of the acquired data only suggesting that further improvements may be possible if all projection images were used. To this end, some algorithms estimate the intra-scan displacements due to cardiac motion, that are then integrated into the geometric

description: a particular world point is displaced according to the estimated deformation before it is projected into detector domain such that

$$\begin{aligned}\mathbf{x}' &= \mathbf{x} + T_r^i(\mathbf{x}) \\ \underline{\mathbf{u}}^i &= \mathbf{P}^i \mathbf{x}',\end{aligned}\tag{3.3}$$

where  $T_r^i : \mathbb{R}^3 \rightarrow \mathbb{R}^3$  describes the 3-D translation of a world point at cardiac phase  $c^r$  to the corresponding location at phase  $c^i$  (cf. Fig. 2.4) [Blon 04, Scha 06, Rohk 10b, Liu 16]. This concept allows for straight-forward integration of highly complex motion patterns into standard reconstruction algorithms [Scha 06]. It is worth mentioning that a formulation according to Eq. (3.3) is approximate for analytic, FBP-based methods as no update of ramp, cosine, or redundancy filtering is performed [Prum 06, Scha 06]. To minimize the effects on image quality, the displacements are required to be small [Tagu 08].

### 3.5.2 Symbolic Reconstruction

In contrast to tomographic reconstruction algorithms, symbolic methods (also referred to as model-based [Cime 16a] or geometric [Rohk 11]) are more flexible with respect to the imaging geometry and, in general, require fewer consistent images [Cime 16a]. This flexibility is usually enabled by sparse input data, such as vessel centerlines [Blon 06, Liao 10, Li 11, Card 12, Liu 15, Cime 16b] or tubularity response maps [Jand 09, Keil 09a, Keil 09b], that are not obtained easily due to noise, poor contrast, or overlap with strongly attenuating structures. In general, the methods devised for symbolic reconstruction reveal a trade-off between the amount of views available and the need for accurate segmentation and manual interaction. The reason for this is, that most symbolic methods rely on implicit or explicit correspondence estimation between detector domain points. Establishing correspondences, however, is non-trivial as the matching is ambiguous due to the complex shape of the coronary artery tree.

#### 3.5.2.1 Symbolic Reconstruction via Explicit Correspondence Matching

This problem becomes particularly obvious for methods based on the epipolar geometry. Given a detector domain point  $\mathbf{u}$  in reference image  $\mathcal{I}^{r_1}$ , the epipolar constraint states that the corresponding point in view  $\mathcal{I}^{r_2}$  *must* lie on the respective epipolar line  $\underline{\mathcal{I}}_{r_2}^{r_1}$ . Unfortunately, the intersection of this line with the segmented coronary artery centerlines does not generally yield a single but multiple correspondence candidates as illustrated in Fig. 3.3a. Consequently, methods devised for reconstruction from bi-plane angiography rely on manual input to alleviate the ambiguity of the correspondence problem [Hoff 00, Andr 08]. Rotational angiography, however, yields multiple consistent views and hence enables fully automatic symbolic reconstruction algorithms. Blondel et al. propose to dissolve the ambiguity of the matching according to the epipolar constraint by incorporation of the remaining views [Blon 06]. Candidate 3-D points are triangulated from the proposed correspondences and then evaluated by reprojection into the remaining views. Correct correspondences of a linked set of points are assumed to a) project close to detector domain centerlines

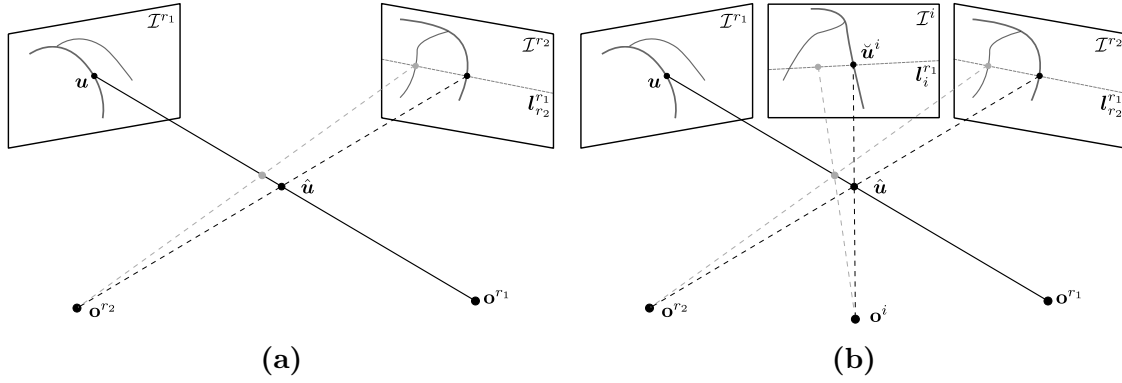


**Figure 3.3:** The epipolar constraint between views  $\mathcal{I}^{r1}$  and  $\mathcal{I}^{r2}$  yields two potential correspondence candidates for centerline point  $\mathbf{u}$ , making the correspondence matching ambiguous (Fig. 3.3a). The ambiguity of the matching can be resolved using views not currently used for triangulation (Fig. 3.3b).

in all views while b) remaining in close proximity and preserving the linked structure. The two requirements, referred to as relevance and geometric coherence, are combined in a joint energy function and optimized for using Dijkstra’s algorithm and dynamic programming [Blon 06, Dijk 59].

### 3.5.2.2 Symbolic Reconstruction via Implicit Correspondence Optimization

Rather than using triangulation from corresponding points, Liao et al. and Liu et al. proposed to directly estimate the depths of centerline pixels in a reference view  $\mathcal{I}^r$  [Liao 10, Liu 15]. To this end, the space between source and detector is discretized into  $L$  planes of equal depth with a spacing of  $\Delta L$ . Reconstructed 3-D centerline points  $\mathbf{u}$  must lie on the ray  $\mathbf{r}_u = \mathbf{o} \mathbf{u}^{3D}$  that connects the optical center  $\mathbf{o}$  and the 3-D position  $\mathbf{u}^{3D}$  of the 2-D centerline point  $\mathbf{u}$ . This geometrical relation is visualized in Fig. 3.4. Then, 3-D reconstruction essentially becomes a labeling problem, where every centerline point  $\mathbf{u}$  is assigned a label  $l_u$  corresponding to a certain depth plane. The method seeks to recover depth labels such that the reconstructed points are in good agreement with the remaining views and piecewise continuous [Liao 10]. Both requirements are integrated into an energy function that is minimized using discrete optimization, namely  $\alpha$ -expansion moves [Boyk 01] and belief propagation [Melt 05] in [Liao 10] and [Liu 15], respectively.

### 3.5.2.3 Symbolic Reconstruction via 3-D Minimal Paths

An approach partially similar to the implicit methods described above was proposed by Jandt et al. and Li et al.. They consider centerline reconstruction as a 3-D minimal path extraction problem [Jand 09, Li 11]. The 3-D cost map  $g^r$  at heart phase  $c^r$  is computed similar to Eq. (3.2) using modified backprojection operators that, in contrast to additive updates, promote sparsity in reconstruction domain. It is given by

$$g^r(\mathbf{x}) = \max_i \left( w_c(r, i) \cdot \Lambda^i \left( h \left( \underline{\mathbf{u}}^i \right) \right) \right), \quad (3.4)$$

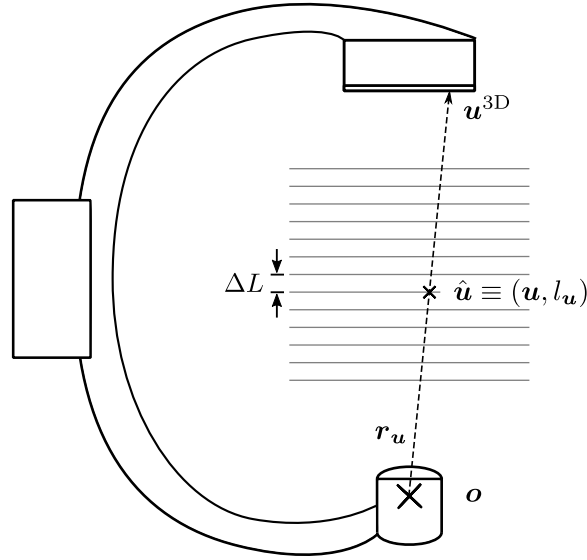


**Figure 3.4:** Depth labels with respect to a particular reference view. For a known imaging geometry, the position of the 3-D point  $\hat{\mathbf{u}}$  is uniquely determined by its observation on the detector  $\mathbf{u}$  and its depth label  $l_{\mathbf{u}}$ .

where  $\underline{\mathbf{u}}^i = \mathbf{P}^i \underline{\mathbf{x}}$ ,  $w_c : \mathbb{N} \times \mathbb{N} \mapsto \{0, 1\}$  denotes nearest neighbor gating, and  $\Lambda^i$  is the distance transform of the vessel centerlines in view  $i$ , that will be derived thoroughly in Sec. 4.4.1. 3-D centerlines are then extracted from  $g^r$  using minimal paths [Li11] or fast marching [Jand09].



# Rotational Angiography Data and Preprocessing

4.1	Introduction .....	33
4.2	Phantom Data .....	33
4.3	Clinical Data .....	34
4.4	Preprocessing .....	35
4.5	Experiments .....	38
4.6	Results and Discussion .....	40
4.7	Conclusion .....	40

## 4.1 Introduction

To evaluate the methods developed within the scope of this thesis, we rely on simulation studies based on *in silico* phantoms and on clinically acquired *in vivo* data, that is presented in detail in Sec. 4.2 and Sec. 4.3, respectively. The projection images are preprocessed automatically to a) extract the vessel centerlines, b) segment the contrasted lumen, and c) estimate a non-contrast background for vDSA imaging. The methods devised for these tasks are described in Sec. 4.4. Finally, we apply the algorithms to our data as described in Sec. 4.5 and report our findings in Sec. 4.6 and Sec. 4.7.

## 4.2 Phantom Data

To assess the proposed methods in a controlled environment we extend the cardiac vasculature reconstruction evaluation (CAVAREV<sup>1</sup>) framework [Rohk 10c] to allow for the evaluation of both tomographic and symbolic coronary artery reconstruction algorithms. Within the CAVAREV framework, the dynamic XCAT phantom [Sega 01, Sega 08, Rohk 10c] was used to simulate the 3-D anatomy in various motion states. Anatomy and physiology of the 4-D XCAT are based on 4-D tagged magnetic resonance imaging (MRI) and high-resolution respiratory-gated 4-D computed tomography (CT) data sets of human subjects [Sega 08], allowing for highly realistic modeling of the vasculature and its embedding even in presence of motion.

---

<sup>1</sup><https://www5.cs.fau.de/research/software/cavarev/>

The *XCAT* phantom consists of B-spline surface definitions for the organs in the thorax, which in the original CAVAREV were used to generate temporal series of 3-D ground truth volumes. The 4-D sequences were then forward projected assuming a 5 s circular short scan trajectory covering  $200^\circ$  yielding  $N_\lambda = 133$  2-D rotational angiography images. We summarize the most important geometrical parameters in Tab. 4.1. The CAVAREV framework comprises data sets exhibiting two distinct motion patterns:

1. strictly periodic cardiac motion referred to as *CARD*, and
2. strictly periodic cardiac motion superimposed by respiratory motion denoted by *CARDBREATH*.

Providing projection images only is sufficient for objective comparison between tomographic reconstruction algorithms but does not yet accommodate symbolic methods. To overcome this limitation, we utilize the 3-D ground truth volumes to extract 3-D ground truth coronary artery centerlines and binary masks of the lumen. We then forward project both the centerlines and the binary masks at every motion state to obtain detector domain centerlines and segmentation masks, that serve as input to symbolic reconstruction algorithms.

The 3-D centerlines as well as the 3-D binary masks of the lumen can then be used to objectively assess reconstruction performance. Centerline and volumetric ground truth at the motion state corresponding to projection  $\mathcal{I}^i$  are denoted by  $\mathcal{G}_c^i$  and  $g_c^i$  for *CARD*, and  $\mathcal{G}_b^i$  and  $g_b^i$  for *CARDBREATH*, respectively.

## 4.3 Clinical Data

Clinical data sets were provided by Dr. med. Michaela Hell and Prof. Dr. med. Stephan Achenbach, Department of Cardiology, Friedrich-Alexander-Universität Erlangen-Nürnberg. They were acquired on two distinct *Artis one* systems (Siemens Healthcare GmbH, Forchheim, Germany). All data sets consist of  $N_\lambda = 133$  projection images acquired on a circular short scan trajectory covering  $200^\circ$  over 5 s. We state the acquisition parameters in Tab. 4.1. A catheter is inserted into the femoral artery and navigated to the *LCA* ostium (cf. Sec. 2.1.2). During X-ray acquisition, the coronary arteries are contrasted using an iodine-based contrast agent, namely *Ultravist®-370* [Baye 14], that is injected at  $4 \text{ mL s}^{-1}$ .

In contrast to *in silico* phantom data, 3-D ground truth is generally inaccessible for clinical cases. To enable quantitative evaluation of some of the proposed algorithms, a medical imaging expert with more than three years experience in interventional cardiac imaging manually extracted the coronary artery centerlines in projection domain.



**Table 4.1:** Acquisition parameters for the phantom and clinical data sets.  $D_{SI}$  and  $D_{SD}$  denote the [source-isocenter-distance \(SID\)](#) and [source-detector-distance \(SDD\)](#) while  $U_1, U_2$  and  $\Delta u_1, \Delta u_2$  refer to the number of pixels and the corresponding pixel size in detector  $u_1$  and  $u_2$  direction, respectively. Moreover, we state the peak tube voltage  $U_{Tube}$  and the tube current  $I_{Tube}$  for the clinical acquisitions.

	$D_{SD}$	$D_{SI}$	$U_1 \times U_2$	$\Delta u_1, \Delta u_2$	$U_{Tube}$	$I_{Tube}$
CAVAREV	1200 mm	800 mm	$960 \times 960$ px	0.32 mm	- kV	- mA
R1	1200 mm	720 mm	$896 \times 812$ px	0.308 mm	90.0 kV	602 mA
R2	1200 mm	720 mm	$776 \times 712$ px	0.386 mm	90.0 kV	508 mA
R3	1200 mm	720 mm	$896 \times 812$ px	0.308 mm	91.6 kV	717 mA

## 4.4 Preprocessing

### 4.4.1 Vessel Segmentation and Centerline Extraction

Many methods in angiography, including the algorithms presented in this thesis, rely on binary segmentation masks or vessel centerlines. As this work focuses on respiratory motion estimation and 3-D reconstruction, we follow the literature [[Blon 06](#), [Jand 09](#), [Liao 10](#), [Poly 12](#), [Buda 13](#), [Cime 16b](#)] and rely on the combination of well established segmentation algorithms such as vesselness [[Fran 98](#)] and medialness filters [[Koll 95](#)] to automatically process the clinical data sets.

In angiography, contrasted vessels appear as narrow tubular structures that are bright with respect to the surrounding background. It seems natural to exploit this prior knowledge for segmentation in a multi-scale approach based on first and second order derivatives. The acquired images are preprocessed using the well-known bilateral filter that suppresses noise while preserving edges [[Toma 98](#), [Maie 16](#)].

Let  $\alpha(\mathbf{u}, \sigma)$  be the local orientation of a structure at position  $\mathbf{u}$  and scale  $\sigma$ , and let  $\mathbf{e}_\alpha$  be a unit vector orthogonal to the respective orientation. If the structure at  $\mathbf{u}$  is a contrasted vessel of scale  $\sigma$  we expect high negative gradients in the direction orthogonal to  $\alpha$  as well as a high negative curvature along  $\mathbf{e}_\alpha$ . Filters that enhance structures with aforementioned properties are already known in literature [[Dehk 11](#)]. We briefly restate vesselness and Koller filtering following [[Fran 98](#)] and [[Koll 95](#)], respectively. Finally, we describe a strategy to merge both responses to obtain a) binary segmentation masks and b) vessel centerlines.

#### 4.4.1.1 Vesselness Filtering

In order to determine the respective responses at position  $\mathbf{u}$ , first the Hessian matrix is computed as

$$\mathbf{H}(\mathbf{u}, \sigma) = \begin{pmatrix} \frac{\partial^2 \mathcal{I}_\sigma(\mathbf{u})}{\partial u_1^2} & \frac{\partial^2 \mathcal{I}_\sigma(\mathbf{u})}{\partial u_1 \partial u_2} \\ \frac{\partial^2 \mathcal{I}_\sigma(\mathbf{u})}{\partial u_1 \partial u_2} & \frac{\partial^2 \mathcal{I}_\sigma(\mathbf{u})}{\partial u_2^2} \end{pmatrix}, \quad (4.1)$$

where  $\mathcal{I}_\sigma = \mathcal{I} * G_\sigma$ ,  $G_\sigma$  is a 2-D Gaussian kernel with standard deviation  $\sigma$ ,  $\mathcal{I}$  is the projection image, and  $*$  denotes convolution. The Eigenvalues of the Hessian matrix

$\nu_{1/2}$ ,  $|\nu_1| \geq |\nu_2|$  are related to the tubularity of an underlying structure and allow for the definition of meaningful quantities. The Blobness  $B = \nu_2/\nu_1$  is close to zero for tubular structures and close to unity for bright regions with similar extent in all directions, such as blobs. The structureness  $S = \sqrt{\nu_1^2 + \nu_2^2}$  is given by the Frobenius norm of the Hessian and is close to zero for uniform background and large in regions with high contrast [Fran 98]. Combining the two measures into a probability-like response yields the vesselness

$$\mathcal{V}(\mathbf{u}) = \max_{\sigma} e^{(-c_B B)} \cdot (1 - e^{(-c_S S)}) , \quad (4.2)$$

where  $c_B$  and  $c_S$  are constants that control the influence of  $B$  and  $S$ . Tuning  $c_B$  and  $c_S$  for sensitivity yields strong responses for vessels, but also for other structures with high curvature, such as the edges of bones. Subsequent hysteresis thresholding [Cann 86] and removal of small connected components [Chan 04] suppresses isolated responses and yields a binary mask  $\mathcal{V}_b$ .

#### 4.4.1.2 Koller Filtering

In contrast to the vesselness filter that enhances the complete lumen, Koller filtering only yields strong responses on the centerline of tubular structures. Given the Hessian  $\mathbf{H}(\mathbf{u}, \sigma)$ , we can compute the orientation  $\alpha(\mathbf{u}, \sigma)$  of the generating structure as  $\tan(2\alpha) = 2H_{12}/(H_{11} - H_{22})$ , where  $hessEl_{ij}$  is the element of the Hessian  $\mathbf{H}$  in row  $i$  and column  $j$ , respectively. For vessels with scale  $\sigma$  we expect large negative gradients at its boundaries  $\mathbf{u} \pm \sigma \mathbf{e}_\alpha$ , yielding the Koller filter response

$$\mathcal{K}(\mathbf{u}) = \max_{\sigma} \left\{ \min \left\{ -\left(\nabla \mathcal{I}_{\sigma}(\mathbf{u} + \sigma \mathbf{e}_\alpha)\right)^\top \mathbf{e}_\alpha, \left(\nabla \mathcal{I}_{\sigma}(\mathbf{u} - \sigma \mathbf{e}_\alpha)\right)^\top \mathbf{e}_\alpha \right\} \right\} .$$

#### 4.4.1.3 Filter Combination

Both the vesselness and Koller filtered image contain excess responses from structured background, such as lung tissue or the vertebrae. Erroneous segmentations are, at least partly, mutually exclusive making a combination of both responses beneficial. The refined Koller response  $\mathcal{K}_r$  is obtained by a per-pixel weighting with the vesselness, reading  $\mathcal{K}_r(\mathbf{u}) = \mathcal{K}(\mathbf{u}) \cdot \mathcal{V}(\mathbf{u})$ . Similar to Blondel et al. [Blon 06], we then extract initial centerline candidates from  $\mathcal{K}_r$  using thresholding. The set of potential centerline points is given by  $Q = \{\mathbf{u} \mid \mathcal{K}_r(\mathbf{u}) > c_K\}$ , where  $c_K$  is a heuristically determined threshold.

$Q$  still contains isolated responses and discontinuous centerlines, but can be used to derive a cost map for centerline extraction in the minimal path sense. To this end, the distance transform of  $Q$  is used to define the edge costs for path extraction. The distance transform is defined as  $\Lambda(\mathbf{u}|Q) = \|\mathbf{u} - d(\mathbf{u}|Q)\|_2$ , where  $d(\mathbf{u}|Q) = \operatorname{argmin}_{\mathbf{v} \in Q} \|\mathbf{v} - \mathbf{u}\|_2$  is the closest point to  $\mathbf{u}$  in  $Q$ . Subsequently, the final set of centerlines is extracted from  $\Lambda(\mathbf{u}|Q)$  as minimal cost paths between end nodes and the start node using Dijkstra's algorithm [Dijk 59] with back tracking. The start node is defined as the first point of the largest connected component in  $Q$ . As the true end nodes are not known, every centerline candidate point in  $Q$  is considered as a potential end node. Finally, after path extraction and pruning of short branches

the extracted centerline tree  $\mathcal{T}$  is given by the junction of all remaining branches  $\mathcal{T} = \bigcup \mathcal{B}_i$ . We also compute its distance transform  $\Lambda(\mathbf{u}|\mathcal{T})$  for later use in reconstruction algorithms.

Subsequently, the aforementioned cost map  $\Lambda(\mathbf{u}|\mathcal{Q})$  is used to refine the binary lumen segmentation. We assume, that the final segmentation mask  $\mathcal{W}$  can only be non-zero within a certain distance  $c_R$  to vessel centerlines candidates, such that

$$\mathcal{W}(\mathbf{u}) = \begin{cases} 1 & \text{for } \mathcal{V}_b(\mathbf{u}) \neq 0 \wedge \Lambda(\mathbf{u}|\mathcal{Q}) < c_R \\ 0 & \text{otherwise} \end{cases}, \quad (4.3)$$

where  $c_R$  is chosen to reflect the largest vessel diameter to be expected. Finally, we define the inverse segmentation mask  $\overline{\mathcal{W}}$ , where  $\overline{\mathcal{W}}(\mathbf{u}) = 1 - \mathcal{W}(\mathbf{u})$ .

#### 4.4.2 Background Estimation

We design a **vDSA** pipeline following the schematic shown in Fig. 3.1. Once binary segmentation masks are obtained according to Sec. 4.4.1, they are used to remove intensity information at the locations of contrasted vessels, thereby artificially corrupting the projections. Formally, the corrupted image  $\mathcal{G}$  is obtained by multiplying the original image with the inverse mask such that  $\mathcal{G} = \mathcal{I} \cdot \overline{\mathcal{W}}$ . The acquired image  $\mathcal{I}$  and the background image that we seek to estimate  $\mathcal{B}$  are similar in that their corrupted versions cannot be distinguished:

$$\mathcal{G} = \mathcal{I} \cdot \overline{\mathcal{W}} \stackrel{!}{=} \mathcal{B} \cdot \overline{\mathcal{W}}. \quad (4.4)$$

The artificially corrupted observation  $\mathcal{G}$  does not contain any information about the presence of contrast agent. Consequently, the estimation solely relies on the remaining structures and the resulting background estimate can be considered a virtual non-contrast image (cf. Sec. 3.2). The corrupted regions of  $\mathcal{G}$  are narrow and sparse but they are connected. Simple methods, such as morphological closure, are predominant in literature, however, in the case of background recovery they often yield patchy images with unnatural appearance, a behavior that is largely suppressed when non-local techniques in frequency domain are used [Berg 14].

A concurrent approach proposed by Aach et al. tries to recover the missing values using spectral domain techniques [Aach 01]. According to the convolution theorem, Eq. (4.4) can be restated as a convolution in frequency domain  $\mathbf{g} = \frac{1}{N_u}(\mathbf{b} * \overline{\mathbf{w}})$ , where  $N_u$  is the number of pixels in the background image, and  $*$  denotes convolution. Both  $\mathcal{G}$  and  $\mathcal{B}$  are real valued such that their Fourier transforms  $\mathbf{g}$  and  $\mathbf{b}$ , respectively, are symmetric. Therefore, it holds  $\mathbf{b}(k) = \mathbf{b}^*(N_u - k)$  for a spectral line pair  $\mathbf{b}(k)$  and  $\mathbf{b}(N_u - k)$ . Let the spectrum  $\mathbf{b}$  of the undistorted background  $\mathcal{B}$  consist of only a single spectral line pair  $\mathbf{b}(k) = \hat{\mathbf{b}}(s)\delta(k - s) + \hat{\mathbf{b}}(N_u - s)\delta(k - (N_u - s))$ . Then, using

$$\mathbf{g}(s) = \frac{1}{N_u}(\mathbf{b} * \overline{\mathbf{w}})(s) = \frac{1}{N_u} \sum_l^{N_u} \mathbf{b}(l) \cdot \overline{\mathbf{w}}(l - s), \quad (4.5)$$

the observed line pair at  $s$  and  $N_u - s$  reads:

$$\begin{aligned} \mathbf{g}(s) &= \frac{1}{N_u} \left( \hat{\mathbf{b}}(s) \cdot \overline{\mathbf{w}}(0) + \hat{\mathbf{b}}^*(s) \cdot \overline{\mathbf{w}}(2s) \right) \\ \mathbf{g}(N - s) &= \mathbf{g}^*(s) = \frac{1}{N_u} \left( \hat{\mathbf{b}}^*(s) \cdot \overline{\mathbf{w}}^*(0) + \hat{\mathbf{b}}(s) \cdot \overline{\mathbf{w}}^*(2s) \right) \end{aligned} \quad (4.6)$$

**Table 4.2:** Heuristically determined parameters used in the segmentation algorithms. Constant  $c_B$  is defined using the  $c$ -th percentile of the structureness  $\mathbb{P}_c(c_S)$ . As the Koller filter response is not normalized,  $c_K$  is dependent on image domain gradients and, hence, the contrast level.

$c_B$	$c_S$	$c_R$	$c_K$
$1/0.5^2$	$1/(\mathbb{P}_{0.98}(S))^2$	4.0 mm	0.07

where  $\hat{\mathbf{b}}(s)$  and  $\hat{\mathbf{b}}(N - s) = \hat{\mathbf{b}}^*(s)$  are the coefficients to be recovered. Eq. (4.6) can be solved for  $\hat{\mathbf{b}}(s)$  yielding

$$\hat{\mathbf{b}}(s) = N_u \cdot \frac{\mathbf{g}(s)\overline{\mathbf{w}}(0) - \mathbf{g}^*(s)\overline{\mathbf{w}}(2s)}{|\overline{\mathbf{w}}(0)|^2 - |\overline{\mathbf{w}}(2s)|^2}. \quad (4.7)$$

In practice, however,  $\mathbf{b}$  consists of more than a single spectral line pair. After one such deconvolution step the error is zero only at  $s$  and  $N_u - s$ . Therefore, deconvolution is applied iteratively, estimating multiple line pairs  $s_i$  and  $N_u - s_i$  in succession. The line pairs for each iteration are selected such that they maximize the decrease in mean-square error [Aach 01].

We apply spectral deconvolution in a patch wise manner to preserve the locality of image appearance. The patches exhibit partial overlap and are weighted with a Blackman window to create artificially continuous signals and to avoid spectral leakage [Harr 78].

Finally, the estimated background image is subtracted from the acquired images yielding a **virtual digital subtraction angiography** (vDSA)  $\mathcal{D}(\mathbf{u}) = \mathcal{I}(\mathbf{u}) - \mathcal{B}(\mathbf{u})$ . Assuming perfect segmentation and background estimation,  $\mathcal{D}$  contains contributions of the contrast agent only. As the contrast agent is confined to the coronary arteries that do not extend beyond the FOV, the resulting vDSA images  $\mathcal{D}^i, i = 1, \dots, N_\lambda$  are, ideally, not truncated. This enables the application of consistency-based methods for intra-scan motion detection that are described in the following chapter.

## 4.5 Experiments

We apply the automatic methods devised in Sec. 4.4.1 to the clinical acquisitions to obtain projection domain centerline and binary segmentation masks that are readily available for the phantom data. The performance of aforementioned algorithms depends on the choice of parameters that were tuned heuristically. Tab. 4.2 summarizes the values used for all experiments on clinical data.

Subsequently, we estimate non-contrast background images  $\mathcal{B}$  using the method described in Sec. 4.4.2 to obtain vDSA sequences of all data sets.

We evaluate the performance of the described methods qualitatively, as no adequate ground truth is available.

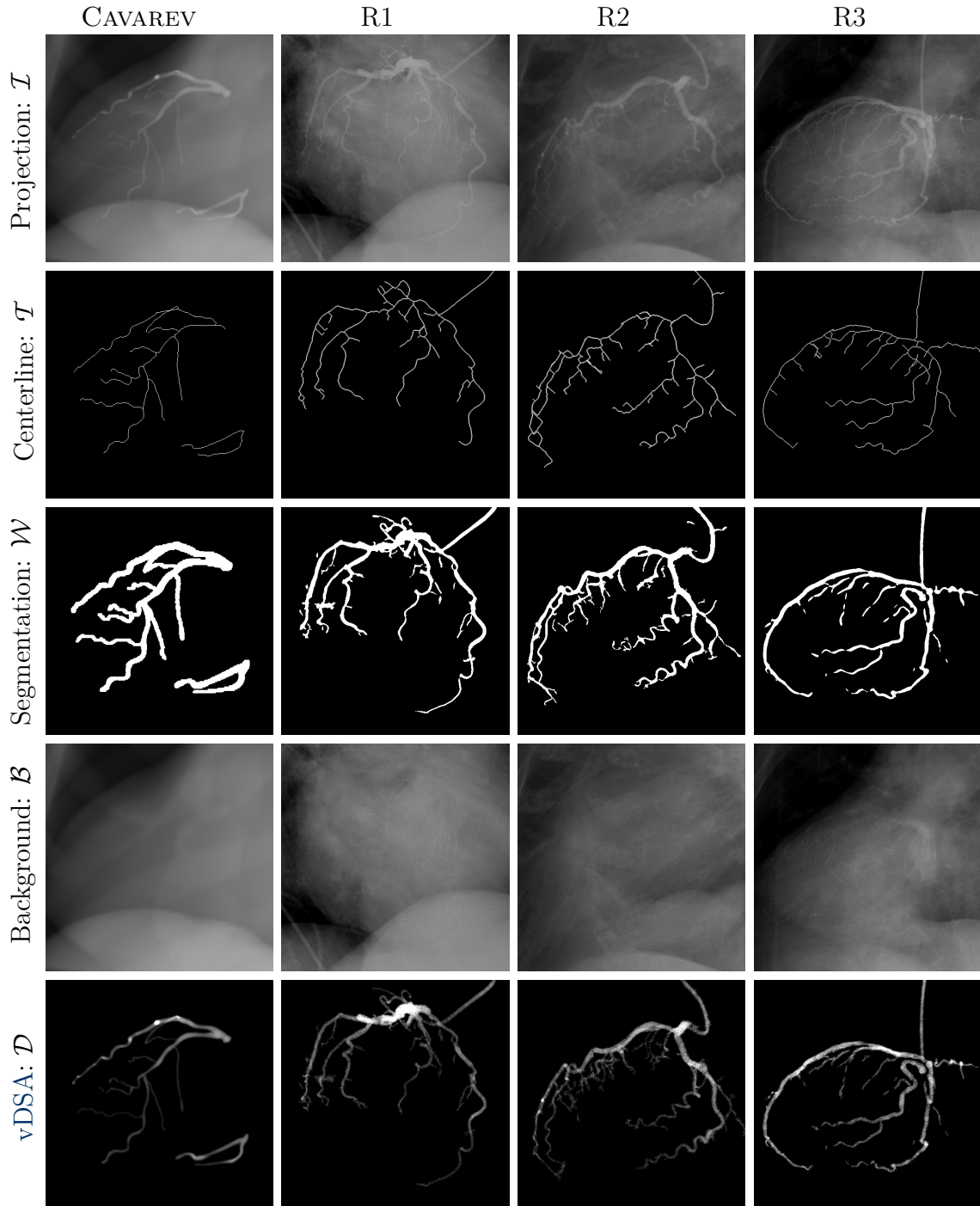


**Figure 4.1:** From top to bottom: projection, centerline, binary segmentation, estimated background, and virtual subtraction image. Red and green arrows point to excess and missing segmentations, respectively. We show representative angiograms of the coronary arteries at different viewing angles for the phantom data set CAVAREV, and the three clinical acquisitions R1, R2, and R3. Individual data sets occupy one column each.

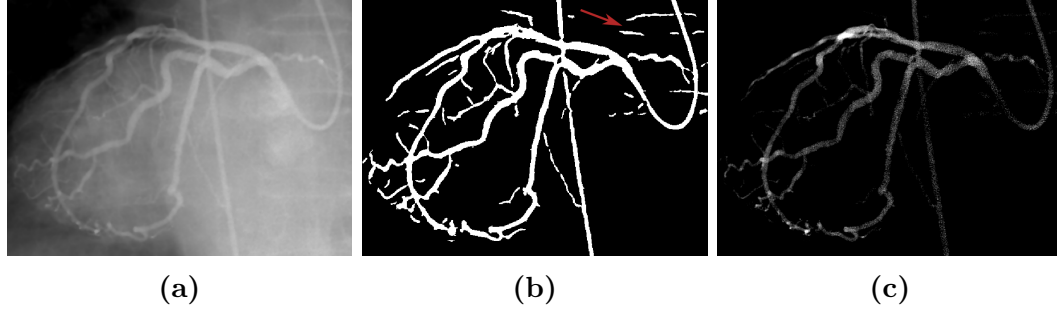


**Figure 4.2:** Fig. 4.2b represents the binary segmentation mask obtained from segmenting Fig. 4.2a using the algorithm described above. While erroneous segmentations (highlighted by the red arrow) are very prominent in the binary mask, they are not as distinct in the vDSA image.

## 4.6 Results and Discussion

Representative results of the proposed methods for centerline extraction, lumen segmentation, and background estimation are shown in Fig. 4.1. Obtaining good centerline and segmentation quality was particularly difficult in views that exhibit overlap of the arterial tree with the spine which drastically decreases vessel visibility. Moreover, we observed discontinuous segmentations that arise from low vessel contrast. Background estimation worked well for both phantom and clinical data sets, yielding vDSA images that, at least visually, exhibit a very low level of artifact. Yet, segmentation errors propagate through the whole vDSA pipeline and erroneously segmented structures, such as vertebrae, are pronounced in the binary mask as can be seen in Fig. 4.2b. However, the presence of mis-segmentation is not as distinct in the vDSA image (cf. Fig. 4.2c), potentially decreasing its influence on subsequently applied algorithms such as motion estimation or reconstruction. Moreover, a preliminary study suggested that the de-truncated vDSA images and CC can be used to reduce over-segmentation within sequences that are consistent otherwise [Unbe 16b].

CAVAREV does not provide non-contrast projection images, such that quantitative evaluation is impossible. We would like to point out that the results reported here, albeit qualitative, are in excellent agreement with studies published earlier that included a quantitative assessment [Unbe 16b, Unbe 16c, Unbe 17a]. Within these studies it was shown, that the proposed vDSA pipeline is able to achieve excellent structural similarity indexes (SSIMs) between 91 % to 99 % w. r. t. to the ground truth.

## 4.7 Conclusion

We proposed a projection image preprocessing pipeline consisting of vessel centerline extraction, lumen segmentation, and background estimation to obtain vDSA images. Both, the coronary artery centerlines as well as the de-truncated vDSA images of the contrasted lumen are used as input to respiratory motion compensation and 3-D reconstruction algorithms that will be presented in Chap. 5, Chap. 6 and Chap. 7, respectively.

# DCM-based Respiratory Motion Compensation

5.1	Introduction .....	41
5.2	Methods .....	41
5.3	Results .....	50
5.4	Discussion .....	50
5.5	Conclusion .....	52

## 5.1 Introduction

This chapter is concerned with the estimation and compensation of intra-scan respiratory motion without the need for prior information on the 3-D topology of the vascular tree. To this end, we devise two [data corruption metric](#) (DCM)-based methods that either exploit redundancies in projection images (cf. Sec. 5.2.1) or impose favorable properties of 3-D space (cf. Sec. 5.2.2) to estimate the respiratory motion of the heart.

## 5.2 Methods

### 5.2.1 ECC-based Correction

As motivated in Sec. 2.5.1, it is known that X-ray projections of the same 3-D object carry redundant information that can be used to define an overall consistency metric (cf. Eq. (2.22)) for a particular acquisition  $\{\mathcal{I}^i | i = 1, \dots, N_\lambda\}$  consisting of  $N_\lambda$  images. Due to the limited [FOV](#) of C-arm [CBCT](#) scanners, projection images of the thorax are truncated. This is problematic, as integrals over epipolar lines would not yield the complete plane integral and would, therefore, be inconsistent even when no other source of corruption such as motion is present. Consequently, we apply [ECC](#) to the sequence of [vDSA](#) images  $\{\mathcal{D}^i | i = 1, \dots, N_\lambda\}$  obtained according to Sec. 4.4.2 rather than the acquired projections [[Unbe 16c](#), [Unbe 17a](#)].

We now introduce a motion model allowing for shifts in detector domain. A motion state is parametrized as  $\gamma \in \mathbb{R}^{N_\lambda \times 1}$ , where  $\gamma_{i,1}$  corresponds to the shift of image  $i$  in



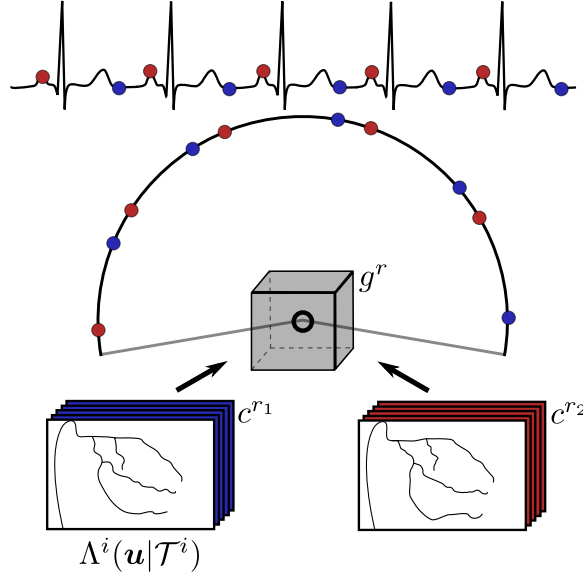


**Figure 5.1:** Images of distinct cardiac phases  $c^r$  are distributed over the scan range. Backprojection following Eq. (5.3) at a specific cardiac phase  $c^r$  yields the corresponding potential map  $g^r$ .

detector  $u_2$ -direction that approximately coincides with the craniocaudal axis of the patient. The model is integrated into the integrals over the epipolar lines yielding

$$\rho_i(\underline{\mathbf{L}}_i^j(\kappa), \gamma) = \iint \mathcal{D}^i(u_1, u_2 + \gamma_{i,1}) \cdot \delta\left((u_1, u_2, 1) \cdot \underline{\mathbf{L}}_i^j(\kappa)\right) du_1 du_2, \quad (5.1)$$

where  $\delta\left((u_1, u_2, 1) \cdot \underline{\mathbf{L}}_i^j(\kappa)\right)$  is the Dirac delta function that evaluates to unity for detector domain points  $(u_1, u_2)^\top \in \mathbb{R}^2$  that lie on the line  $\underline{\mathbf{L}}_i^j(\kappa)$ . Integrating Eq. (5.1) in Eq. (2.22) allows to estimate detector shifts  $\gamma$  such that  $\text{EC}(\{\mathcal{D}^i\}|\gamma)$  is minimized. In the use case presented here, the metric is usually not smooth and exhibits pronounced local minima making gradient-based optimization unfavorable. To account for this issue, we discretize the shifts into multiples of the pixel spacing and sequentially optimize the motion for each image individually using grid search until convergence of global consistency.

For respiratory motion corrected reconstruction, we exploit the convenient property that rigid motion can be directly integrated into the projection matrices. Let  $\mathbf{P}^i$  denote the projection matrix describing the geometry of  $\mathcal{I}^i$  and, consequently,  $\mathcal{D}^i$ . Then, the motion corrected matrix  $\mathbf{P}_E^i$  is given by

$$\mathbf{P}_E^i = \begin{pmatrix} 1 & 0 & 0 \\ 0 & 1 & \gamma_{i,1} \\ 0 & 0 & 1 \end{pmatrix} \cdot \mathbf{P}^i. \quad (5.2)$$

### 5.2.2 AFM-based Correction

The algorithm devised in Sec. 5.2.1 exploits redundancies in projection domain directly, but struggles with in-plane motion due to the circular source orbit [Aich 15a,



Aich 15b, Unbe 16c, Unbe 17a]. To allow for the estimation of more complex motion models, we devise a second motion estimation algorithm based on the concepts of auto-focusing (cf. Sec. 2.5.2). The method operates in reconstruction domain and seeks to optimize a task-based auto-focus measure using  $\alpha$ -expansion moves and graph cuts. To allow for sparse sampling of the projection sequence, we parametrize the motion model using B-splines rather than a sequence of translation vectors.

### 5.2.2.1 Auto-focus Measure

As explained in Sec. 2.5.2, motion compensation based on image sharpness has received increasing attention. Unfortunately, standard measures as studied by Wicklein et al. [Wick 12] or Sisniega et al. [Sisn 16a] are not applicable in the context described here because straight-forward tomographic reconstruction is infeasible. However, as motivated in Sec. 3.5.2.3, sparsifying image processing in projection domain together with modified backprojection operators enable the reconstruction of volumetric potential maps, rather than tomographic images [Jand 09, Li 11]. Properties of aforementioned potential maps directly relate to the quality of symbolic coronary artery reconstructions and can, therefore, be subject to auto-focus measurements.

We use the methods described in Sec. 4.4.1 to extract projection domain centerlines  $\mathcal{T}^i$  in all views  $i = 1, \dots, N_\lambda$  and compute their distance transforms  $\Lambda^i(\mathbf{u}|\mathcal{T}^i)$ . We then apply nearest neighbor gating to extract the sets of images  $\mathcal{C}^r = \{i_1, i_2, \dots\} \subseteq \{1, 2, \dots, N_\lambda\}$  corresponding to all  $R$  target heart phases  $c^r = r/R, r = 1, \dots, R$ . From the distance transforms, the 3-D potential map  $g^r(\mathbf{x})$  at reference heart phase  $c^r$  is given by

$$g^r(\mathbf{x}) = \max_{i \in \mathcal{C}^r} \left( \Lambda^i \left( h(\underline{\mathbf{u}}^i) | \mathcal{T}^i \right) \right), \quad (5.3)$$

where we used  $\underline{\mathbf{u}}^i = \mathbf{P}^i \mathbf{x}$ , the projection of  $\mathbf{x}$  onto image plane  $i$ .

Points exhibiting a very low response  $g^r$  are most likely to belong to the 3-D centerline, however, they are very sparse as Eq. (5.3) allows low responses only at positions that consistently project close to the 2-D centerlines. For symbolic reconstruction in the sense of 3-D minimal path extraction [Jand 09, Li 11] we favor sharp responses with pronounced local minima and design our auto-focus measure accordingly [Unbe 17d]. It is given by

$$a(g^r) = \left( \sum_{i=1}^{H_B} \theta_i \frac{H_i^C(g^r)}{H_i^V(g^r)} \right)^{-1}, \quad (5.4)$$

where  $(H_i^V, H_i^C)$  constitutes the histogram of  $H_B$  intensity bins:  $H_i^V$  represent the histogram intensity values and  $H_i^C$  denote the respective voxel counts. Further,  $\theta_i$  is a bin dependent gain that is tuned to emphasize the importance of low-cost bin counts; details on the choice of  $\theta$  are given in Sec. 5.2.3.  $a(g^r)$  tends to zero with increasing numbers of low cost voxels in  $g^r$ .

### 5.2.2.2 Motion Model, Target Function, and Optimization

We extend the motion model used in Sec. 5.2.1 to allow for reconstruction domain translations. Direct estimation of 3-D shifts for every projection requires a cost function that accounts for every image. This requirement, however, is not practical

because subsequent images correspond to different heart phases that require separate potential maps which drastically increases the computational demand (see Fig. 5.1). Consequently, we express the 3-D shifts  $\gamma \in \mathbb{R}^{N_\lambda \times 3}$  as a B-spline curve

$$\gamma_i(\Phi) = \sum_{k=1}^K \varphi_k \cdot B_{k,d} \left( \frac{i}{N_\lambda} \right), \quad (5.5)$$

where  $\gamma_i \in \mathbb{R}^3$  is the  $i$ -th row of  $\gamma$  corresponding to the 3-D translation associated with frame  $i$ . Further,  $B_{k,d}$  are the B-spline basis functions of degree  $d$  and  $\Phi = \{\varphi_k \in \mathbb{R}^3 | k = 1, \dots, K\}$  is the set of control points, the position of which will be optimized [Stay 12, Pour 16]. This approach is advantageous in two ways. First, it yields inherently smooth displacement sequences for all images. Second, a subset of the images, which is defined by the target heart phases selected, suffices for obtaining a global motion trajectory.

Given the motion model we can formulate the target energy function that we seek to minimize. It reads

$$\text{AF}(\{\Lambda^i\}|\gamma(\Phi)) \equiv \text{AF}(\{\Lambda^i\}|\Phi) = \sum_{k=1}^K D(\varphi_k|\Phi) + \mu_E \sum_{(k,l) \in \Omega} V(\varphi_k, \varphi_l), \quad (5.6)$$

where  $D(\varphi_k|\Phi)$  enforces data fidelity while  $V(\varphi_k, \varphi_l)$  promotes smoothness in neighborhoods  $\Omega$ . The data term reads

$$D(\varphi_k|\Phi) = \frac{1}{R} \sum_{r=1}^R a \left( g^r \circ \Gamma_{(\varphi_k|\Phi)} \right), \quad (5.7)$$

where  $(\varphi_k|\Phi)$  denotes  $\Phi$  with all elements held constant except for  $\varphi_k$ ,  $g^r \circ \Gamma_\Phi$  is the motion compensated 3-D potential map at phase  $r$ :

$$\begin{aligned} \underline{u}^i &= \mathbf{P}^i \Gamma_\Phi(\mathbf{x}, i) = \mathbf{P}^i(\mathbf{x} + \gamma_i(\Phi)), \\ (g^r \circ \Gamma_\Phi)(\mathbf{x}) &= \max_{i \in C^r} \left( \Lambda^i(h(\underline{u}^i)|\mathcal{T}^i) \right), \end{aligned} \quad (5.8)$$

and  $R$  is the number of considered heart phases. Moreover,  $V(\varphi_k, \varphi_l) = \|\varphi_k - \varphi_l\|_2$  is the Euclidean distance between neighboring control points.

Gradient- and grid search-based optimization of Eq. (5.6) is, in general, impractical due to the complex shape and high-dimensional domain of the target function, respectively. However, when exchanging continuous control point locations  $\varphi_k$  with discrete candidates  $\varphi_k^{l_k}$ , Eq. (5.6) takes a form that can be optimized efficiently using the  $\alpha$ -expansion algorithm [Boyk 01]. Rather than directly obtaining optimal control point positions that minimize the energy, we recover optimal labels  $\mathbf{l} = (l_1, \dots, l_K)^\top \in \mathbb{N}^K$  that yield shifts  $\gamma(\Phi_{\mathbf{l}})$ , where  $\Phi_{\mathbf{l}} = \{\varphi_k^{l_k} | k = 1, \dots, K\}$  is the set of control points defined by the current labeling. Put concisely, for all candidate labels  $\alpha \in \{1, \dots, F\}$  we seek to find  $\hat{\mathbf{l}}$  such that

$$\Phi_{\hat{\mathbf{l}}} = \underset{\mathbf{l}'}{\operatorname{argmin}} \text{AF}(\{\Lambda^i\}|\Phi_{\mathbf{l}'}) \quad (5.9)$$

where  $\hat{\mathbf{l}}$  is within one  $\alpha$ -expansion of the current labeling  $\mathbf{l}$ . As for particular control points  $\varphi_k^{l_k}$  the label  $l_k$  either changes to  $\alpha$  or stays the same, each move is essentially a partitioning problem that is solved using a graph cut. A comprehensive description of the algorithm can be found in [Veks 99, Boyk 01].

### 5.2.3 Implementation Details

As outlined in Sec. 5.2.2.2, the  $\alpha$ -expansion algorithm traverses the discretized space and accepts updates that reduce the total energy. Consequently, shifts that yield improvement must lie within the capture range of the optimizer, suggesting that the considered label space must be sufficiently large. To allow for large motion amplitudes while preserving details, we apply optimization on multiple scales by simultaneously increasing the number of control points and heart phases after convergence, such that  $(K, R) \in \{(2, 3), (5, 3), (7, 10)\}$ . At the lowest scale, the control points are initialized to yield zero shift. The discrete samples then cover a  $4 \text{ mm}^3 \times 4 \text{ mm}^3 \times 7 \text{ mm}^3$  neighborhood around the starting positions. The potential map has  $256^3$  voxels with an isotropic size of 0.5 mm.

The bin-dependent gain  $\theta_i$  is selected to heavily favor high counts in low cost histogram bins. It reads

$$\theta_i = \begin{cases} 10 & \text{if } H_i^V < 1 \text{ mm}, \\ 1 & \text{if } 1 \text{ mm} \leq H_i^V < 5 \text{ mm}, \\ 0 & \text{else.} \end{cases} \quad (5.10)$$

As in Sec. 5.2.1, the estimated displacements can be conveniently integrated into the projection matrices. After optimization, the motion corrected matrix  $\mathbf{P}_A^i$  is given by

$$\mathbf{P}_A^i = \mathbf{P}^i \cdot \begin{pmatrix} 1 & 0 & 0 & \gamma_{i,1} \\ 0 & 1 & 0 & \gamma_{i,2} \\ 0 & 0 & 1 & \gamma_{i,3} \\ 0 & 0 & 0 & 1 \end{pmatrix}. \quad (5.11)$$

### 5.2.4 Experiments and Evaluation Metrics

We validate the proposed methods on the CARDBREATH and all three clinical data sets introduced in Sec. 4.2 and Sec. 4.3, respectively. The data sets are preprocessed according to Sec. 4.4. To enable quantitative evaluation and, hence, comparisons between both algorithms, we manually track the 2-D position  $\boldsymbol{\xi}_j^i \in \mathbb{R}^2$  of key points  $j = 1, \dots, Q$ , such as vessel bifurcations, over all frames  $i = 1, \dots, N_\lambda$ .

Unfortunately, direct comparison of the estimated shifts with ground truth is unrewarding, as cardiac motion is non-rigid and, hence, cannot be compensated for by the proposed strategies. An intuitive illustration of this issue is provided in Fig. 5.2. To overcome this fundamental limitation, we evaluate the compensation error for different target heart phases separately. Similar to Sec. 5.2.2.1, we determine the set of corresponding images  $\mathcal{C}^r$  for every of the  $R$  test cardiac phases  $c^r = r/R$  with  $r = 1, \dots, R$  using nearest neighbor ECG-gating. Then, the error  $\varepsilon^P(c^r)$  and  $\varepsilon^R(c^r)$  in projection and reconstruction domain averaged over all tracked points at a given heart phase  $c_r$  reads

$$\varepsilon^{P/R}(c^r) = \sum_{k=1}^R \frac{w_c(r, k)}{\sum_k w_c(r, k)} \left( \frac{1}{Q} \sum_{j=1}^Q [\zeta^{P/R}(\mathcal{C}^r)]_j \right), \quad (5.12)$$

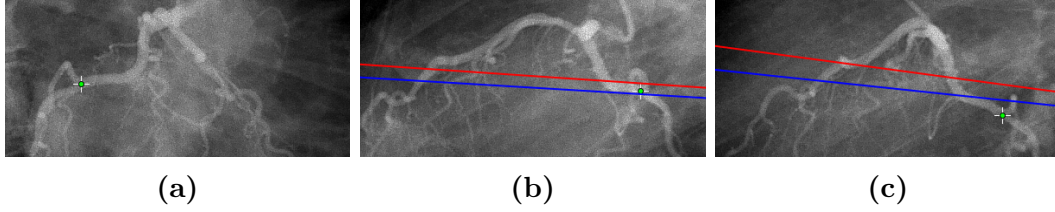


**Figure 5.2:** Illustration of the evaluation strategy described in Sec. 5.2.4. The manually tracked points  $\xi^i$  are highlighted by green markers, where  $i \in \{i_1, i_2, i_3\}$  denote Fig. 5.2a, Fig. 5.2b, and Fig. 5.2c, respectively. Using the original projection matrices, the key point  $\xi^{i_1}$  maps to the red epipolar lines in images  $i_2$  and  $i_3$ . After compensation, the same key point maps to the blue epipolar lines. Images  $i_1$  and  $i_2$  correspond to the same cardiac phase  $c^r$ . The rightmost image  $i_3$ , however, corresponds to a drastically different phase and shows residual mismatch between the compensated epipolar line and the tracked key point. This observation highlights the influence of cardiac motion and motivates the use of gating weights in Eq. (5.13).

where  $\zeta^{P/R}$  is the projection and reconstruction domain error within a particular gate that is computed as detailed below. To obtain smooth curves,  $R$  is set to 100. Moreover, we accumulate the weighted error within a small window around the target heart phase where the weights are given by Eq. (3.1) using  $w_g = 0.4$  and  $a_g = 4$ . We evaluate both error metrics using the original geometry, and the corrected geometries obtained using ECC and AFM. They will be referred to as  $\varepsilon$ , and  $\varepsilon_E$  and  $\varepsilon_A$ , respectively.

#### 5.2.4.1 Projection Domain Error

The projection domain error  $[\zeta^P(C^r)]_j$  of key point  $\xi_j$  in gate  $C^r$  relies on the epipolar geometry between pairs of views (cf. Fig. 2.5 and Fig. 3.3). Specifically, it accumulates violations of the epipolar constraint such that

$$[\zeta_P(C^r)]_j = \frac{2!(|C^r| - 2)!}{|C^r|!} \sum_{\substack{i_1, i_2 \in C^r \\ i_1 < i_2}} \left| \underline{\xi}_j^{i_1 \top} \cdot \mathbf{F}_{i_2}^{i_1} \cdot \underline{\xi}_j^{i_2} \right|, \quad (5.13)$$

where  $\mathbf{F}_{i_2}^{i_1} \in \mathbb{R}^{3 \times 3}$  is the fundamental matrix between views  $i_1$  and  $i_2$  that is computed from the projection matrices [Hart 04, Aich 15a]. Evaluating the proposed methods is implicit, as the motion is encoded in the projection matrices and, consequently, in the fundamental matrix.

#### 5.2.4.2 Reconstruction Domain Error

It seems natural that 3-D points triangulated from corresponding 2-D observations using the epipolar geometry [Hart 04] should coincide in reconstruction domain. In presence of intra-scan motion, this assumption does not hold and the triangulated 3-D points are distributed around the true position. As the true mean of this distribution is unknown, it cannot be used to quantify the corruption. The variance of the distribution, however, can be computed from the observations and is related to the

corruption of the sequence.

Let  $\mathbf{x}_j^{(i_1, i_2)} \in \mathbb{R}^3$  denote the 3-D point that arises from triangulation of  $\boldsymbol{\xi}_j$  from views  $i_1$  and  $i_2$ . Then, the reconstruction domain error is computed as

$$[\zeta_{\text{R}}(\mathcal{C}^r)]_j = \text{var} \left( \left\{ \mathbf{x}_j^{(i_1, i_2)} \mid i_1, i_2 \in \mathcal{C}^r \wedge i_1 < i_2 \right\} \right)^{1/2}, \quad (5.14)$$

where  $\text{var}(\{\mathbf{x}^{(i_1, i_2)}\})$  computes the variance among the set of triangulated points. Similarly to the projection domain error, the motion correction is evaluated implicitly by using the corrected projection matrices to triangulate the 3-D points.

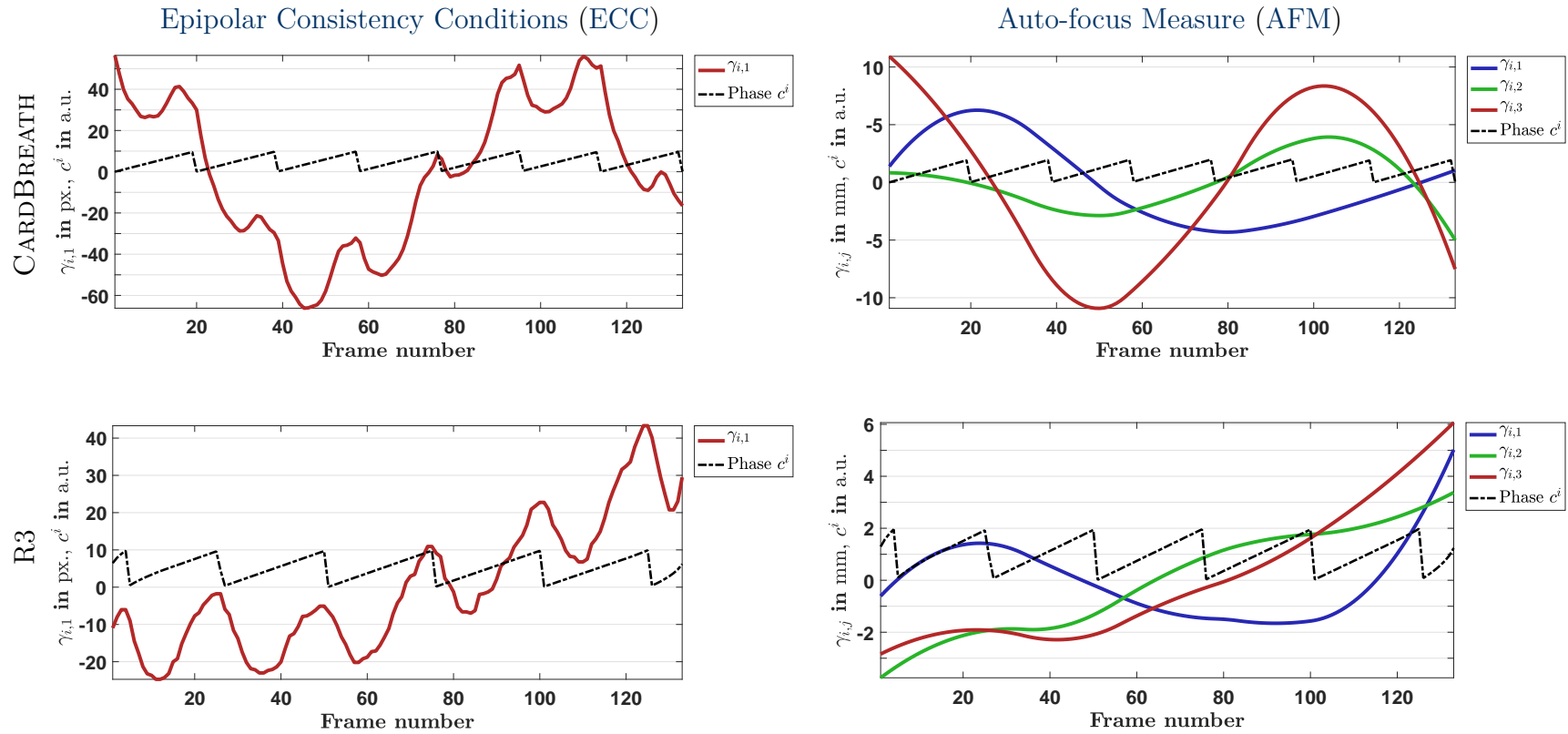


**Figure 5.3:** Motion patterns estimated from optimization of ECC (left column) and AFM (right column) for the phantom (top row) and the clinical data (bottom row), respectively, together with the corresponding cardiac phase information.

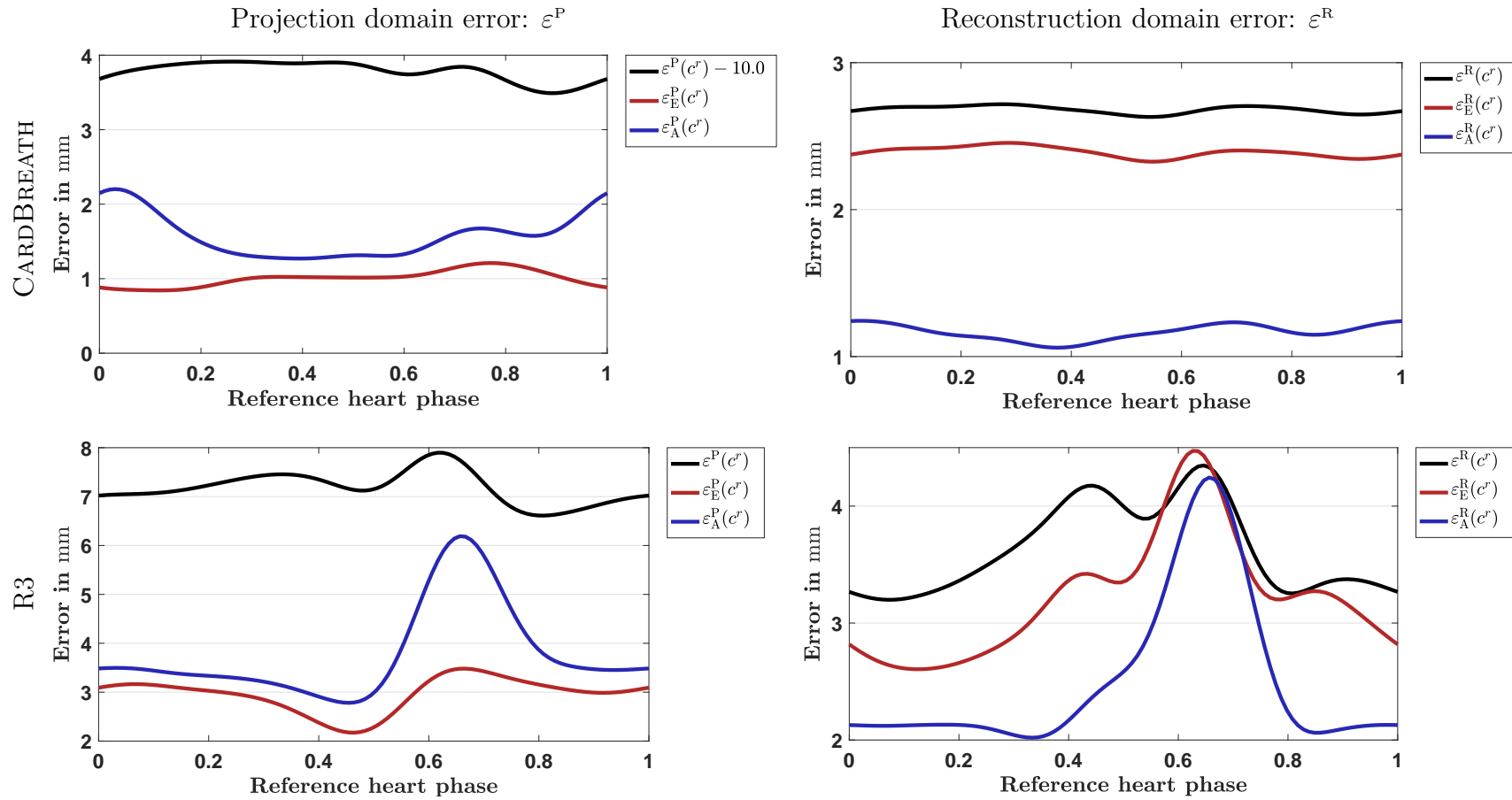


**Figure 5.4:** Representative error curves for both the phantom (top row) and the clinical data (bottom row). Errors obtained using the projection and reconstruction domain metric are shown on the left and the right hand side, respectively. Note that uncompensated projection domain error curve for CARDBREATH was shifted downward by 10 mm to allow for better visualization.

**Table 5.1:** Projection domain errors computed according to Eq. (5.13). We state the average and standard deviation over all heart phases, and the minimal value in brackets. All errors are stated in mm.

	$\varepsilon^P$	$\varepsilon_E^P$	$\varepsilon_A^P$
CARDBREATH	$13.8 \pm 0.1$ (13.5)	$1.01 \pm 0.11$ (0.84)	$1.58 \pm 0.29$ (1.27)
R1	$1.65 \pm 0.53$ (1.00)	$1.02 \pm 0.13$ (0.84)	$1.33 \pm 0.40$ (0.77)
R2	$1.87 \pm 0.20$ (1.58)	$1.45 \pm 0.17$ (1.17)	$1.54 \pm 0.31$ (1.18)
R3	$7.18 \pm 0.33$ (6.61)	$2.96 \pm 0.35$ (2.17)	$3.77 \pm 0.93$ (2.78)

**Table 5.2:** Reconstruction domain errors computed according to Eq. (5.14). We state the average and standard deviation over all heart phases, and the minimal error in brackets. All errors are stated in mm.

	$\varepsilon^R$	$\varepsilon_E^R$	$\varepsilon_A^R$
CARDBREATH	$2.68 \pm 0.03$ (2.63)	$2.39 \pm 0.04$ (2.33)	$1.17 \pm 0.05$ (1.06)
R1	$1.68 \pm 0.33$ (1.21)	$1.58 \pm 0.23$ (1.19)	$1.63 \pm 0.35$ (1.19)
R2	$2.28 \pm 0.64$ (1.38)	$1.66 \pm 0.22$ (1.35)	$1.60 \pm 0.17$ (1.35)
R3	$3.63 \pm 0.38$ (3.20)	$3.22 \pm 0.51$ (2.61)	$2.50 \pm 0.66$ (2.02)

## 5.3 Results

Motion patterns estimated using ECC and AFM according to Sec. 5.2.1 and Sec. 5.2.2 for the phantom study and a representative clinical data set are shown in Fig. 5.3. For the same representative data sets, we also show the projection and reconstruction domain error curves computed according to Sec. 5.2.4.1 and Sec. 5.2.4.2. Finally, we report the results of the quantitative assessment of projection and reconstruction domain errors in Tab. 5.1 and Tab. 5.2, respectively. We observed substantial reductions in mean and minimum values of both target errors for all studied cases.

## 5.4 Discussion

### 5.4.0.3 Motion Patterns and Target Errors

From Tab. 5.1 it is apparent that the corruption due to respiratory motion among the clinical cases is most dramatic for R3. Cases R1 and R2 exhibit residual respiratory motion only while scan R3 suffers from heavy intra-scan respiratory motion. As the *in silico* phantom exhibits substantial corruption due to respiration, we have selected R3 for qualitative comparisons of the estimated motion patterns and error curves.

It is obvious from Fig. 5.3 that the S-I component of the motion patterns estimated with ECC and AFM ( $\gamma_{i,1}$  and  $\gamma_{i,3}$ , respectively) qualitatively are in very good agreement for both phantom and clinical data. However, while AFM yields smooth curves, optimization of ECC results in low frequency signals that are superimposed with a high frequency signal that originates from the S-I motion of the heart during contraction [Shec06, Unbe17a]. This behavior is to be expected, as the current formulation of  $EC(\{\mathcal{D}^i\}|\gamma)$  according to Eq. (2.22) and Eq. (5.1) does not incorporate gating



weights. Although the high frequency component corresponding to cardiac motion cannot be used for motion correction, it proved useful for the derivation of an image-based surrogate signal for the cardiac phase [Unbe 16c, Unbe 17a]. This fact can be appreciated when comparing the position of the local maxima w.r.t. to the maxima of the sawtooth wave corresponding to the cardiac phase in Fig. 5.3.

Improvements of the projection domain error are  $(53.0 \pm 14.4) \%$  and  $(43.3 \pm 33.1) \%$  for ECC and AFM, respectively, suggesting that optimizing for 3-D rather than 1-D translational motion proved disadvantageous. When considering circular source trajectories, the reason for this behavior is easily understood. Extending detector  $u_2$  shifts to 3-D translations adds degrees of freedom in the plane orthogonal to the rotation axis that, when projected, imply shifts along the  $u_1$  axis. It is known that epipolar lines are approximately parallel to the  $u_1$  direction even for large primary angle increments [Unbe 16b]. As the projection domain metric is unaffected by shifts along epipolar lines, potential improvements due to additional flexibility in the  $x_1$ - $x_2$ -plane are mitigated by imperfect solutions to the more complex optimization problem. It is worth mentioning that, despite the previous reasoning, both methods yield very comparable minimal errors (cf. Tab. 5.1).

Considering the reconstruction domain error it becomes apparent that additional flexibility of the motion model as for AFM is, in fact, beneficial: optimizing for ECC and  $u_2$  shifts yields an average decrease of  $(12.0 \pm 10.5) \%$  while estimating 3-D translations based on AFM resulted in a substantially larger improvement of  $(28.7 \pm 21.9) \%$ . In contrast to the projection domain error, this trend is also reflected in the minimal error measures.

When considering the motion compensation error at specific heart phases shown in Fig. 5.4, we observed comparable errors throughout most of the cardiac cycle with the highest discrepancies around ventricular systole ( $c^r \sim 0.5 - 0.7$ ). This result is to be expected, as residual cardiac motion within gates is most prominent during systole [Shec 06, Schw 13b].

It is worth mentioning that the quantitative errors reported in Tab. 5.1, Tab. 5.2, and Fig. 5.4 depend on the choice of gating parameters, as they influence the weighting used in Eq. (5.12). Wider gating windows increase the residual motion contained in each gate which would, therefore, result in higher errors. Within this thesis, we used nearest neighbor gating, however, cosine function-based weighting may be of interest. In that case,  $a_g = 4$  and  $w_g = 0.4$  may constitute a reasonable compromise between heart phase sensitivity and residual cardiac motion [Schw 13a, Unbe 15c].

The reduction in error achieved for the clinical cases is substantial, yet average minimal errors (cf. Fig. 5.4) remain. This residual error is a composite of three different sources of error: incorrect estimates  $\gamma$ , a finite gating window width, but also inaccuracies in manual key point tracking. Incorrect key point positions impose a fundamental lower bound on error reduction, unfortunately, direct assessment of this systematic error is not possible for the real data cases. Previous results obtained on different phantom data, however, suggest that very accurate motion compensation even below the pixel or voxel size is possible with the proposed methods [Unbe 17a, Unbe 17d].

#### 5.4.0.4 Limitations and Challenges

First, the current optimizations described in Sec. 5.2.1 and Sec. 5.2.2 do not inhibit a systematic shift of all detectors. Such shift is bounded by the maximally occurring motion and would introduce cone-beam artifacts, the effect of which is negligibly compared to the drastic motion artifacts. However, at least the ECC-based method is, in principle, able to optimize for systematic drifts [Debb 13], an extension that should be considered for future work.

Second, within this work we optimized for S-I shifts and 3-D translational motion only, motion models that may not be sufficient in the most general case [Shec 06]. Compensation of the dominant motion components as proposed here may allow for initial reconstructions and, therefore, enable methods based on 3-D/2-D registration that allow for more complex motion models [Shec 04, Blon 06, Bros 10, Baka 14, Baka 15]. Finally, the phantom experiment was restricted to a recurring breathing cycle, an assumption that was motivated by free-breathing imaging. In previous work, we showed that the proposed methods are fit to handle both recurring and incomplete breathing cycles [Unbe 16c, Unbe 17a, Unbe 17d], yet, a more exhaustive evaluation on real data remains subject of future work.

## 5.5 Conclusion

In summary, we proposed two DCM-based algorithms targeted at intra-scan motion assessment in rotational coronary angiography. The methods do not require prior 3-D models of the coronary anatomy as they exploit redundancies in X-ray transmission imaging and favorable properties of reconstructed images, respectively. All figures of merit suggested good performance for both phantom and clinical cases.

The current evaluation was performed on sparse key points that were manually tracked over the image sequence. Although the results are very promising, it is not yet clear how the improvements in target error achieved by both methods translate to 3-D image quality, a shortcoming that we seek to address in the forthcoming chapters.

# Tomographic Coronary Artery Reconstruction

6.1	Introduction .....	53
6.2	Methods .....	54
6.3	Results .....	58
6.4	Discussion .....	61
6.5	Conclusion .....	63

## 6.1 Introduction

Tomographic reconstruction from rotational angiography is very challenging, as the algorithms devised for 3-D reconstruction need to account for diverse sources of image corruption (cf. Sec. 2.4), such as truncation, and respiratory and cardiac motion. In Chap. 4 and Chap. 5, we presented methods that effectively eliminate truncation and correct for intra-scan respiratory motion, respectively.

As motivated in Sec. 3.3, the most influential problem that inhibits tomographic reconstructions of high quality is angular undersampling due to cardiac gating. A common strategy to overcome this limitation is to incorporate all available views. In order to do so, state-of-the-art methods rely on deformable 3-D/2-D registration to correct for intra-scan cardiac motion. Such approaches were shown to be very effective [Scha06, Rohk10b, Schw13a, Liu16], yet, come at a very high computational cost.

In this chapter, we employ novel iterative reconstruction algorithms that exploit image properties in spatial and, more importantly, temporal domain [Taub17a, Taub17c]. In addition to employing *spatial* regularizers used in compressed sensing such as (spatial) **total variation** (TV) minimization [Sidk08, Wu11], these methods reconstruct images at multiple cardiac phases simultaneously while allowing for communication among them using *temporal* regularizers. Therefore, they implicitly address the problem of insufficient data more effectively [Taub16, Taub17a, Taub17c].

Ultimately, the method devised in this chapter will be used to conduct a task-based evaluation of the respiratory motion compensation methods proposed previously.

## 6.2 Methods

### 6.2.1 Gating

The proposed algorithm simultaneously reconstructs 3-D volumes containing the coronary arteries at different cardiac phases. Each of the  $R$  volumes is reconstructed from very few images that are determined using nearest neighbor gating. As introduced in Sec. 5.2.2.1, the set of images corresponding to a particular target heart phase  $c^r = r/R$  is given by  $\mathcal{C}^r = \{i_1, i_2, \dots\} \subseteq \{1, 2, \dots, N_\lambda\}$ , where  $r = 1, \dots, R$ .

### 6.2.2 Truncation correction

Severe lateral truncation proved to be a substantial problem for tomographic coronary artery reconstruction. It is usually addressed by preprocessing the projection images with top-hat filters that, on the one hand, mitigate the problems due to truncation but, on the other hand, introduce inconsistency w. r. t. to the image formation theory (cf. Sec. 3.2). In Sec. 4.4, we developed a sophisticated method for truncation removal via background subtraction that proved sufficient for the application of CC. Therefore, rather than reconstructing the heavily truncated projections  $\mathcal{I}^i$  directly, we operate on the vDSA images  $\mathcal{D}^i$  obtained according to Sec. 3.2.1.

### 6.2.3 Limited Grid Size Correction

Simultaneous iterative reconstruction of time-resolved 3-D volumes including regularizers is associated with memory requirements of several times the size of the image to be recovered. Consequently, hardware limitations often prohibit the reconstruction of ROIs that contain the whole object [Rit09a]. This is not problematic for analytic, one-shot reconstruction algorithms such as the FDK, because every voxel is updated independently. However, it is of importance in iterative methods that rely on repeated forward projections of intermediate image estimates.

Taubmann et al. proposed a simple, yet effective method to correct for truncation resulting from limited grid sizes in 4-D iterative reconstruction [Taub17b]. Assuming that the region outside the ROI corresponds to background that is static, the correction term can be precomputed and applied independently of the dynamic reconstruction. It comprises of the following steps:

1. On a grid considerably larger than the ROI, reconstruct a static image  $\mathbf{f}_{\text{static}}$  from the projection data  $\mathcal{D}$  by, e. g., minimizing Eq. (2.19).
2. Separate  $\mathbf{f}_{\text{static}}$  into two images:  $\mathbf{f}_{\text{ROI}}$  corresponding to the ROI that will be reconstructed dynamically later, and  $\mathbf{f}_{\text{BG}}$  that represents the background.
3. Compute the corrected projections  $\mathcal{D} = \mathcal{D}' - \mathbf{M}\mathbf{f}_{\text{BG}}$ , where  $\mathbf{M} \in \mathbb{R}^{N_\lambda \cdot N_u \times N_x}$  encodes the geometry and  $\mathcal{D}' \in \mathbb{R}^{N_u \cdot N_\lambda}$  is a vectorized version of the set of vDSA images.

Aforementioned correction proved particularly beneficial for sequences corrupted by severe lateral truncation [Taub17b]. Due to prior truncation correction using vDSA

imaging, we do not anticipate substantial image content outside the central ROI. However, the **vDSA** sequences may still contain artifacts due to erroneous segmentation or imperfect inpainting. These inconsistencies can be accounted for using the correction scheme above.

### 6.2.4 Spatially and Temporally Regularized Reconstruction

We adapt the formulation of iterative reconstruction developed in Sec. 2.3.2 to allow for simultaneous 4-D reconstruction. Again, we seek to find an optimal solution to the minimization problem

$$\operatorname{argmin}_{\mathbf{f}} D(\mathbf{f}) + R(\mathbf{f}) = \operatorname{argmin}_{\mathbf{f}} \frac{1}{2} \|\mathbf{M}\mathbf{f} - \mathcal{D}\|_2^2 + R(\mathbf{f}), \quad (6.1)$$

where we use the squared residual to enforce data fidelity while  $R(\mathbf{f})$  encodes regularizers. In contrast to Eq. (2.17), we are now considering a dynamic, 4-D object  $\mathbf{f} \in \mathbb{R}^{R \cdot N_x}$  that is reconstructed from  $\mathcal{D} \in \mathbb{R}^{N_u \cdot N_\lambda}$ , the vectorized version of the set of **vDSA** images after correction according to Sec. 6.2.3. The geometry of the tomography problem is encoded in the system matrix  $\mathbf{M} \in \mathbb{R}^{N_\lambda \cdot N_u \times R \cdot N_x}$ , a discrete representation of the projection operator, associating the 4-D image  $\mathbf{f}$  with the pre-processed data  $\mathcal{D}$ .

For spatially and temporally regularized reconstruction, the regularization terms consist of a non-negativity constraint  $\iota_{\mathbb{R}_+}(\mathbf{f})$ , the **sTV** norm  $\|\mathbf{f}\|_{\text{sTV}}$ , and, most importantly, the **tTV** norm  $\|\mathbf{f}\|_{\text{tTV}}$  [Taub17a, Taub17c]. As before, the **sTV** norm is computed as  $\|\mathbf{f}\|_{\text{sTV}} = \|\mathbf{D}_s \mathbf{f}\|_{1,2}$ , however, using a slightly modified version of the element-wise spatial forward difference operator  $\mathbf{D}_s$  that is given by

$$\mathbf{D}_s : f_{x_1, x_2, x_3, r} \mapsto \begin{bmatrix} f_{x_1+1, x_2, x_3, r} - f_{x_1, x_2, x_3, r} \\ f_{x_1, x_2+1, x_3, r} - f_{x_1, x_2, x_3, r} \\ f_{x_1, x_2, x_3+1, r} - f_{x_1, x_2, x_3, r} \end{bmatrix} \quad (6.2)$$

to account for the 4-D nature of  $\mathbf{f}$ . Similarly, the **tTV** norm of image  $\mathbf{f}$  is given by  $\|\mathbf{f}\|_{\text{tTV}} = \|\mathbf{D}_t \mathbf{f}\|_1$ , where  $\mathbf{D}_t$  computes element-wise forward differences in temporal domain

$$\mathbf{D}_t : f_{x_1, x_2, x_3, r} \mapsto f_{x_1, x_2, x_3, r+1} - f_{x_1, x_2, x_3, r} \quad (6.3)$$

with periodic boundary condition to account for the periodicity of cardiac motion. With these definitions, the complete minimization problem reads

$$\operatorname{argmin}_{\mathbf{f}} \frac{1}{2} \|\mathbf{M}\mathbf{f} - \mathcal{D}\|_2^2 + \mu_s \cdot \|\mathbf{f}\|_{\text{sTV}} + \mu_t \cdot \|\mathbf{f}\|_{\text{tTV}} + \iota_{\mathbb{R}_+}(\mathbf{f}), \quad (6.4)$$

where  $\mu_s, \mu_t \geq 0$  are weights associated with the spatial and temporal regularization terms, respectively.

### 6.2.5 Primal-Dual Optimization

Eq. (6.4) consists of a smooth, differentiable part  $D(\mathbf{f})$  and of non-smooth but proximable operators, albeit in linearly transformed domains in case of the  $L^1$  components.

This type of function qualifies for optimization using a proximal splitting algorithm derived by Condat [Cond 13] that proved effective in the case of TV regularized inverse problems [Cond 14, Taub 17a]. Due to its full-splitting approach, it does not require nested loops to approximate the TV proximal operator, which has no closed form solution. For the task of minimizing Eq. (6.4), the updates consist of:

1.  $\mathbf{f}_{\text{prev}} \leftarrow \mathbf{f}$
2. The primal update step  $\mathbf{f} \leftarrow \left( \mathbf{f} - \tau_p \left( \mathbf{M}^\top (\mathbf{M}\mathbf{f} - \mathbf{D}) + \mathbf{D}_s^\top \mathbf{G}_s + \mathbf{D}_t^\top \mathbf{G}_t \right) \right)_+$ , where  $\tau_p$  is the primal step length,  $\mathbf{G}_s \in \mathbb{R}^{3 \cdot R \cdot N_x}$  and  $\mathbf{G}_t \in \mathbb{R}^{R \cdot N_x}$  are dual variables corresponding to the spatial and temporal gradients, and  $(\cdot)_+ : f \mapsto \max(f, 0)$  is the proximal operator of  $\iota_{\mathbb{R}_+}(\cdot)$  and enforces the non-negativity constraint.
3. A dual update  $\mathbf{G}_s \leftarrow \text{prox}_{\tau_d(\mu_s \|\cdot\|_{1,2})^*} \left( \mathbf{G}_s + \tau_d \mathbf{D}_s (2 \cdot \mathbf{f} - \mathbf{f}_{\text{prev}}) \right)$ , with dual step length  $\tau_d$ . Moreover,  $\text{prox}_{\tau_d(\mu_s \|\cdot\|_{1,2})^*} : \mathbf{g} \mapsto \mathbf{g} / \max(\|\mathbf{g}\|_2 / \mu_s, 1)$ , is the proximal operator of the sTV norm and can be understood as the projection of each component vector  $\mathbf{g}$  in  $\mathbf{G}_s$  onto a ball with radius  $\mu_s$ .
4. Another dual update  $\mathbf{G}_t \leftarrow \text{prox}_{\tau_d(\mu_t \|\cdot\|_1)^*} \left( \mathbf{G}_t + \tau_d \mathbf{D}_t (2 \cdot \mathbf{f} - \mathbf{f}_{\text{prev}}) \right)$ , using the proximal operator of the tTV norm  $\text{prox}_{\tau_d(\mu_t \|\cdot\|_1)^*} : \mathbf{g} \mapsto \mathbf{g} / \max(\|\mathbf{g}\|_1 / \mu_t, 1)$ .

The primal and dual step lengths are chosen to satisfy the convergence criterion  $\tau_p \left( \frac{\beta}{2} + \tau_d \|\mathbf{D}_s^\top \mathbf{D}_s + \mathbf{D}_t^\top \mathbf{D}_t\| \right) < 1$ , where  $\|\cdot\|$  is the operator norm, and  $\beta$  is the Lipschitz constant of  $\nabla_{\mathbf{f}}(\mathbf{f}) = \mathbf{M}^\top (\mathbf{M}\mathbf{f} - \mathbf{D})$ , the backprojection of the residual error  $\mathbf{M}\mathbf{f} - \mathbf{D}$  [Cond 14]. Primal updates following an ordered subsets scheme have been found beneficial [Byrn 02], but are not necessary in this case due to favorable angular distributions arising from gating [Taub 17a].

For a comprehensive derivation of the algorithm including a proof of convergence we refer the reader to [Cond 13, Cond 14].

## 6.2.6 Experiments

We reconstruct the coronary arteries using a streak-reduced, ECG-gated FDK algorithm (cf. Eq. (3.2) in Sec. 3.5.1) and the proposed, spatially and temporally regularized iterative method using the uncompensated projection matrices  $\{\mathbf{P}^i\}$ , and the respiratory motion compensated matrices  $\{\mathbf{P}_E^i\}$  and  $\{\mathbf{P}_A^i\}$ , respectively. The reconstructions are performed on a  $256^3$  grid with an isotropic voxel size of 0.5 mm using 300 iterations. Feasible values for the weights  $\mu_s$  and  $\mu_t$  are determined in a grid search.

### 6.2.6.1 Numerical Phantom Studies

For the CAVAREV data set, it has been shown that simple top-hat filtering is sufficient to achieve acceptable results [Rohk 11, Schw 13a, Unbe 16a] suggesting that the *in silico* phantom does not sufficiently reflect the key challenges associated with clinical cases, such as high noise levels and poor vessel contrast. To achieve better comparability to the clinical cases, where a potentially high artifact level in the vDSA

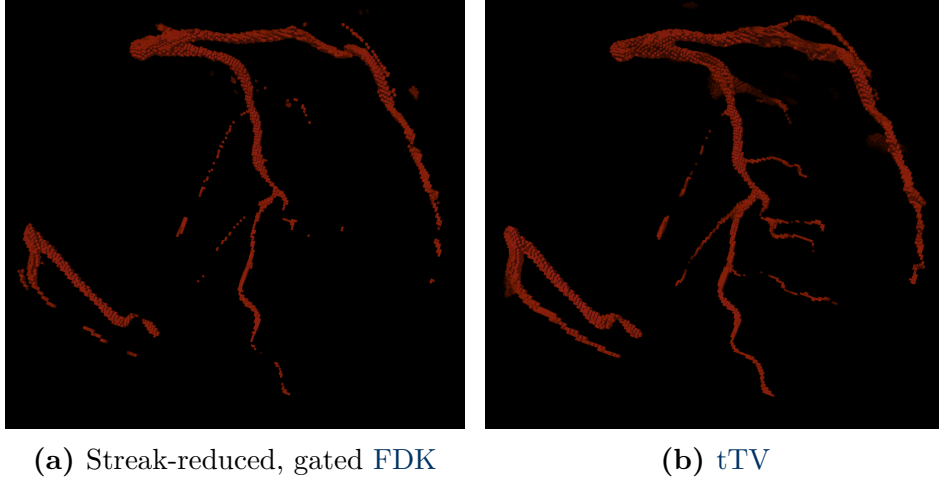


**Figure 6.1:** Volume renderings of tomographic reconstructions of the *in silico* phantom data set containing cardiac motion only CARD. Fig. 6.1a was obtained using streak-reduced, ECG-gated FDK, while Fig. 6.1b was reconstructed using the tTV regularized iterative method.

images introduces inconsistency, reconstruction is performed on the acquired projections  $\{\mathcal{I}^i\}$  directly, rather than relying on the vDSA images  $\{\mathcal{D}^i\}$ . Both phantom data sets CARD and CARDBREATH are reconstructed using  $R = 19$  gates simultaneously.

Quantitative assessment is performed based on the evaluation framework associated with the CAVAREV data set, that is based on the Dice similarity coefficient [Sore48], that measures the overlap between two binarized images and ranges between zero (no overlap) to unity (perfect match). Although the ground truth provided by CAVAREV is binary, reconstructed images  $f$  are not. To overcome this limitation,  $f$  is repeatedly binarized using a sweeping intensity threshold and then compared to the ground truth morphology  $g_c^i$  in all motion states (i.e., projection images)  $i$ . As the final score, CAVAREV selects the best value over all thresholds and motion states [Rohk10c].

We reconstruct and evaluate data set CARD using a state-of-the-art analytic and the proposed method to establish an upper bound on the achievable image quality. Subsequently, we assess the reconstruction performance in presence of respiratory motion using CARDBREATH that is reconstructed using uncompensated, and ECC and AFM corrected projection matrices. In agreement with the literature, we select a cardiac phase at end diastole for the quantitative assessment.

### 6.2.6.2 Clinical Data

In order to assess the applicability of the proposed methods to real-world scans, we reconstruct the three clinical scans described in Sec. 4.3 with and without the proposed respiratory motion compensation strategies using  $R = 27$  gates. In agreement with the description in Sec. 6.2.2, we use the vDSA images as input to the reconstruction algorithms. As no ground truth data is available, we limit our analysis to a



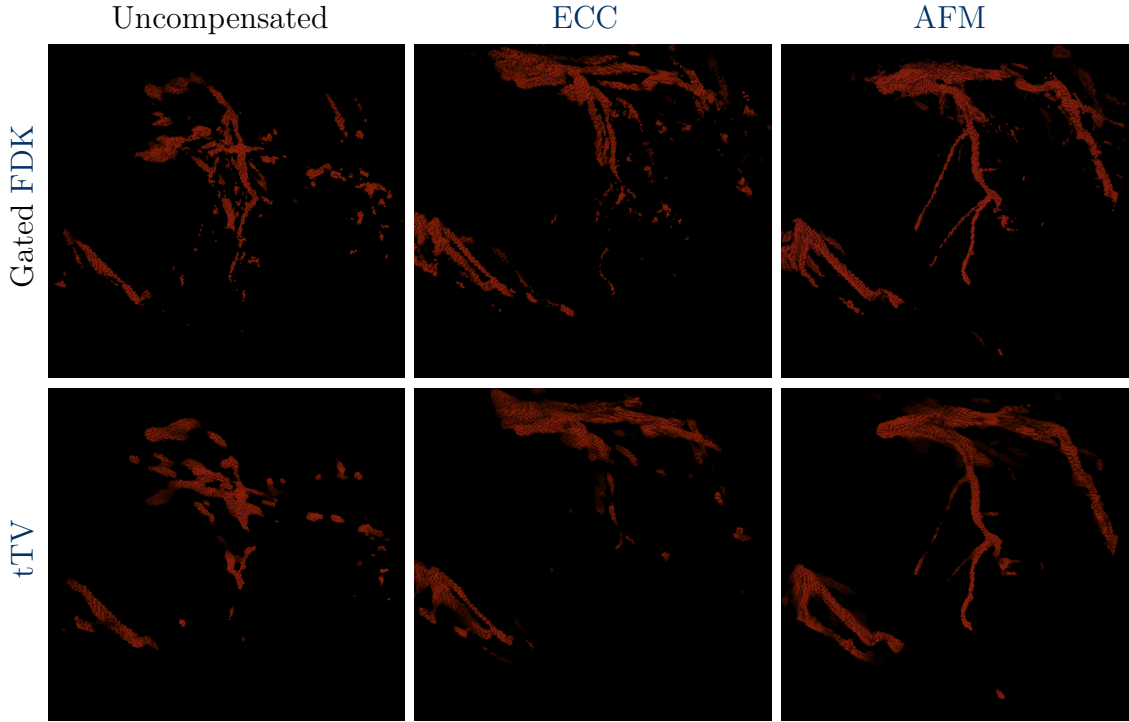


**Figure 6.2:** Volume renderings of reconstructions of CARDBREATH obtained using the proposed respiratory motion compensation strategies. From left to right, we show results obtained with the original, and the ECC and AFM corrected geometry. Results in the top row are reconstructed using streak-reduced, gated FDK while images in the bottom row are reconstructed using the proposed iterative method.

qualitative assessment by visual inspection of the reconstruction results at a diastolic heart phase.

## 6.3 Results

### 6.3.1 Phantom Data

Reconstructions of data set CARD using streak-reduced, gated FDK and tTV regularized iterative reconstruction are shown in Fig. 6.1a and Fig. 6.1b, respectively. The coronary arteries appear more complete and exhibit less artifact for the proposed method, which is also reflected in a substantially higher overlap with the CAVAREV ground truth of 81.2 % compared to 76.0 %.

Quantitative and qualitative results of the study assessing reconstruction quality in combination with respiratory correction on CARDBREATH are given in Tab. 6.1 and Fig. 6.2. Dice scores are consistently higher for tTV regularized reconstruction. Respiratory motion compensation using ECC and AFM substantially increased the overlap with the ground truth, with AFM considerably outperforming the ECC-based correction. All quantitative results are in very good agreement with the visual impressions.



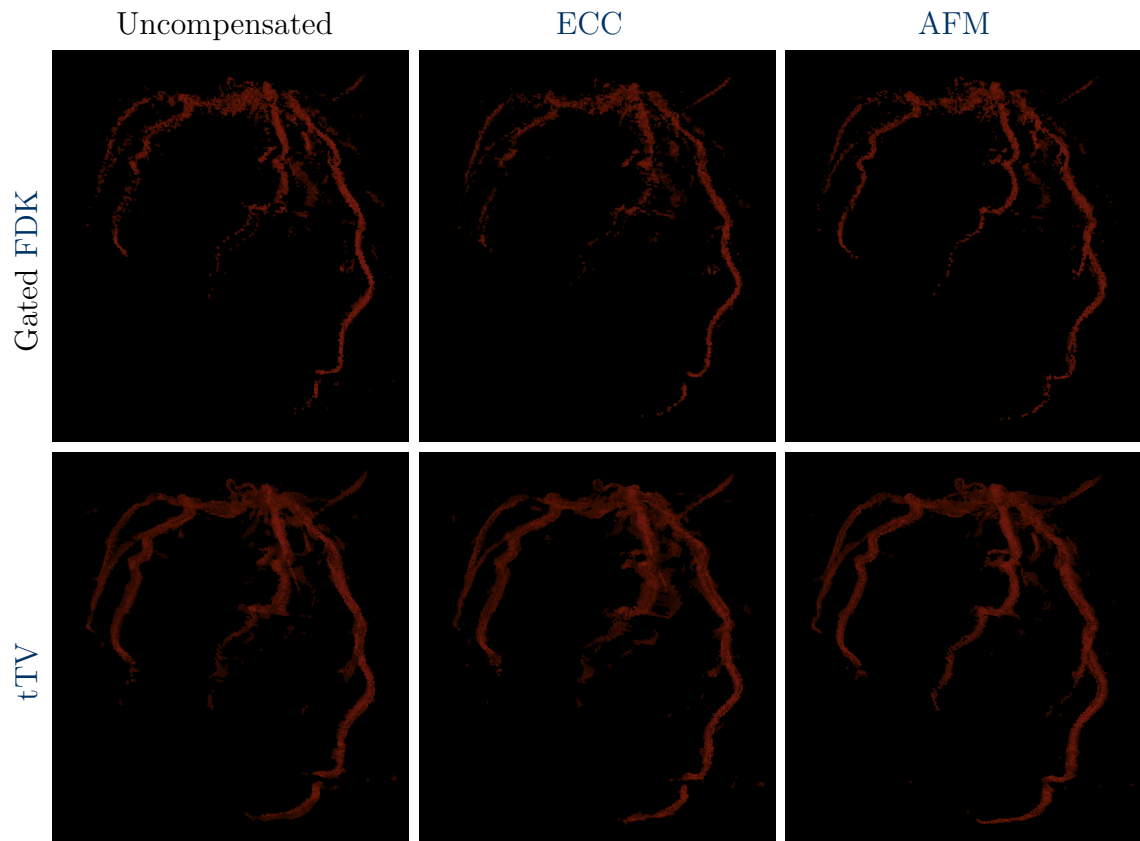


**Figure 6.3:** Volume renderings of clinical data set R1 using streak-reduced, gated **FDK** in the top and **sTV** and **tTV** regularized iterative reconstruction in the bottom row, respectively. From left to right, we show results obtained with the uncompensated matrices, and the **ECC** and **AFM** corrected geometry.

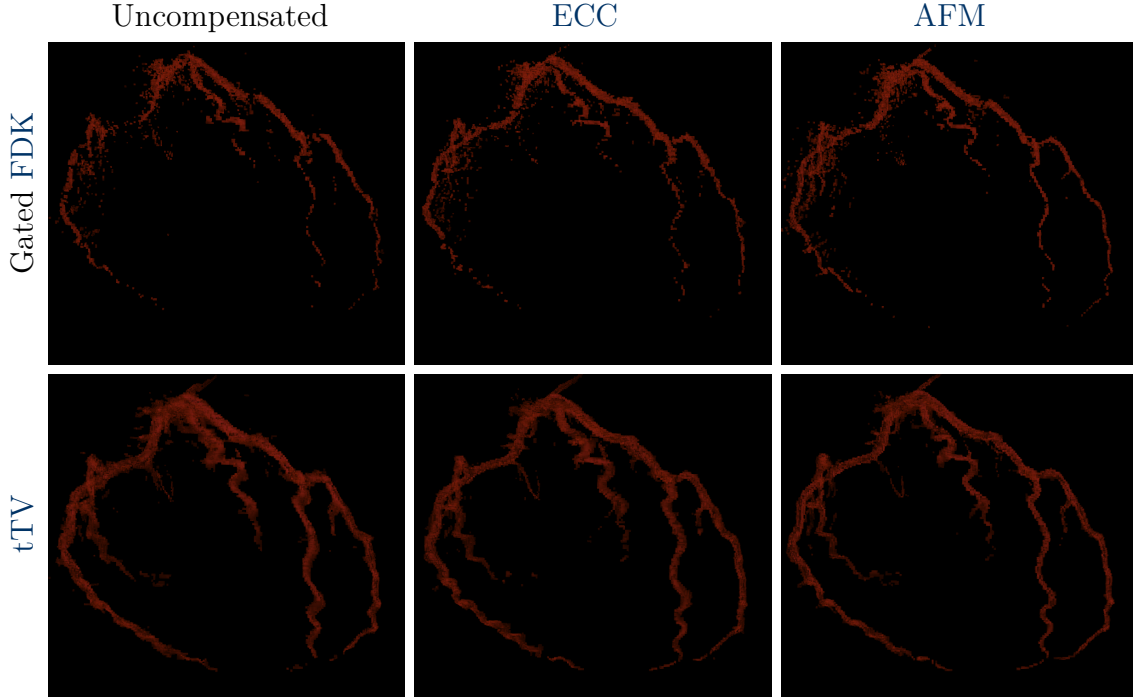


**Figure 6.4:** Renderings of clinical data set R2 using streak-reduced, gated **FDK** in the top and the proposed iterative reconstruction in the bottom row, respectively. From left to right: reconstructions using the uncompensated matrices, and the **ECC** and **AFM** corrected geometry.

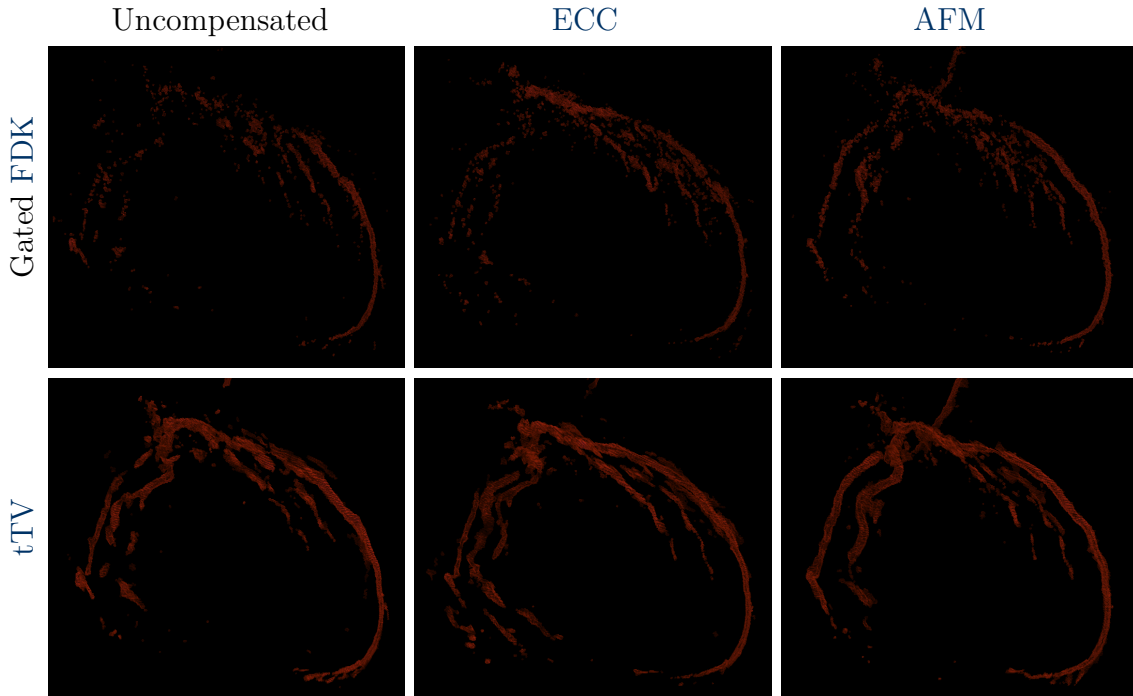


**Figure 6.5:** Visualization of clinical data set R3 reconstructed using a state-of-the-art analytic method in the top and the novel iterative reconstruction algorithm in the bottom row, respectively. From left to right: reconstructions using the uncompensated matrices, and the **ECC** and **AFM** corrected geometry.

**Table 6.1:** CAVAREV Dice scores achieved with analytic and iterative reconstruction algorithms using the respiratory motion compensation schemes described in Chap. 5.

	Uncompensated	ECC	AFM
Gated FDK	21.0 %	27.9 %	44.0 %
tTV	25.1 %	30.7 %	46.3 %

### 6.3.2 Clinical Data

We show volume renderings of volumes reconstructed with and without respiratory motion compensation using streak-reduced, gated FDK and the proposed method for R1, R2, and R3 in Fig. 6.3, Fig. 6.3 and Fig. 6.5, respectively. Similar to the results reported for the phantom study, reconstructions obtained using the tTV regularized method exhibit less noise and discontinuities within the artery tree. Moreover, the proposed method was able to retrieve distal parts of the vessels that are invisible for the FBP-based algorithm.

We observed similar or improved image quality when the proposed respiratory motion correction strategies were applied. In agreement with the phantom study as well as the results of Chap. 5, improvements were substantial for the AFM-based correction for all studied cases, while ECC-based compensation yielded notable improvements only in presence of strong respiratory motion artifact, such as R3.

## 6.4 Discussion

Although the proposed methods for respiratory motion compensation substantially improved reconstruction performance w.r.t. the uncorrected case, the Dice scores achieved on CARDBREATH remain considerably below the upper bound given by the reconstruction of CARD. This suggests that both ECC- and AFM-based respiratory motion correction algorithms cannot yet accurately estimate and, hence, compensate for all occurring displacements. The most obvious reason is that the considered motion models may not be flexible enough [Shec 06]. Extending the proposed approaches using more complex motion models is complicated for ECC due to reasons presented in Sec. 5.4.0.3, but may be feasible for AFM. However, this would require more efficient optimization schemes to be practical, as the performance of  $\alpha$ -expansions is drastically dependent on the parameter space to be discretized. Yet, the Dice coefficients of 44.0 % and 46.3 % achieved with AFM-corrected FBP-based and tTV regularized reconstruction, respectively, are the highest scores on data set CARDBREATH in CAVAREV at the time of writing. The scoreboard is shown in Tab. 6.2.

AFM-based correction substantially outperformed the ECC-based method in the task-based evaluation targeted at reconstruction quality presented here. This suggests that the epipolar constraint-based evaluation strategy proposed in Sec. 5.2.4.1, although able to predict improvement, fails to accurately rank the methods w.r.t. to anticipated reconstruction performance. Our results indicate that the 3-D metric proposed in Sec. 5.2.4.2 more accurately reflects the results reported in this chapter. The respiratory motion compensation algorithms presented in Chap. 5 were not applied to CARD as there is no respiratory motion. Considering that applying AFMs

**Table 6.2:** Best Dice coefficients achieved in CAVAREV. Methods are listed in ascending order w.r.t. their scores achieved on CARDBREATH and, if unavailable, w.r.t. CARD. Results of previous methods are linked to the respective publication. Results obtained within the scope of this thesis are highlighted in light gray, while results taken from our own prior work are shaded in dark gray. The best performing methods on CARD and CARDBREATH, respectively, are highlighted in bold face.

	CARD	CARDBREATH
Dynamic level set reconstruction [Keil 09a]	69.2 %	–
2-D/2-D registration-based motion compensation [Schw 13a]	77.6 %	–
PICCS [Chen 12]	72.6 %	–
3-D/2-D registration-based compensation [Rohk 11]	72.8 %	–
sTV [Wu 11]	78.5 %	–
tTV + vDSA [Taub 17c]	<b>87.6 %</b>	–
ECG-gated FDK [Rohk 17]	59.5 %	15.6 %
Standard FDK [Rohk 17]	43.1 %	20.6 %
Streak-reduced, ECG-gated FDK	76.0 %	21.0 %
tTV	81.2 %	25.1 %
Streak-reduced, ECG-gated FDK + ECC	–	27.9 %
tTV + ECC	–	30.7 %
2-D/2-D registration-based compensation with large gates [Schw 13b]	82.3 %	38.6 %
Streak-reduced, ECG-gated FDK + AFM	–	44.0 %
tTV + AFM	–	<b>46.3 %</b>

improved image the quality even for very small motion amplitudes as in R1 and R2, it may be worthwhile to investigate this behavior within the CAVAREV framework. Within this study, we reconstructed CARD without the use of background suppression to better reflect the challenges faced in clinical data. It is worth mentioning, that the proposed **sTV** and **tTV** regularized iterative algorithm using **vDSA** preprocessing has recently achieved a Dice coefficient of 87.6% on CARD, making it the best performing method in CAVAREV up to date [Taub17c]. The algorithm outperformed methods based on cardiac motion compensation [Schw13a, Schw13b], suggesting that temporal regularization is a viable alternative for incorporating more data into the reconstruction problem.

Above comments apply to the results on clinical data. Additionally, we observe that some distal vascular structures are not fully recovered due to the fact that in several frames, the vessel tree is not completely recognized by the **vDSA** pipeline (Sec. 4.4), leading to inconsistent data. Mild examples of this issue can be seen in Fig. 4.1, where parts of single, small vessels are still visible in the inpainted background images. Overall, the employed regularization scheme appears to be robust when dealing with such inconsistencies. The benefits of spatially and temporally regularized iterative reconstruction over streak-reduced, gated **FDK** become apparent when comparing top and bottom rows in Fig. 6.2, Fig. 6.3, Fig. 6.3 and Fig. 6.5. Using any motion correction scheme, **FDK** suffers from an increased amount of noise and artifacts and partially fails to resolve structures that are clearly distinguishable when the proposed method is employed.

Our results on clinical data, despite qualitative, suggest a clear ranking of both respiratory motion correction and tomographic reconstruction algorithms that is supported by the quantitative results on phantom data. Nevertheless, assessing the reconstruction performance quantitatively on *in vivo* patient data, potentially using the norm of the residual error  $\|\mathbf{M}\mathbf{f} - \mathcal{D}\|_1$ , remains subject of future work.

Despite the promising results, the methods developed here rely on periodic cardiac motion as they employ gating strategies. This assumption, however, is not justified in many cases due to irregularities in the heart beat pattern [Cies84, Wang99, Chun04] suggesting that cardiac motion compensation as proposed in [Blon06, Hans08b, Rohk10b, Schw13a] may be imperative to obtain diagnostic image quality comparable to computed tomography angiography (CTA) [Blue08].

## 6.5 Conclusion

We presented a novel approach to dynamic tomographic reconstruction of the coronary arteries from rotational angiography that minimizes residual motion within each gate while, at the same time, exploiting all available data by means of spatio-temporal regularization. Combined with respiratory motion compensation strategies and **vDSA** preprocessing, the proposed method outperforms both algebraic and analytic state-of-the-art techniques on *in silico* data, leading the scoreboard of CAVAREV on both the CARD and CARDBREATH data set at the time of writing.

Future work will consider the integration of cardiac motion compensation algorithms into the **tTV** framework to bring tomographic lumen reconstruction from rotational angiography yet another step closer to achieving diagnostic image quality.



# Symbolic Coronary Artery Reconstruction

7.1	Introduction .....	65
7.2	Methods .....	66
7.3	Results .....	75
7.4	Discussion .....	77
7.5	Conclusion .....	81

## 7.1 Introduction

Symbolic algorithms enable 3-D reconstruction of the vascular tree from very few projections [Cime 16a]. This asset, however, comes at the price of requiring reliable vessel centerlines in projection domain (cf. Sec. 3.5.2), that are not easily obtained in practice. Centerline extraction is particularly difficult in rotational angiography due to overlap with high intensity structures, such as catheters, metallic implants, or bones, and varying vessel contrast. Inconsistent quality of the extracted centerlines, however, poses a severe problem for virtually any symbolic reconstruction algorithm. Moreover, algorithms based on the epipolar geometry [Blon 06] or multi-view stereo [Liao 10] require the selection of reference views, making the methods inherently asymmetric. Consequently, the performance is heavily dependent on the segmentation quality in and viewing directions of the selected reference frames that, ideally, should exhibit minimal foreshortening: On the one hand, excess centerlines propagate through the reconstruction pipeline yielding inconsistent 3D points. On the other hand, foreshortened vessel segments and incomplete centerlines give rise to gaps in the reconstructed arterial tree [Unbe 16a]. Considering these challenges, estimating the coronary artery topology using minimum spanning trees as proposed in the literature [Liao 10, Cime 16b] is unlikely to recover the desired geodesics.

In this chapter, we propose methods that address aforementioned challenges in three post-processing steps: Symmetrization of the centerline modeling thus eliminating reference frame selection, consistency-based removal of outliers, and vascular tree extraction in 3-D that considers the 2-D centerlines to avoid shortcuts.

We show that the devised methods are generic and, hence, applicable to any symbolic reconstruction algorithm using few views. This is done by extending two coronary artery reconstruction algorithms, namely the methods introduced by Blondel et al. [Blon 06] and Liao et al. [Liao 10]. Then, we evaluate the original and extended algo-

rithms by quantitative assessment of reconstruction quality on the two phantom and the three clinical data sets.

## 7.2 Methods

### 7.2.1 Gating and Projection Domain Centerline Extraction

We apply nearest neighbor gating according to Sec. 6.2.1 w.r.t. a cardiac phase at end diastole to obtain the set  $\mathcal{C} = \{i_1, i_2, \dots\}$  of  $N_c$  quasi-stationary images  $\mathcal{I}^i$  and the respective projection matrices, where  $i \in \mathcal{C}$ . Following the procedure detailed in Sec. 4.4.1, projection domain centerlines  $\mathcal{T}^i$  are extracted automatically and the respective distance transforms  $\Lambda^i(\mathbf{u}|\mathcal{T}^i)$  are computed.

### 7.2.2 Asymmetric Reconstruction and Challenges

From the projection domain segmentations, we reconstruct sets of 3-D points using state-of-the-art methods based on explicit [Blon 06] and implicit [Liao 10] correspondence matching as described earlier in Sec. 3.5.2.1 and Sec. 3.5.2.2, respectively. Aforementioned algorithms are similar in that they require the selection of a set of reference frames. In the case of epipolar geometry-based reconstruction a set of two views  $r = \{i_1, i_2\}, i_{1,2} \in \mathcal{C}$  is selected whereas for graph cut-based reconstruction selection of a single reference view  $r$  is sufficient. Although both methods are relatively robust against segmentation errors in views other than the reference, the reconstruction result heavily depends on the quality of the centerlines that are extracted from the reference views  $\mathcal{I}^r$ . The reason is that only points in  $\mathcal{T}^r$  will be reconstructed making the algorithm susceptible to incomplete centerlines and suggesting best performance for views with minimal foreshortening. However, every single centerline point in the reference views will be reconstructed implying that  $\mathcal{T}^r$  should not contain excess segmentations. A common way of addressing these issues is adding user interaction for segmentation refinement and view selection to otherwise fully automatic algorithms [Liao 10]. Doing so, however, seems impractical in a clinical application.

To overcome aforementioned limitations, we propose extensions to asymmetric centerline reconstruction that consist of exhaustive merging (Sec. 7.2.3), consistency-based outlier removal (Sec. 7.2.4), and projection domain-informed topology recovery (Sec. 7.2.5).

### 7.2.3 Symmetrization

We seek to omit reference frame selection and to promote completeness of the set of reconstructed points  $\mathcal{R}$ . This is achieved by considering all sets of reconstructed 3-D points  $\mathcal{R}^r$  that arise from reconstruction with respect to reference views  $\mathcal{I}^r$  with  $r \in \mathcal{C}$ . The point clouds describe the same 3-D scene but do not necessarily contain the exact same 3-D points. Straight-forward merging of all sets could, therefore, lead to dissimilar point densities. The strategy proposed here is inspired by the fusion algorithm described in [Blon 06] with the slight difference that we do not fuse two



sets at a given time but all sets simultaneously. For each point  $\hat{\mathbf{u}}^{r_1}$  we retrieve points from the remaining sets that are considered redundant  $\hat{\mathbf{u}}^{r_2} = d(\hat{\mathbf{u}}^{r_1} | \mathcal{R}^{r_2})$  satisfying  $d(\hat{\mathbf{u}}^{r_1} \hat{\mathbf{u}}^{r_2}) < t_{3D}$  with  $r_2 \in \{1, \dots, N_r\} \setminus \{r_1\}$ , where  $d(\hat{\mathbf{u}} | \mathcal{R})$  retrieves the closest point to  $\hat{\mathbf{u}}$  in  $\mathcal{R}$ ,  $t_{3D}$  is a constant and  $N_r$  is the number of asymmetric reconstructions, i.e.,  $N_r = N_c \cdot (N_c - 1)$  and  $N_r = N_c$  for the explicit and the implicit method, respectively. The barycenter of these points is added to the symmetric reconstruction  $\mathcal{R}$  and the individual points are removed from their respective sets  $\mathcal{R}^{r_h}$ . The procedure starts with  $h = 1$  and is repeated until  $\mathcal{R}^{r_h} = \emptyset \forall h \in \{1, \dots, N_r\}$ .

### 7.2.4 Outlier Removal

Symmetrization of the reconstruction using exhaustive merging effectively closes gaps in the 3-D arterial tree that arise from incomplete segmentations or foreshortened segments. However, the set of reconstructed 3-D points  $\mathcal{R}$  still contains incorrect points that originate from excess centerlines. Erroneous segmentations usually occur at structures that resemble contrasted vessels in projection images, such as the cortical bone of ribs or vertebrae. However, erroneous segmentations of such structures only propagate through the preprocessing pipeline described in Sec. 4.4.1 if they are considered connected to the arterial tree, e.g., in presence of overlap due to projective simplification. Fortunately, such scenarios only occur in a limited angular range in P-A viewing direction. Although points reconstructed from excess centerlines do minimize the respective reconstruction cost functions, their reprojection error into views other than the reference reveals high discrepancies as erroneous segmentations are highly likely to be inconsistent among views. This property can be exploited effectively to remove outliers from  $\mathcal{R}$  that are not consistent with a majority of the observations  $\mathcal{T}^i$  with  $i \in \mathcal{C}$ . A score is assigned to each 3-D point  $\hat{\mathbf{u}} \in \mathcal{R}$  that is derived from the reprojection error

$$s_{\hat{\mathbf{u}}} = \mathbb{P}_k \left( \left\{ \lambda^i(\hat{\mathbf{u}}) \mid i \in \mathcal{C} \right\}, k \right), \quad (7.1)$$

where  $\lambda^i(\hat{\mathbf{u}}) = \Lambda^i(\check{\mathbf{u}}^i | \mathcal{T}^i)$  is the distance of the reprojected point to the closest centerline point in view  $i$  and  $\mathbb{P}_k(\{\lambda^i(\hat{\mathbf{u}}), i \in \mathcal{C}\}, k)$  yields the  $\lambda^j$  such that  $k \cdot 100\%$  of all observations  $\lambda^i$  are smaller than or equal to  $\lambda^j$ . Points with scores  $s_{\hat{\mathbf{u}}}$  above a certain threshold  $t_{2D}$  are considered outliers and removed from the reconstruction. The magnitude of  $t_{2D}$  is matched to the expected residual motion and is set to 0.75 mm and 1.5 mm for phantom and clinical data sets, respectively. Choosing  $k \leq (N_c - 1)/N_c$  promotes robustness against incomplete centerlines that arise from statistical segmentation errors or contrast wash-out. In our experiments, we set  $k = (N_c - 1)/N_c$  due to the very low amount of views available in rotational angiography.

### 7.2.5 Vascular Tree Extraction

After symmetrization and outlier removal we are left with a set of 3-D points  $\mathcal{R}$  that reflects the underlying anatomy but is not yet connected such that the topology of the arterial tree remains unclear. Liao et al. use a Euclidean [minimum spanning tree \(MST\)](#) to recover the topology [Liao 10]. Rather than requiring a minimal Euclidean length of the arterial tree, we propose an edge cost that reflects prior knowledge about

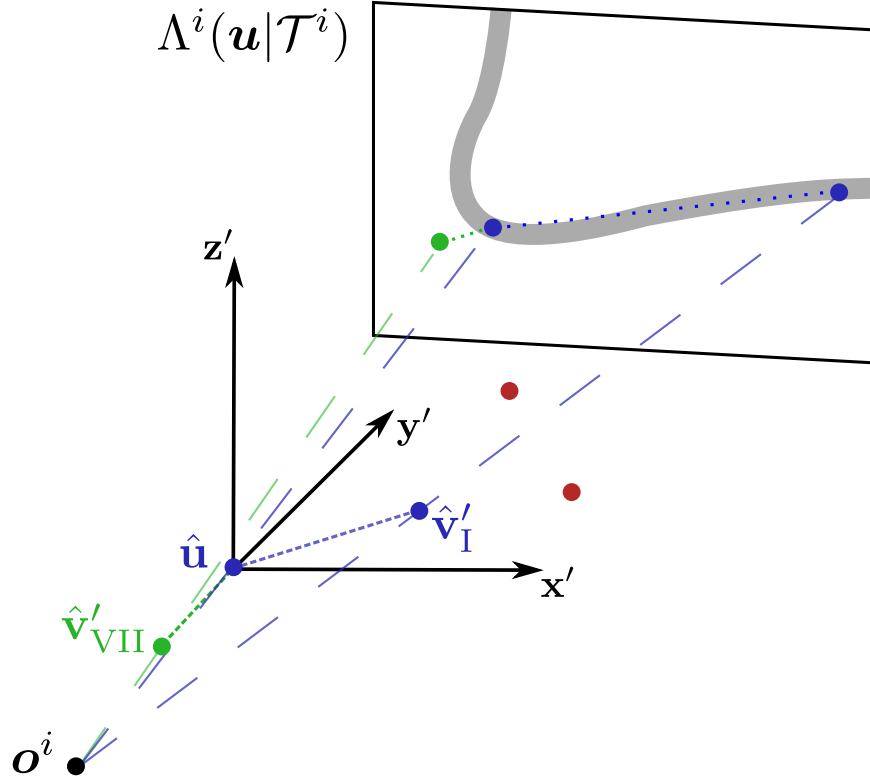


**Figure 7.1:** Edge cost computation in 3-D using reprojection in view  $i$ . The points  $\hat{v}'_I$  and  $\hat{v}'_{VII}$  are the closest points to  $\hat{u}$  in octants I and VII, respectively. The red dots denote points that are also located in octant I but are not considered. Although close to the centerline, the reprojection of edge  $e_{\hat{u}, \hat{v}'_{VII}}$  into view  $i$  does not yield a large contribution to the overall edge cost as defined in Eq. (7.2), as it is foreshortened and assigned a weight  $\eta^i$  close to zero.

the centerlines in projection domain.

To this end, we first divide the set of reconstructed points into connected sets  $\mathcal{R} = \bigcup \mathcal{V}_i$  such that  $\mathcal{V}_i = \{\hat{u} \in \mathcal{R} \mid \|\hat{u} - d(\hat{u} | \mathcal{R} \setminus \mathcal{V}_i)\|_2 > t_{\text{con}}\}$ . In practice, this division is achieved using a Kruskal Euclidean MST [Krus 56]. The maximum allowed distance between points  $t_{\text{con}}$  prevents bridging of large gaps resulting from, e.g., consistently incomplete segmentations due to low contrast, and was set to 6 mm. We now seek to recover the topology of each individual subset  $\mathcal{V}_i$ .

Extracting vascular trees from a 3-D point cloud that exhibit a minimal Euclidean distance is, in general, not optimal because of shortcuts. Short-cutting may occur when points of topologically distinct anatomical structures are geometrically close, e.g., at bifurcations. We propose projection domain-informed shortest path extraction to address this issue. Rather than relying on Euclidean distances as edge costs, we devise an edge cost computed in projection domain and only implicitly account for spatial closeness in 3-D. The cost is derived from the 2-D centerlines that were used to obtain the set of reconstructed points in the first place. Given two 3-D points  $\hat{u}, \hat{v} \in \mathcal{V}_i$  the isotropic cost of the connecting edge  $e_{\hat{u}, \hat{v}}$  is given as

$$\epsilon(e_{\hat{u}, \hat{v}}) = \frac{\|e_{\hat{u}, \hat{v}}\|_2}{\sum_k \eta^k(e_{\hat{u}, \hat{v}})} \sum_{j \in C} \eta^j(e_{\hat{u}, \hat{v}}) \cdot \psi(e_{\hat{u}, \hat{v}}, j), \quad (7.2)$$

where

$$\eta^j(\mathbf{e}_{\hat{\mathbf{u}}, \hat{\mathbf{v}}}) = 1 - \frac{|\mathbf{e}_{\hat{\mathbf{u}}, \hat{\mathbf{v}}}^\top \cdot \mathbf{r}_{\mathbf{u}_0}^j|}{\|\mathbf{e}_{\hat{\mathbf{u}}, \hat{\mathbf{v}}}\|_2 \cdot \|\mathbf{r}_{\mathbf{u}_0}^j\|_2} \quad (7.3)$$

is a weighting based on the foreshortening of a particular edge in the target view  $j$  with principal ray  $\mathbf{r}_{\mathbf{u}_0}^j$ . The projection domain cost reads

$$\psi(\mathbf{e}_{\hat{\mathbf{u}}, \hat{\mathbf{v}}}, j) = \sum_{l=0}^{L-1} \Lambda^j \left( \check{\mathbf{u}}^j + \frac{l}{L-1} (\check{\mathbf{v}}^j - \check{\mathbf{u}}^j) \mid \mathcal{T}^j \right), \quad (7.4)$$

with  $L$  being the number of discrete samples along a certain edge.  $L$  is determined using a constant sampling factor, such that  $L = \|\check{\mathbf{v}} - \check{\mathbf{u}}\|_2/s$ , where  $s$  is set to one fifth of the pixel size.

Spatial closeness in 3-D is addressed implicitly, as for a particular point  $\hat{\mathbf{u}}$  we only establish connections  $\mathbf{e}_{\hat{\mathbf{u}}, \hat{\mathbf{v}}'_o}$  to the closest point  $\hat{\mathbf{v}}'_o$  in each of the eight octants  $o$  of a translated coordinate system centered in  $\hat{\mathbf{u}}$ . The process is illustrated schematically in Fig. 7.1.

Once the connecting edges and the respective costs are known, we can construct a graph and extract a **MST** that is minimal with respect to the cost stated in Eq. (7.2). Finally, we seek to extract distinct vessel branches from the **MST** edges using Dijkstra's algorithm. To this end, the start node is determined as the point with the most connections to neighboring nodes. Subsequently, we extract vessel branches as the set of edges that connects a particular leaf node to the start node. To avoid fragmentation of long branches, branch extraction is carried out iteratively. In each iteration, only the leaf node yielding the longest branch is considered. The procedure is repeated until all edges of the **MST** are used, yielding a minimal set of maximal paths  $\hat{\mathcal{T}} = \bigcup \hat{\mathcal{B}}_i$  that still contains unwanted branches.

### 7.2.6 Pruning

The resulting vessel centerline tree  $\hat{\mathcal{T}}$  still contains short and incorrect branches that should be removed. After pruning of very short paths, we compute significance values for the remaining branches. For a particular vessel branch  $\hat{\mathcal{B}}_i$ , the significance  $\chi_i$  is determined by its total length  $\mathcal{L}_i$  and a weighting derived from projection domain similar to Eq. (7.4). It reads

$$\chi_i = \left( \text{mean}_j \left( \epsilon^j(\hat{\mathcal{B}}_i), \eta_{\hat{\mathcal{B}}_i}^j \right) \cdot \left( 1 + \sqrt{\text{var}_j \left( \epsilon^j(\hat{\mathcal{B}}_i), \eta_{\hat{\mathcal{B}}_i}^j \right)} \right) \cdot \frac{1}{\mathcal{L}_i} \right)^{-1} \quad (7.5)$$

where  $\epsilon^j(\hat{\mathcal{B}}) = \sum_{\mathbf{e} \in \hat{\mathcal{B}}} \eta^j(\mathbf{e}) \cdot \psi(\mathbf{e}, j)$  is the projection domain branch cost in view  $j$  and  $\eta_{\hat{\mathcal{B}}}^j = \sum_{\mathbf{e} \in \hat{\mathcal{B}}} \eta^j(\mathbf{e})$  are the view dependent weights that reflect the total foreshortening of branch  $\hat{\mathcal{B}}$  in the respective view. Moreover,  $\text{mean}_j(\epsilon^j, \eta^j)$  and  $\text{var}_j(\epsilon^j, \eta^j)$  compute the weighted mean and variance of measurements  $\epsilon^j$  with corresponding weights  $\eta^j$ . The significance value  $\chi$  is highest for long centerline branches that consistently project close to the 2-D centerlines. Consequently, it can be used to rank the extracted centerlines and, once ordered, remove incorrect branches from the final tree.

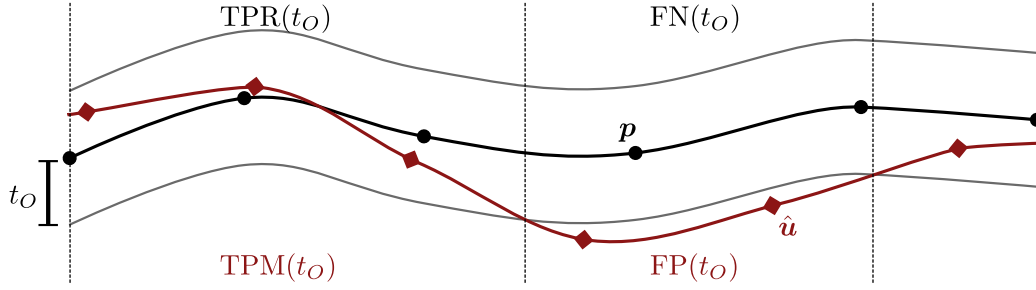


**Figure 7.2:** Schematic illustrating the definitions of false positives, false negatives, and true positives for a particular distance threshold  $t_O$ .

## 7.2.7 Experiments

### 7.2.7.1 Evaluation Metrics

**3-D Overlap** We use the 3-D ground truth centerlines  $\mathcal{G}_c^i$  and  $\mathcal{G}_b^i$  at motion state  $i$  provided by CAVAREV to evaluate the proposed methods in reconstruction domain. The metric used for the evaluation of a particular reconstruction  $\mathcal{P}_{\hat{T}}$  is a modified form of the overlap measure introduced in [Scha 09] and, later, used to assess centerline reconstructions in [Cime 16b]. For a particular combination of ground truth and test centerlines sampled according to Sec. 7.2.7.2,  $\mathcal{P}_{\mathcal{G}}$  and  $\mathcal{P}_{\hat{T}}$ , respectively, the procedure is as follows.

First, both ground truth and reconstructed centerlines  $\mathcal{G}$  and  $\hat{T}$  are sampled equidistantly using a sampling distance of 0.1 mm yielding sets of 3-D points  $\mathcal{P}_{\mathcal{G}}$  and  $\mathcal{P}_{\hat{T}}$ , respectively, that are used for the evaluation. To assess overlap we use a sweeping distance threshold  $t_O \in [t_{\min}, t_{\max}]$  rather than the vessel diameter. Given a distance  $t_O$ , every point of the ground truth  $p \in \mathcal{P}_{\mathcal{G}}$  is marked as belonging to the set  $TPR(t_O)$  of true positives of the reference if there is at least one point  $\hat{u} \in \mathcal{P}_{\hat{T}}$  satisfying  $\|p - \hat{u}\|_2 < t_O$  and to the set  $FN(t_O)$  of false negatives otherwise. Points of the reconstruction  $\hat{u}$  are labeled as belonging to the set  $TPM(t_O)$  of true positives of the tested method if there is at least one ground truth point  $p$  satisfying  $\|\hat{u} - p\|_2 < t_O$  and to the set  $FP(t_O)$  of false positives otherwise. The overlap for a certain distance can then be computed as

$$O(t_O) = \frac{|TPM(t_O)| + |TPR(t_O)|}{|TPM(t_O)| + |TPR(t_O)| + |FN(t_O)| + |FP(t_O)|}. \quad (7.6)$$

Similar to the Dice score (cf. Sec. 6.2.6), the overlap measure ranges from zero (no overlap) to one (perfect match). An intuitive illustration is provided in Fig. 7.2. With increasing distance thresholds the measure increases monotonically. A simple score that reflects the overall quality of a reconstruction is the area under the overlap curve

$$\tilde{O} = \frac{1}{t_{\max} - t_{\min}} \int_{t_{\min}}^{t_{\max}} O(t) dt \quad (7.7)$$

that, again, ranges from zero to one indicating no to perfect overlap, respectively. In our experiments we chose  $(t_{\min}, t_{\max}) = (0 \text{ mm}, 2.5 \text{ mm})$ . The computation is repeated for every ground truth motion state and the maximum value is chosen as the final score.

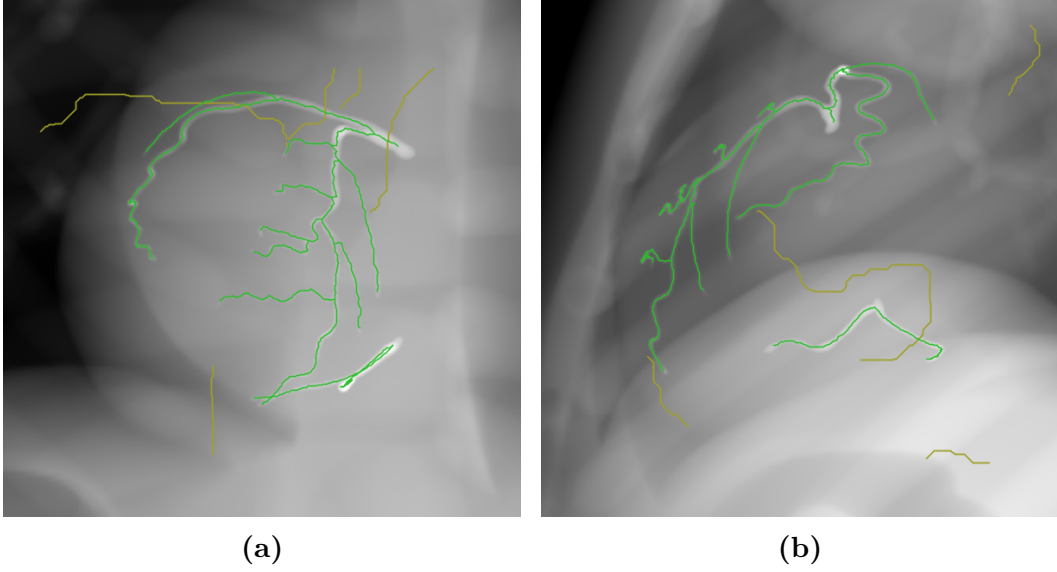


**Figure 7.3:** Two exemplary views of the phantom: ground truth centerlines are highlighted in green while randomly generated outliers (40 % corruption) are depicted in yellow.

**Reprojection Error** As the 3-D ground truth is not available for clinical data, the overlap as defined above cannot be computed. To provide a measure that applies to both phantom and clinical data, we assess the averaged mean reprojection error referred to as  $\text{RE}^{\text{mean}}$ . This metric is derived from a set of reconstructed 3-D points  $\mathcal{P}_{\hat{\mathcal{T}}}$  and the 2-D ground truth centerlines that, in case of the phantom study, are obtained by forward projection of the 3-D ground truth. The reprojection error is computed as

$$\text{RE}^{\text{mean}} = \frac{1}{|\mathcal{P}_{\hat{\mathcal{S}}}|} \sum_{\hat{\mathbf{u}} \in \mathcal{P}_{\hat{\mathcal{T}}}} \text{mean}_i \left( \|\hat{\mathbf{u}}^i - \mathbf{p}^i\|_2 \right) \quad (7.8)$$

where  $\mathbf{p}^i$  is the 2-D centerline point closest to  $\hat{\mathbf{u}}^i$  in view  $i$ .

### 7.2.7.2 Procedure

We reconstruct 3-D centerlines using the symbolic algorithms described in Sec. 3.5.2.1 and Sec. 3.5.2.2 with and without the proposed extensions for all data sets introduced in Chap. 4. Standard and extended algorithms based on the explicit correspondence matching using the epipolar geometry will be referred to as EG and  $\text{EG}_{\text{ext}}$  while the implicit methods based on graph cuts are denoted by GC and  $\text{GC}_{\text{ext}}$ , respectively.

**Data Set Card** To investigate the performance of the proposed extensions in a very controlled environment, we corrupt the ground truth of CARD in every view by adding excess structure amounting to 0 %, 10 %, 20 %, 30 %, and 40 % of the true centerline pixels. Excess structure is generated by simulating paths of particles subject to Brownian motion similar to [Cime 16b], examples of which are shown in Fig. 7.3.

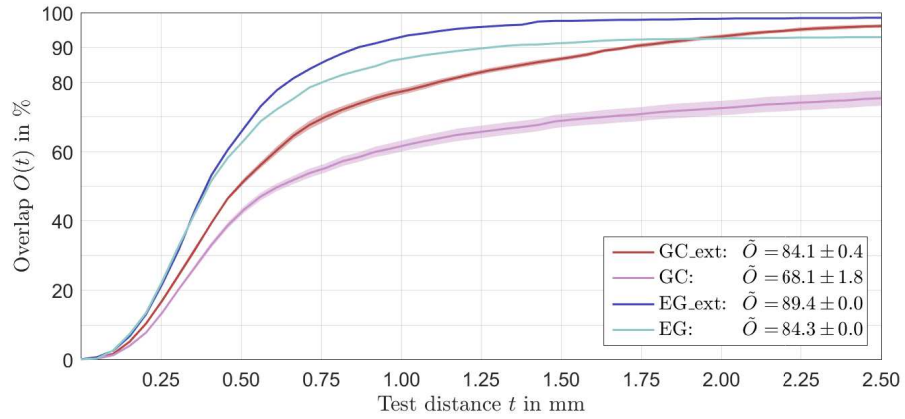
As the outlier generation is random, the corruption process is repeated ten times. For each generated data set, we reconstruct coronary artery centerlines using the two algorithms introduced earlier with and without the proposed extension and assess the overlap with the ground truth in 3-D and reprojection errors in 2-D. Finally, we report the average area under the overlap curve  $\tilde{O}$ , and the averaged mean reprojection error  $RE^{\text{mean}}$ .

**Data Set CardBreath** Similar to Chap. 6, we use the uncompensated, and respiratory motion corrected imaging geometries to reconstruct the 3-D anatomy using both original and extended methods. As for data set CARD, we report the area under the overlap curve  $\tilde{O}$  and the reprojection error.

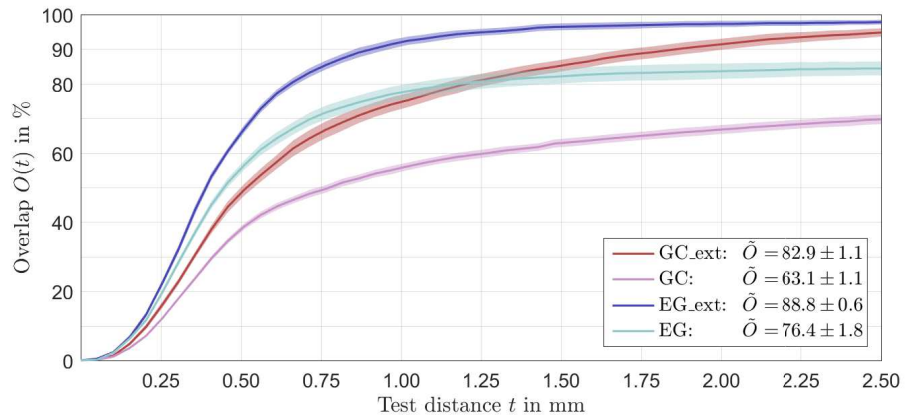
**Clinical Data** We demonstrate the applicability of the proposed extensions to the reconstruction of clinical data. Considering the findings of Chap. 5 and Chap. 6, we limit the analysis on clinical data to reconstructions using the AFM-corrected projection matrices.

As the 3-D ground truth is unknown, we manually segment coronary artery centerlines in the projection images. Overlap assessment in projection domain does not yield the desired result because points that are far from the correct 3-D position may project close to 2-D centerlines and, therefore, bias the assessment. Consequently, we limit the quantitative analysis to the mean reprojection error using the manually extracted 2-D ground truth as the reference.

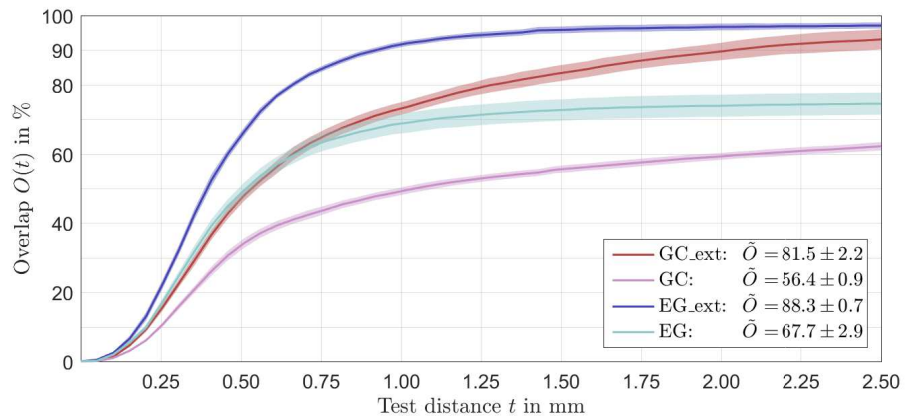
We reconstruct 3-D centerlines using the manually obtained 2-D ground truth to establish an upper bound on the reconstruction quality to be expected that will be referred to as  $RE_{GT}^{\text{mean}}$ . In a second experiment, we rely on the automatically extracted projection domain centerlines and use those for 3-D reconstruction. Finally, we assess the quality of the automatic result by computing the reprojection error according to Eq. (7.8).



(a) Baseline: 0 % corruption



(b) Mild: 20 % corruption



(c) Severe: 40 % corruption

**Figure 7.4:** Overlap curves describing average reconstruction results obtained using centerline reconstruction algorithms based on epipolar geometry (EG, explicit) and graph cuts (GC, implicit). The solid curves represent the mean overlap with the transparent margin representing the standard deviation. Fig. 7.4a establishes a baseline for the reconstruction performance to be expected. Fig. 7.4b and Fig. 7.4c show reconstruction performance for different levels of additive outliers.

**Table 7.1:** Quantitative results of the phantom study on data set CARD: Average area under the overlap curve for different corruption levels stated in %.

	$\tilde{O}_{0\%}$	$\tilde{O}_{10\%}$	$\tilde{O}_{20\%}$	$\tilde{O}_{30\%}$	$\tilde{O}_{40\%}$
EG	$84.3 \pm 0.0$	$80.3 \pm 1.5$	$76.4 \pm 1.8$	$72.5 \pm 3.3$	$67.7 \pm 2.9$
EG <sub>ext</sub>	$89.4 \pm 0.0$	$89.1 \pm 0.5$	$88.8 \pm 0.5$	$89.1 \pm 0.5$	$88.3 \pm 0.7$
GC	$65.4 \pm 6.3$	$62.7 \pm 6.4$	$60.4 \pm 6.2$	$58.7 \pm 5.1$	$55.9 \pm 5.1$
GC <sub>ext</sub>	$84.1 \pm 0.4$	$83.1 \pm 0.9$	$82.9 \pm 1.1$	$82.5 \pm 2.4$	$81.5 \pm 2.2$

**Table 7.2:** Mean reprojection error for different corruption levels of the phantom study CARD stated in mm.

	RE <sub>0%</sub> <sup>mean</sup>	RE <sub>10%</sub> <sup>mean</sup>	RE <sub>20%</sub> <sup>mean</sup>	RE <sub>30%</sub> <sup>mean</sup>	RE <sub>40%</sub> <sup>mean</sup>
EG	$4.86 \pm 14.13$	$4.69 \pm 12.19$	$6.97 \pm 15.86$	$8.82 \pm 17.5$	$8.78 \pm 18.01$
EG <sub>ext</sub>	$0.160 \pm 0.081$	$0.169 \pm 0.117$	$0.181 \pm 0.173$	$0.170 \pm 0.125$	$0.198 \pm 0.223$
GC	$0.506 \pm 0.880$	$1.27 \pm 3.83$	$1.83 \pm 4.66$	$2.55 \pm 5.71$	$2.96 \pm 6.34$
GC <sub>ext</sub>	$0.193 \pm 0.128$	$0.201 \pm 0.0137$	$0.202 \pm 0.136$	$0.204 \pm 0.142$	$0.215 \pm 0.167$



## 7.3 Results

**Data Set Card** Quantitative results of overlap assessment in the phantom study are reported in Tab. 7.1 and visualized in Fig. 7.4. Mean reprojection errors are summarized in Tab. 7.2.

The results suggest that EG-based centerline reconstruction yields superior overall reconstruction quality both for its original and extended version. For the extended algorithms, we observe improved reconstruction quality at all corruption levels. The average improvement of the overlap measure for EG-based reconstruction is  $(17.3 \pm 9.6) \%$ , whereas for the GC-based method improvement is even more substantial  $((36.9 \pm 6.7) \%)$ . As expected, reconstruction quality achieved with the original methods decreases with increasing levels of corruption. In contrast, the extended versions prove largely unaffected by the addition of outliers yielding reprojection errors below the pixel size for all corruption levels.

These observations are in agreement with the qualitative results presented in Fig. 7.5, where we show reprojections of the reconstruction results onto two representative 2-D image planes. For the original methods, reprojection shows both erroneously reconstructed points that project far from the ground truth centerlines as well as missing segments. This behavior is already observed for reconstruction of the baseline data set that does not include any outliers, and is drastically more pronounced when erroneous centerlines are introduced. When a Euclidean MST is used, we observe short cuts in the 3-D centerline that occur primarily near bifurcations and at adjacent vessels that are very close (indicated by red arrows in Fig. 7.5). In contrast, results of the extended versions no longer exhibit outliers that project far from 2-D centerlines. Moreover, projection domain informed MST extraction as explained in Sec. 7.2.5 more accurately restores correct vessel topology in complicated point distributions occurring at, e.g., bifurcations (indicated by green arrows in Fig. 7.5).

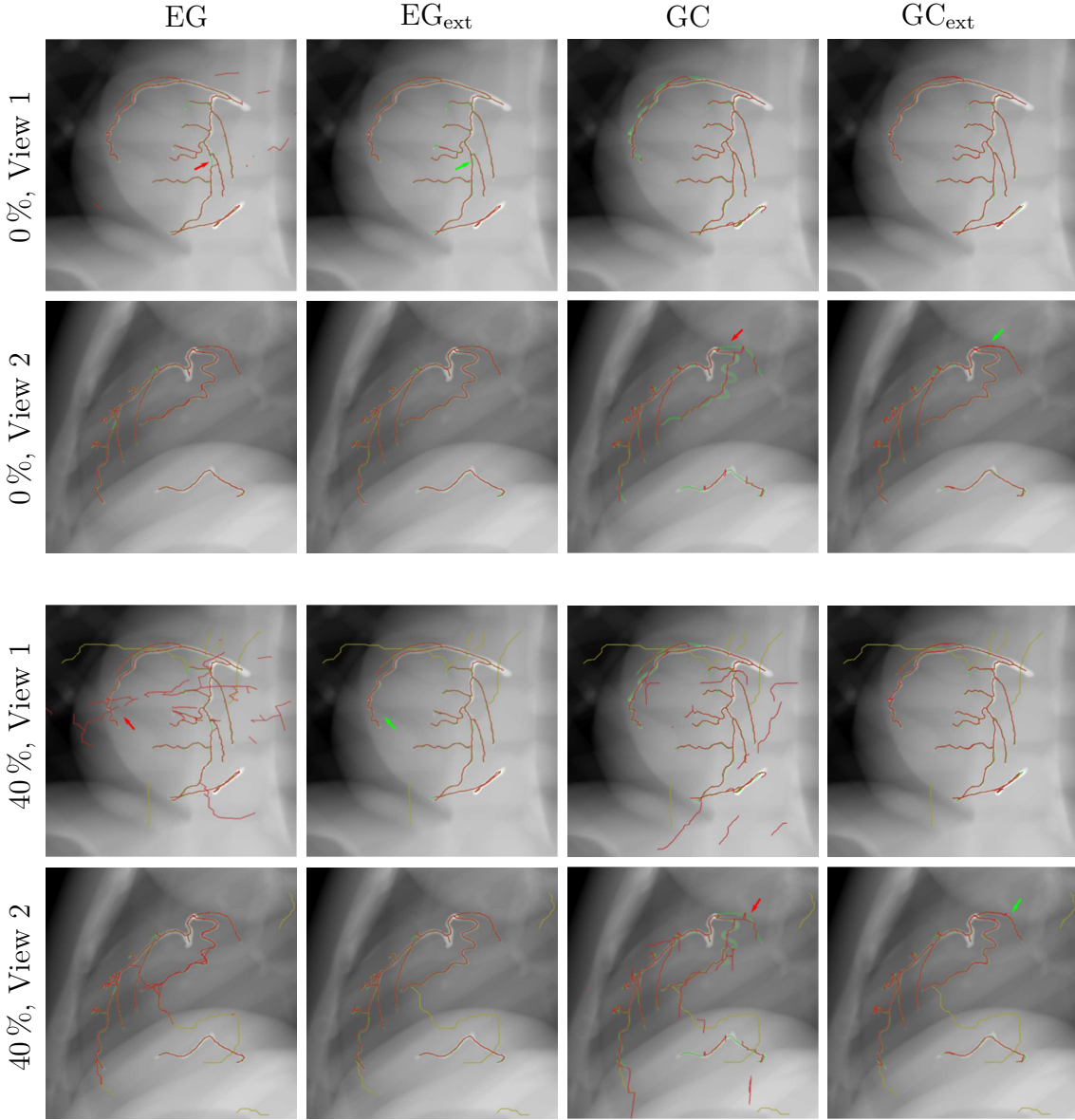


**Figure 7.5:** Reprojections of reconstruction results obtained with the four considered methods at the minimum and maximum corruption level. Erroneous, reprojected, and ground truth centerlines are overlaid in yellow, red, and green, respectively. Red arrows point to locations that exhibit outliers or short-cutting when Euclidean [MSTs](#) are used. Green arrows indicate positions where aforementioned problems are alleviated by using the proposed methods.

**Data Set CardBreath** Results of the 3-D overlap assessment and the reprojection error of reconstructions of CARDBREATH using respiratory motion compensated projection matrices are summarized in Tab. 7.3 and Tab. 7.4, respectively. Both measures indicate that respiratory motion compensation based on ECC and AFM yields superior reconstruction quality. We confirm the results of Chap. 6, where we observed best performance for AFM-based compensation.

Albeit considerable improvements for the corrected w.r.t. the uncompensated case are observed, the 3-D overlap for AFM-compensated CARDBREATH is considerably lower than for CARD.

**Clinical Data** Quantitative results of the reprojection error assessment on the clinical data is presented in Tab. 7.5. The reprojection error substantially decreased in every case when the proposed extensions were applied yielding an average improvement of  $(2.69 \pm 2.39)$  mm and  $(1.93 \pm 2.23)$  mm for EG- and GC-based methods, respectively. For reconstructions from the manually extracted centerlines all results are in agreement with the observations made in the phantom study, as they show superior accuracy for EG-based reconstruction. However, when automatically extracted centerlines are used, the GC-based method exhibits very similar up to superior performance, an observation that is discussed in greater detail below.

We found a considerable increase in reprojection error when automatically rather than manually extracted centerlines were input to the algorithms. From the reprojections shown in Fig. 7.6 it becomes apparent that the decrease in  $RE^{\text{mean}}$  is not associated with a substantial decrease in completeness. Yet, some smaller branches could not be recovered. As for the phantom data set we observe a large number of erroneously reconstructed segments for the original methods, that are largely suppressed when the proposed extensions are employed.

## 7.4 Discussion

### 7.4.1 Phantom Study

While the original EG-based algorithm already includes symmetrization, GC-based reconstruction in its original form is inherently asymmetric. Consequently, improvements in reconstruction performance were more substantial for the GC-based methods

**Table 7.3:** Quantitative results of the phantom study on data set CARDBREATH: Average area under the overlap curve for reconstructions using the uncompensated, and ECC- and AFM-corrected projection matrices, respectively. All measures are stated in %.

	$\tilde{O}_{\text{uncomp.}}$	$\tilde{O}_{\text{ECC}}$	$\tilde{O}_{\text{AFM}}$
EG	16.3	36.7	34.1
EG <sub>ext</sub>	9.1	25.7	37.8
GC	$12.1 \pm 1.1$	$15.2 \pm 5.6$	$46.8 \pm 4.8$
GC <sub>ext</sub>	8.1	19.3	51.2

**Table 7.4:** Mean reprojection error for reconstructions obtained using different respiratory motion compensation strategies on data set CARDBREATH stated in mm.

	$RE_{uncomp.}^{mean}$	$RE_{ECC}^{mean}$	$RE_{AFM}^{mean}$
EG	$3.01 \pm 4.46$	$3.41 \pm 10.8$	$2.45 \pm 5.67$
$EG_{ext}$	$1.43 \pm 0.81$	$0.686 \pm 0.503$	$0.590 \pm 0.410$
GC	$2.97 \pm 0.99$	$0.785 \pm 0.104$	$0.581 \pm 0.134$
$GC_{ext}$	$1.19 \pm 0.70$	$0.642 \pm 0.288$	$0.479 \pm 0.247$

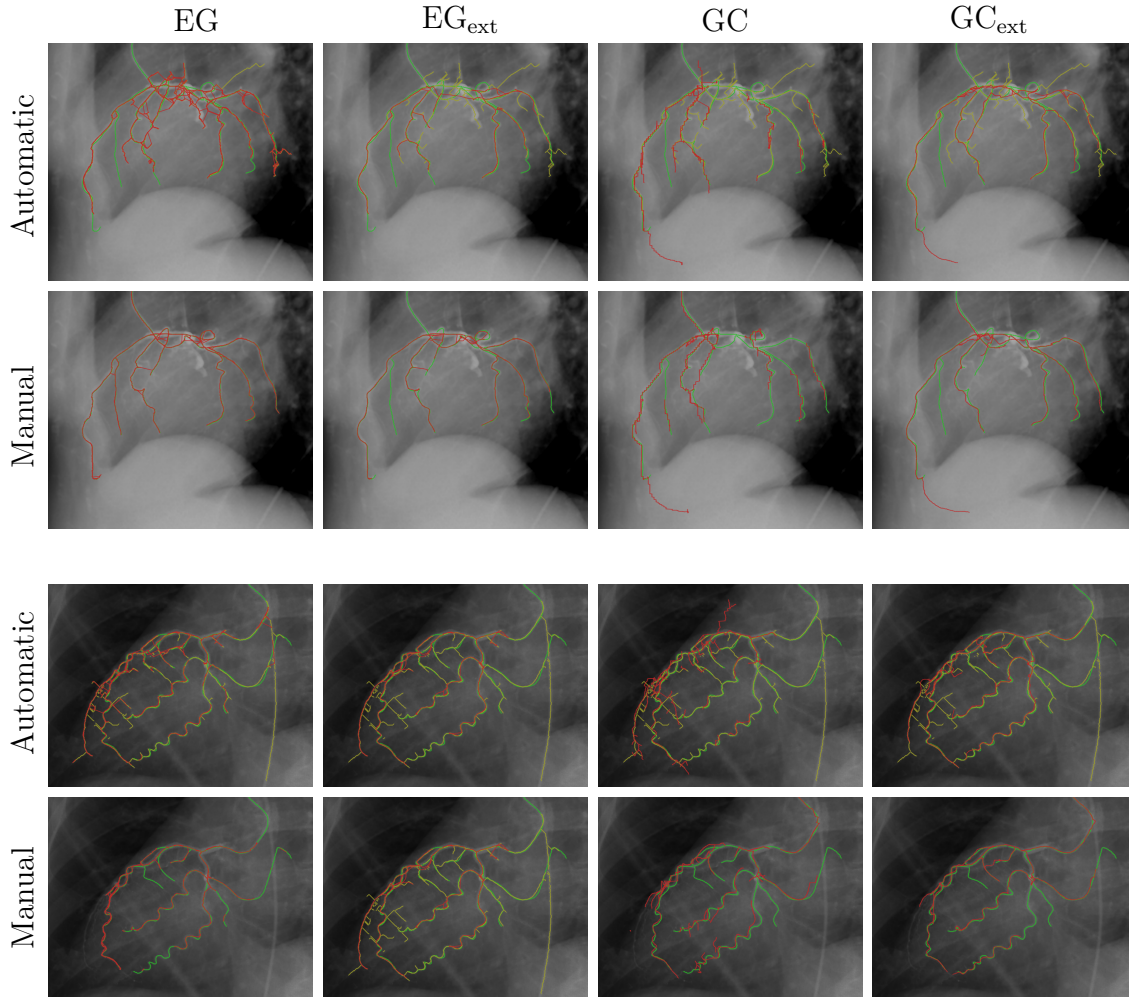


**Figure 7.6:** Representative reprojections of reconstruction results obtained with the four considered methods on clinical data. Automatically and manually extracted, and reprojected centerlines are overlaid in yellow, green, and red, respectively.

**Table 7.5:** Mean reprojection error for reconstructions of the three clinical cases obtained using [AFM](#)-corrected projection matrices from both the manually and the automatically extracted centerlines. As before, the reprojection errors are stated in mm.

<b>Autom.</b>	$RE_{R1}^{\text{mean}}$	$RE_{R2}^{\text{mean}}$	$RE_{R3}^{\text{mean}}$
EG	$3.49 \pm 5.33$	$3.87 \pm 8.09$	$10.7 \pm 15.9$
EG <sub>ext</sub>	$0.956 \pm 0.549$	$1.45 \pm 1.24$	$3.45 \pm 9.51$
GC	$5.03 \pm 3.81$	$2.75 \pm 0.76$	$6.82 \pm 3.56$
GC <sub>ext</sub>	$1.02 \pm 0.85$	$1.26 \pm 1.11$	$1.47 \pm 1.19$
<b>GT</b>	$RE_{R1}^{\text{mean}}$	$RE_{R2}^{\text{mean}}$	$RE_{R3}^{\text{mean}}$
EG	$1.21 \pm 1.88$	$1.70 \pm 3.77$	$3.34 \pm 7.97$
EG <sub>ext</sub>	$0.695 \pm 0.332$	$0.701 \pm 0.645$	$0.901 \pm 0.627$
GC	$1.03 \pm 0.11$	$1.10 \pm 0.07$	$0.979 \pm 0.141$
GC <sub>ext</sub>	$0.855 \pm 1.110$	$0.738 \pm 0.685$	$0.810 \pm 0.536$

when overlap was assessed, as symmetrization yields a drastically more complete reconstruction. This behavior is very well observed in Fig. 7.5 where, even without corruption, the original GC-based method exhibits substantial gaps in the retrieved vascular tree.

In contrast, from Tab. 7.2 it is apparent that the improvement in reprojection error was notably more pronounced for the EG-based methods suggesting that the reconstructions obtained using the original algorithm contain a large amount of incorrectly reconstructed points that project far from the 2-D centerlines, which can be seen in the top row of Fig. 7.5.

From Tab. 7.1 and Fig. 7.4 it becomes apparent that the GC-based methods show a higher standard deviation in the respective reconstruction overlap curves and, consequently, in the area under the curves. Moreover, GC-based reconstruction has a non-zero standard deviation already for the base line data set that does not contain any variation. This behavior originates from the random initialization and the approximative nature of the  $\alpha$ -expansion optimization. The algorithm yields slightly different solutions for each execution as it converges to a minimum that is within a certain range of the global optimum [Liao 10, Boyk 01].

The area under the reconstruction overlap curve for GC<sub>ext</sub> is smaller than for EG<sub>ext</sub>, suggesting that GC<sub>ext</sub> exhibits worse reconstruction performance, that may be attributed to less complete or less accurate reconstruction. The qualitative results presented in Fig. 7.5 together with the reprojection errors stated in Tab. 7.2 suggest that the discrepancy arises from a less accurate reconstruction that can, at least partly, be explained by the approximative character of GC-based reconstruction. For each reference view, the algorithm yields a set of reconstructed points that exhibits very good reconstruction quality in parts of the tree and rather poor quality in others. Consequently, the symmetric set is slightly biased towards these poor quality points due to averaging during merging as described in Sec. 7.2.3.

However, the results on data set CARDBREATH presented in Tab. 7.3 and Tab. 7.4 suggest that implicit correspondence optimization as in the GC-based methods may

be preferable in presence of residual respiratory motion, i.e., inaccurate geometric calibration. The reason seems natural: EG-based reconstruction retrieves 3-D points from correspondences that are determined using the projection matrices of two reference frames simultaneously [Hart04]. Consequently, the position of the resulting 3-D point is more drastically affected by residual errors in calibration.

### 7.4.2 Clinical Data

In the EG-based methods shown in Fig. 7.6 the reprojection of the reconstructions obtained using the original method EG seems to explain more of the projection domain ground truth than the reprojection of  $EG_{\text{ext}}$ . One may be tempted to assume that this observation implies superior reconstruction quality. 3-D points arise from the matching of two 2-D points as outlined in Sec. 3.5.2.1 and, therefore, must reproject onto the centerline in at least two views for the original method. If, however, the matching is incorrect, they do not agree with the remaining views and will be removed from the set of reconstructed points by the proposed extensions, a reasoning that is supported by the reduction in reprojection error reported in Tab. 7.5. The same line of argumentation applies to GC, however, with the difference that the original GC-based method is not yet symmetric, making it obvious which view not to consider for analysis of completeness.

Tab. 7.5 shows a generally inferior performance for clinical scan  $R_3$ . This behavior may be attributed to residual errors in respiratory motion compensation. Both the reprojection error and its standard deviation are particularly high for the result of  $EG_{\text{ext}}$  based on the automatically extracted centerlines. Visual inspection confirmed that this behavior results from reconstruction of parts of the catheter that are not part of the manual segmentation and, consequently, negatively influence the reprojection error. It is worth mentioning, that the extended methods perform comparably well when manually extracted centerlines are used.

We have found that extended versions of EG-based reconstruction perform better than GC-based methods if correct calibration and reliable 2-D centerline information are available. However, the superior performance comes at a cost. In our experiments on clinical data, EG-based reconstruction took  $(12.0 \pm 10.2)$  min while GC-based reconstruction took  $(1.82 \pm 0.21)$  min<sup>1</sup>. Although more efficient implementations are conceivable, the execution time of EG-based reconstruction is far from interventional applicability.

### 7.4.3 Limitations and Challenges

All considered algorithms performed substantially better on phantom data compared to clinical data suggesting that the phantom study does not accurately account for all potential sources of error. Yet, it provides useful information on the baseline performance of each method, the trend of which was clearly reproduced on clinical data. The quantitative evaluation on clinical data currently uses the same views for both reconstruction and evaluation. Validation strategies that evaluate the reprojection

---

<sup>1</sup>All algorithms are implemented in Java [Maie13] and executed on a computer equipped with an Intel® Core™ i7-4910MQ processor at 2.90 GHz.

error in a leave-one-out setting are conceivable [Liao 10, Unbe 16a], but aggravate problems due to angular undersampling that negatively affecting the reconstruction performance. In situations where sufficient data is available, however, leave-one-out strategies should be preferred.

The proposed extensions use the asymmetric reconstruction results provided by slightly modified versions of previously published, state-of-the-art centerline reconstruction algorithms [Blon 06, Liao 10]. As the proposed methods are not constructive but rather restrictive, there is a fundamental limit on the achievable quality improvement that is determined by the data basis provided by a candidate reconstruction method. However, all extensions are generic such that they can easily be applied to any input centerline reconstruction algorithm.

## 7.5 Conclusion

In summary, this chapter discussed generic extensions for asymmetric coronary artery centerline reconstruction that address symmetrization, outlier removal, and projection domain-informed topology recovery. Two state-of-the-art reconstruction algorithms based on explicit, epipolar geometry-based correspondence matching and energy minimization, respectively, in their original and extended form were applied to numerical phantom and clinical data. Quantitative and qualitative evaluation demonstrated improved performance for the extended methods in all cases studied.

Although our results show that the proposed extensions can alleviate some of the problems arising from erroneous 2-D centerline segmentations, we still observed substantial performance differences when corrupted rather than clean centerlines were used for reconstruction. Consequently, future work should revisit 2-D centerline extraction that, unfortunately, is a very hard problem in rotational angiography due to varying contrast and overlap. Considering recent work by Çimen et al. [Cime 16b], it may be worthwhile to study how the presence of inevitable sources of error, such as incorrect calibration or outliers, can be modeled explicitly in reconstruction algorithms.





# Outlook

Despite promising results, we have identified areas where the proposed methods could benefit from future work.

**Auto-focus Measures (AFMs)** are an interesting concept for motion estimation from rotational acquisitions. As the focus of this thesis was registration-free respiratory motion estimation, we used a discrete optimization scheme to accommodate arbitrarily large displacements. Although elegant, the deployed scheme exhibits a high runtime making the clinical usefulness questionable. However, if smaller displacements are to be expected other optimization schemes, such as stochastic gradient descent [Zink 10], have proved highly efficient [Rohk 11], and should be considered for future investigations.

Exploiting **Epipolar consistency conditionss (ECCs)** for intra-scan motion compensation is of profound interest, as it solely relies on geometric calibration and projection domain images. Unfortunately, circular trajectories that currently constitute the clinical state-of-the-art are suboptimal for ECC-based optimization. Consequently, we would like to study ECC in combination with experimental trajectories, such as saddle trajectories [Pack 04] or **dual axis rotational angiography (DARCA)** [Klei 11]. Although simultaneous, **temporal total variation (tTV)**-regularized 4-D reconstruction constitutes an interesting alternative to cardiac motion compensation, a large scale evaluation on clinical data including quantitative validation remains subject of future work.

As mentioned multiple times throughout the thesis, reliable 2-D lumen segmentation and centerline extraction is a largely unsolved problem. Although very effective methods exist for static-gantry angiography [Dehk 11, Kerk 16], they are not easily applicable to rotational angiography as the lumen contrast and visibility is substantially different in every single view. Consequently, requiring sophisticated projection domain segmentation algorithms is a major drawback for virtually any motion compensation and reconstruction algorithm, including the methods proposed here. We believe that a simple yet effective method for projection domain background subtraction and segmentation, potentially based on *deep learning*, would have immediate and substantial impact on the clinical applicability of rotational coronary angiography.



# Summary

Within this thesis, we propose several contributions to respiratory motion compensation and 3-D reconstruction in rotational coronary angiography using interventional C-arm cone-beam scanners.

**Chap. 1** After a brief introduction to interventional C-arm [cone-beam computed tomography \(CBCT\)](#) imaging of the coronary arteries, we provide a detailed summary of contributions to the state-of-the-art in both coronary angiography and generic [CBCT](#) imaging, together with references to the respective publications. We conclude the first chapter with a written and illustrated overview of the organization of the thesis.

**Chap. 2** We provide information on the cardiac anatomy and physiology to motivate the importance of coronary artery health. Subsequently, atherosclerosis is introduced as a primary reason for [coronary heart disease \(CHD\)](#) leading to partial or total occlusion of the coronary artery lumen. In current clinical practice, stenoses are resolved via [percutaneous coronary interventions \(PCI\)](#), a minimally invasive, catheter-based technique that is performed under fluoroscopic guidance using C-arm angiography systems. Such scanners, in principal, also allow for the acquisition of projection sequences on a circular source trajectory (commonly referred to as rotational angiography) that enables 3-D reconstruction.

Following a brief description of the X-ray image formation process, we elaborate on the [CBCT](#) imaging geometry and our formulation based on projection matrices. Assuming ideal (i. e., uncorrupted) acquisitions, straight-forward tomographic 3-D reconstruction using analytic and algebraic algorithms is possible, the most famous representatives of which are discussed in greater detail. Unfortunately, these algorithms cannot be applied to rotational coronary angiography due to severe image corruption by truncation, as well as intra-scan cardiac and respiratory motion, that introduce inconsistency and corruption.

The chapter is concluded with a discussion of [data corruption metrics \(DCMs\)](#), i. e., image-based measures that allow for the quantification of image sequence corruption. We discuss two representatives of [DCMs](#): [Epipolar consistency conditions \(ECC\)](#) that follow immediately from the image formation and geometry, and [auto-focus measures \(AFMs\)](#) that exploit prior knowledge on favorable properties of reconstructed images.

**Chap. 3** Much work has addressed aforementioned challenges to enable 3-D reconstruction from rotational angiography. As the approaches are manifold, we focus on the most important methods related to the proposed algorithms. We organize this section by source of corruption and list the most influential related work w.r.t. to truncation (i.e., background subtraction vs. background suppression), cardiac motion (namely gating based on the ECG or other surrogates), and respiratory motion (particularly 3-D/2-D registration of uncompensated reconstructions with the projection data).

Considering an excellent and very recent review on the topic [Cime 16a], we briefly summarize the state-of-the-art in tomographic and symbolic reconstruction. We then provide details on streak-reduced, ECG-gated filtered backprojection (FBP), 3-D minimal path-computations, and on epipolar geometry- and graph cut-based centerline reconstruction, that will be used in Chap. 5, Chap. 6, and Chap. 7, respectively.

**Chap. 4** The algorithms devised within this thesis are evaluated on the same data basis that is introduced in this chapter. The data sets comprise of two *in silico* phantom sequences and three clinical scans.

The simulated data consists of two rotational angiograms exhibiting cardiac, and cardiac and respiratory motion, respectively, and were introduced as part of a publicly available bench mark for tomographic vasculature reconstruction, CAVAREV. The anatomy and physiology of CAVAREV is based on the well-known dynamic XCAT [Sega 01, Sega 08, Rohk 10c]. We extend the framework with both 3-D and 2-D centerlines [Unbe 17e], to enable quantitative evaluation of symbolic reconstruction algorithms.

Moreover, we apply our methods to three clinical rotational angiograms that were acquired on *Artis one* systems (Siemens Healthcare GmbH, Forchheim, Germany) at the Department of Cardiology, Friedrich-Alexander-Universität Erlangen-Nürnberg. The motion compensation and reconstruction methods proposed later in this thesis do not operate on projection images directly but require sparse input such as background subtracted angiograms (virtual digital subtraction angiography (vDSA) images) [Unbe 16c, Unbe 17a] or vessel centerlines [Unbe 17d, Unbe 17e]. Consequently, we devise a pipeline that automatically extracts vessel centerlines and background subtracted images from the acquired projections. The method relies on vessel enhancing filters [Koll 95, Fran 98] and minimal path computations to extract coronary artery centerlines and binary masks of the lumen in projection domain. A non-contrast background image is then estimated via spectral deconvolution of the segmentation mask and the acquired projection image [Aach 01, Unbe 16c].

As no appropriate ground truth is available, the proposed methods are evaluated qualitatively. The performance of the fully automatic pipeline is promising on both phantom and clinical data, yet, erroneous segmentations occur in posterior-anterior (P-A) views that exhibit substantial overlap of the vascular tree with the spine.

**Chap. 5** Respiratory motion compensation in rotational angiography is challenging, as respiration is quasi non-recurrent within a 5 s acquisition. Most existing methods rely on 3-D/2-D registration of a prior model, that cannot be obtained in presence of low frequency motion with large amplitudes. To overcome this substantial limi-

tation, we propose two respiratory motion compensation algorithms that are purely image-based and exploit [data corruption metrics](#) (DCMs).

First, we show that [vDSA](#) imaging as described in Chap. 4 voids truncation and, thus, enables the application of [Epipolar consistency conditions](#) (ECC) [[Aich 15a](#)], that are then optimized for the [superior-inferior](#) (S-I) motion of the heart during respiration [[Unbe 16c](#), [Unbe 17a](#)]. Second, we use sparsifying backprojection operators [[Li 11](#)] and projection domain centerlines to compute 3-D distance maps, the quality of which depends on intra-scan motion [[Unbe 17d](#)]. We quantify favorable properties of the cost maps using a task-based [auto-focus measure](#) (AFM), that favors pronounced local minima. The AFM is then optimized w.r.t. 3-D translational motion using discrete optimization, i.e.,  $\alpha$ -expansion moves on graph cuts, that is fit to handle large motion amplitudes.

Both methods are then evaluated quantitatively using projection and reconstruction domain error metrics derived from the epipolar geometry. Compared to the uncompensated case, both methods yield substantial improvements of all figures of merit. While the ECC-based method performed best w.r.t. the epipolar constraint, AFM proved superior w.r.t. a reconstruction domain metric, suggesting the need for a task-driven evaluation that is performed in Chap. 6.

**Chap. 6** Having addressed truncation and respiratory motion in previous chapters, Chap. 6 discusses a novel 4-D tomographic vasculature reconstruction algorithm that effectively handles the severe angular undersampling due to cardiac motion gating [[Taub 17c](#), [Taub 17a](#), [Unbe 17c](#)].

Rather than relying on motion compensation, the algorithm reconstructs 3-D volumes of multiple heart phases simultaneously and allows for communication among individual volumes using temporal regularizers, thus, implicitly using all acquired data. Reconstruction is formulated as a minimization problem comprising of a data fidelity term, and spatial and temporal regularizers based on the respective [TV](#) norm; a combination that can be optimized efficiently using a recent proximal splitting method [[Cond 13](#)] that is proven to converge.

We compare the proposed, iterative algorithm to a state-of-the-art analytic method and reconstruct 3-D volumes for all five data sets introduced in Chap. 4. Reconstructions are performed using both the uncompensated and respiratory motion corrected geometries, enabling a task-driven evaluation of the respiratory motion compensation schemes proposed in Chap. 5. For the CAVAREV data sets, reconstruction performance is assessed quantitatively using the Dice similarity coefficient. Due to the lack of proper ground truth, validation of the proposed methods on clinical acquisitions restricted to a qualitative analysis of the reconstructed volumes. The novel method paired with AFM-based correction substantially outperformed all competing combinations on both *in silico* and *in vivo* data, and is currently leading the CAVAREV score board for both phantom data sets.

**Chap. 7** Finally, we consider symbolic reconstruction algorithms that enable 3-D coronary artery centerline retrieval from very few projections only. The flexibility of these algorithms with respect to both the amount and the acquisition geometry of consistent views is enabled by requiring on very sparse projection domain informa-

tion, i.e., coronary artery centerlines. Unfortunately, despite numerous algorithms proposed for 2-D vasculature segmentation [Dehk 11], reliable extraction of projection domain centerlines in rotational angiography is not yet feasible in practice due to poor contrast of the vessels or overlap with strongly attenuating structures, such as the vertebrae. In the recent literature, this shortcoming is oftentimes concealed or avoided by requiring manual refinement and preprocessing steps to otherwise fully automatic algorithms [Cime 16a, Unbe 17e]. To alleviate the dependency on 2-D centerline quality, we propose generic extensions to asymmetric symbolic reconstruction algorithms.

We build upon two state-of-the-art centerline reconstruction methods based on explicit and implicit correspondence matching between 2-D centerlines [Blon 06, Liao 10] to reconstruct the 3-D vasculature from few views of a rotational angiography acquisition, that is still asymmetric due to reference frame selection. The output of aforementioned reconstruction algorithms is then used as input to our extensions that address symmetrization, consistency-based outlier removal, and projection domain-informed topology recovery.

For the phantom data where 3-D and 2-D ground truth is available, the evaluation comprises of both 3-D point cloud overlap and 2-D reprojection errors. As 3-D ground truth is unavailable for clinical acquisitions, we limit the analysis to 2-D reprojection errors w.r.t. manually extracted projection domain centerlines. In comparing the reconstruction performance of the extended to the original methods, we demonstrate that the proposed extensions promote robustness with respect to projection domain mis-segmentations and erroneous correspondences, translating to superior reconstruction quality.

**Chap. 8** We summarize research questions that should be addressed in future work. Discrete optimization of AFMs is beneficial for large displacements but proves challenging when more complex motion models are of interest. We plan on investigating continuous optimization methods, e.g., stochastic gradient descent, in cases where smaller motion amplitudes are anticipated. Moreover, we seek to study the application of ECC in experimental imaging geometries such as DARCA. Given the importance of projection domain vessel segmentation and background estimation, we anticipate a substantial interest in novel methods that are simple, yet effectively address the challenges associated with vessel segmentation in rotational angiography.

# List of Acronyms

## **AFM**

auto-focus measure ii, III, 2, 5, 19–21, 42, 46, 48, 50, 51, 57–62, 72, 77, 79, 83, 85, 87, 88, 93, 97, 99

## **AS**

Amsterdam Shroud 26

## **bpm**

beats per minute 18

## **CBCT**

cone-beam computed tomography i, 2–4, 9–13, 16, 17, 19, 23, 41, 85, 93, 95, 99

## **CC**

consistency conditions 4, 19, 20, 23, 25, 40, 54

## **CHD**

coronary heart disease 7, 8, 85

## **CNN**

convolutional neural network 24

## **CT**

computed tomography 33

## **CTA**

computed tomography angiography 63

## **CVD**

cardiovascular disease 7

## **DAE**

denoising auto-encoder 24

## **DARCA**

dual axis rotational angiography 26, 83, 88

## **DCM**

data corruption metric 2, 3, 5, 19, 25, 41, 52, 85, 87, 93

**DID**

detector-isocenter-distance 11

**DSA**

digital subtraction angiography 9, 23, 24

**ECC**

Epipolar consistency conditions ii, III, 2, 5, 19, 41, 46, 48, 50–52, 57–62, 77, 83, 85, 87, 88, 93, 97, 99

**ECG**

electrocardiogram 2, 7, 25, 26, 28, 45, 56, 57, 62, 86

**FBP**

filtered backprojection 14, 15, 28, 29, 61, 86

**FCC**

Fourier consistency conditions 19

**FDK**

Feldkamp-Davis-Kress 15, 23, 54, 56–63

**FOV**

field of view 16, 17, 23, 38, 41

**FP**

flat panel 11

**HLCC**

Helgason-Ludwig consistency conditions 19

**L-R**

left-right 18

**LAD**

left anterior descending artery 7, 18

**LCA**

left coronary artery 7, 9, 18, 34

**LCX**

left circumflex artery 7, 18

**LV**

left ventricle 2, 18



**MIP**

maximum intensity projection 28

**MRA**

magnetic resonance angiography 4

**MRI**

magnetic resonance imaging 33

**MST**

minimum spanning tree 67–69, 75, 76

**P-A**

posterior-anterior 18, 67, 86

**PCI**

percutaneous coronary interventions 8, 85

**RCA**

right coronary artery 7

**ROI**

region of interest 23, 24, 54, 55

**S-I**

superior-inferior 18, 50, 52, 87

**SDD**

source-detector-distance 11, 17, 35

**SID**

source-isocenter-distance 11, 17, 35

**SSIM**

structural similarity index 40

**sTV**

spatial total variation 16, 19, 55, 56, 59, 62, 63, 95

**tTV**

temporal total variation III, 19, 55–63, 83, 95

**TV**

total variation 53, 56, 87

**vDSA**

virtual digital subtraction angiography [III](#), [2](#), [24](#), [33](#), [37–41](#), [54–57](#), [62](#), [63](#), [86](#), [87](#), [97](#)

# List of Symbols

$AF$	Value of the <a href="#">AFM DCM</a> .
$\Delta\lambda$	Angular spacing between two subsequent projections.
$\mathbf{a}$	Arbitrary vector in $N$ -dimensional space.
$\gamma_c$	Cone-angle dependent on detector coordinate $u_2$ .
$N_u$	Dimension of the detector, i. e., projection, domain. $N_u = 2$ for <a href="#">CBCT</a> imaging.
$\underline{u}_3$	Depth of detector point w. r. t. X-ray source position.
$\mathbf{u}$	An arbitrary detector domain point in pixels.
$\mathbf{u}^c$	An arbitrary detector domain point in mm.
$u_1$	Horizontal detector coordinate in pixels.
$u_1^c$	Horizontal detector coordinate in mm.
$\mathbf{e}_{u_1}$	Unit vector in $u_1$ direction.
$\mathbf{e}_{u_2}$	Unit vector in $u_2$ direction.
$u_2$	Vertical detector coordinate in pixels.
$u_2^c$	Vertical detector coordinate in mm.
$D_{DI}$	Detector-isocenter-distance.
$N$	Arbitrary dimension of a currently considered object.
$\mathbf{r}$	Direction vector of a X-ray beam
$EC$	Value of the <a href="#">ECC DCM</a> .
$e_{\text{Phot}}$	Elementary charge of a photon $\approx 1.602 \times 10^{-19}$ C
$\kappa$	Angle of an epipolar plane w. r. t. to the principal rays of frames $i_1$ and $i_2$ .
$\underline{\mathbf{l}}_{i_1}^{i_2}$	Epipolar line in frame $i_1$ arising from the epipolar geometry between frames $i_1$ and $i_2$ .
$\beta$	Angle of an epipolar line w. r. t. to the $u_1$ axis.
$\underline{\epsilon}_{i_1}^{i_2}$	Epipolar plane around the baseline of frames $i_1$ and $i_2$ .

$\gamma_f$	Fan-angle dependent on detector coordinate $u_1$ .
$\cdot$	Mapping from Euclidean to projective coordinates.
$h(\cdot)$	Mapping from projective to Euclidean coordinates.
$\rho_i(\mathbf{l})$	Integration over a line in frame $i$ .
$\mathbf{K}$	Mapping from world to detector coordinates.
$\iota_{\mathbb{R}_+}(\cdot)$	Non-negativity constraint.
$N_0$	Number of photons emitted by the X-ray tube
$N_P$	Number of photons after attenuation by an object
$N_u$	Total number of pixels in one projection image.
$U_1$	Number of pixels in horizontal detector direction.
$U_2$	Number of pixels in vertical detector direction.
$N_\lambda$	Number of projection images acquired during a circular scan.
$N_x$	Total number of voxels in $\mathbf{f}$ .
$X_1$	Number of voxels in $\mathbf{e}_{x_1}$ direction.
$X_2$	Number of voxels in $\mathbf{e}_{x_2}$ direction.
$X_3$	Number of voxels in $\mathbf{e}_{x_3}$ direction.
$f$	Function describing the attenuation properties of a certain object
$\mathbf{f}$	Discrete, vectorized representation of the object function $f$ .
$E_P$	Energy of a photon in $\text{e}_{\text{Phot}}\text{V}$
$E_{\text{max}}$	Maximum photon energy $\text{e}_{\text{Phot}}\text{V}$
$\mathbf{p}$	Principal point in pixels.
$\mathbf{p}^c$	Principal point in mm.
$i$	Index referring to distinct views.
$\mathcal{I}$	Projection image in detector domain.
$\tilde{\mathcal{I}}$	Projection image in detector domain after cosine weighting and row-wise ramp filtering.
$\mathbf{P}$	Projection matrix describing the mapping from homogeneous world to detector coordinates.

$\mathcal{I}$	Discrete, vectorized representation of the set of projection images $\mathcal{I}^i, i = 1, \dots, N_\lambda$ .
$w_{\text{red}}$	Redundancy weights.
$\mathbf{R}$	Arbitrary rotation matrix.
$\mathbf{R}_{x_1}$	Rotation matrix describing a rotation around the $\mathbf{e}_{x_1}$ axis.
$\mathbf{R}_{x_2}$	Rotation matrix describing a rotation around the $\mathbf{e}_{x_2}$ axis.
$\mathbf{R}_{x_3}$	Rotation matrix describing a rotation around the $\mathbf{e}_{x_3}$ axis.
$\lambda$	Rotation angle on a circular trajectory.
$\mathbf{D}_s$	Spatial forward difference operator.
$D_{\text{SD}}$	Source-detector-distance.
$D_{\text{SI}}$	Source-isocenter-distance.
$t$	Signed distance of an epipolar line to the principal point.
$k_s$	Skewness between the detector $u_1$ and $u_2$ axis.
$\mathbf{o}$	X-ray source position
$\Delta u_1$	Horizontal detector spacing.
$\Delta u_2$	Vertical detector spacing.
$\mu_s$	Lagrange multiplier for <b>sTV</b> regularization.
$\ \cdot\ _{\text{sTV}}$	<b>sTV</b> norm.
$\mathbf{M}$	System matrix describing the X-ray transform for a particular geometry.
$\mathbf{D}_t$	Temporal forward difference operator.
$\mu_t$	Lagrange multiplier for <b>tTV</b> regularization.
$\ \cdot\ _{\text{tTV}}$	<b>tTV</b> norm.
$\mathbf{t}$	Arbitrary translation vector.
$I_{\text{Tube}}$	Tube current through filament measured in A
$U_{\text{Tube}}$	Tube voltage between cathode and anode in V
$N_x$	Dimension of the object domain. $N_x = 3$ for <b>CBCT</b> imaging.
$\mathbf{x}$	An arbitrary object domain point.
$\mathbf{e}_{x_1}$	Unit vector in $x_1$ direction.

$\mathbf{e}_{x_2}$	Unit vector in $x_2$ direction.
$\mathbf{e}_{x_3}$	Unit vector in $x_3$ direction.
$x_1$	First dimension of world coordinates.
$x_2$	Second dimension of world coordinates.
$x_3$	Third dimension of world coordinates.
$c^i$	Linear cardiac time corresponding to projection image $\mathcal{I}^i$ .
$w_c(i, j)$	Gating weight of cardiac phase $c^j$ w.r.t. to $c^i$ .
$l_{\mathbf{u}}$	Depth plane assigned to detector point $\mathbf{u}$ .
$T_r^i$	Displacement field defined describing a 3-D warping from the motion state at $c^r$ to $c^i$ .
$\Lambda$	Projection domain distance transform of a set of points.
$a_g$	Exponent of cosine-based gating function.
$w_g$	Window width of cosine-based gating function.
$N_{\text{ign}}$	Number of smallest and largest contributions ignored for each voxel.
$L$	Number of equi-depth planes.
$f^r$	Function describing the attenuation properties of a certain object at cardiac phase $c^r$ .
$\mathbf{f}^r$	Discrete, vectorized representation of the object function $f^r$ at cardiac phase $c^r$ .
$g^r$	Function describing the cost map at cardiac phase $c^r$ .
$\Delta L$	Spacing between equi-depth planes.
$\mathcal{B}$	An estimate of projection image $\mathcal{I}$ without contrast enhancement.
$\mathbf{b}$	The estimated background image in Fourier domain.
$B$	Blobness according to Frangi et al..
$\mathcal{G}_c^i$	3-D CAVAREV ground-truth centerlines at motion state $i$ for the data set containing cardiac motion only.
$\mathcal{G}_b^i$	3-D CAVAREV ground-truth centerlines at motion state $i$ for the data set containing cardiac and respiratory motion.
$g_c^i$	3-D CAVAREV ground-truth volume of the lumen at motion state $i$ for the data set containing cardiac motion only.

$g_b^i$	3-D CAVAREV ground-truth volume of the lumen at motion state $i$ for the data set containing cardiac and respiratory motion.
$\mathcal{B}$	A branch of the centerline tree in projection domain.
$\mathcal{T}$	Centerline tree in a projection domain.
$\mathcal{G}$	A projection image after artificial corruption using the segmentation mask $\mathcal{W}$ .
$g$	The corrupted image in Fourier domain.
$\mathcal{D}$	A <b>vDSA</b> image obtained from subtracting $\mathcal{B}$ from $\mathcal{I}$ .
$\mathcal{D}$	Vectorized version of the <b>vDSA</b> image sequence.
$\nu$	Eigenvalue of the Hessian matrix.
$G_\sigma$	A Gaussian kernel of scale $\sigma$ .
$\mathbf{H}(\mathbf{u}, \sigma)$	The Hessian matrix at detector point $\mathbf{u}$ at scale $\sigma$ .
$\mathcal{K}$	Koller filtered version of projection image $\mathcal{I}$ .
$\alpha$	Orientation of a 2-D curvilinear structure.
$\sigma$	Standard deviation of a Gaussian kernel for scale space filtering.
$\mathcal{W}$	Binary segmentation mask that is unity for vessels and zero everywhere else.
$\overline{w}$	Inverse binary segmentation mask in Fourier domain.
$S$	Structureness according to Frangi et al..
$\mathbf{e}_\alpha$	Unit vector orthogonal to the orientation $\alpha$ in 2-D.
$\mathcal{V}$	Vesselness filtered version of projection image $\mathcal{I}$ .
$\varphi$	A particular B-spline control point.
$\mathbf{F}_i^j$	The fundamental matrix between view $i$ and view $j$ .
$\xi_j^i$	Key point $j$ in frame $i$ .
$\gamma$	A motion state.
$K$	Number of B-spline control points.
$Q$	Number of key points extracted per frame.
$R$	Number of reference heart phases.
$\mathbf{P}_A$	Projection matrix after <b>AFM</b> -based correction.
$\mathbf{P}_E$	Projection matrix after <b>ECC</b> -based correction.

$\Phi$	Set of B-spline control points $\varphi_k$ .
$\mathbf{G}_s$	Spatial gradient for primal dual optimization.
$\mathbf{G}_t$	Temporal gradient for primal dual optimization.
$N_c$	Number of images remaining after nearest neighbor gating w.r.t. a specific cardiac phase.
$N_r$	Number of asymmetrically reconstructed sets of points.
$\tilde{O}$	Area under the overlap curve.
$\text{RE}^{\text{mean}}$	Mean reprojection error.
$\mathcal{R}$	Set of reconstructed 3-D points.



# List of Figures

1.1	Organization of the thesis. . . . .	5
2.1	Schematic of the cardiac anatomy. . . . .	8
2.2	Example of fluoroscopic angiography. . . . .	9
2.3	Overview of the <b>CBCT</b> imaging geometry. . . . .	12
2.4	Schematic illustration of intra-scan motion. . . . .	17
2.5	Relations in the <b>ECC</b> . . . . .	20
3.1	Schematic of single frame subtraction imaging. . . . .	24
3.2	Different approach to ECG gating. . . . .	26
3.3	Ambiguity of matching using the epipolar constraint. . . . .	30
3.4	Geometric relations for implicit correspondence matching. . . . .	31
4.1	Representative results of the automatic preprocessing algorithms. . .	39
4.2	Erroneous segmentations due to overlap with high contrast objects. .	40
5.1	Illustration of phase resolved cost map generation. . . . .	42
5.2	Illustration of epipolar geometry-based evaluation. . . . .	46
5.3	Shifts estimated using <b>ECC</b> and <b>AFM</b> . . . . .	48
5.4	2-D and 3-D error curves. . . . .	49
6.1	Tomographic reconstructions of <b>CARD</b> . . . . .	57
6.2	Volume renderings for tomographic reconstructions of <b>CARDBREATH</b> . .	58
6.3	Volume renderings for tomographic reconstructions of <b>R1</b> . . . . .	59
6.4	Volume renderings for tomographic reconstructions of <b>R2</b> . . . . .	60
6.5	Volume renderings for tomographic reconstructions of <b>R3</b> . . . . .	60
7.1	Edge cost computation in 3-D using reprojection. . . . .	68
7.2	Illustration of the overlap computation. . . . .	70
7.3	Outlier generation via Brownian motion. . . . .	71
7.4	Overlap curves describing average reconstruction results. . . . .	73
7.5	Reprojections of the reconstruction results of <b>CARD</b> . . . . .	76
7.6	Reprojections of the reconstruction results of clinical data. . . . .	78



# List of Tables

2.1	Maximum displacements of coronary arteries during respiration. . . .	18
4.1	Acquisition parameters for the phantom and clinical data sets. . . . .	35
4.2	Parameters for segmentation algorithms. . . . .	38
5.1	Results: Respiratory motion compensation, projection domain error. .	50
5.2	Results: Respiratory motion compensation, reconstruction domain error.	50
6.1	Results: Dice scores of the CAVAREV study including respiratory motion.	61
6.2	Results: Comparison with the previous methods. . . . .	62
7.1	Area under the overlap curve for CARD. . . . .	74
7.2	Mean reprojection error for CARD. . . . .	74
7.3	Area under the overlap curve for CARDBREATH. . . . .	77
7.4	Mean reprojection error for CARDBREATH. . . . .	78
7.5	Mean reprojection errors for clinical data. . . . .	79



# Bibliography

- [Aach 01] T. Aach and V. H. Metzler. “Defect interpolation in digital radiography: how object-oriented transform coding helps”. In: *Proc. SPIE Medical Imaging*, pp. 824–835, International Society for Optics and Photonics, 2001.
- [Abe 02] T. Abe, M. Hirohata, N. Tanaka, Y. Uchiyama, K. Kojima, K. Fujimoto, A. M. Norbash, and N. Hayabuchi. “Clinical benefits of rotational 3D angiography in endovascular treatment of ruptured cerebral aneurysm”. *American Journal of Neuroradiology*, Vol. 23, No. 4, pp. 686–688, 2002.
- [Aich 15a] A. Aichert, M. Berger, J. Wang, N. Maass, A. Doerfler, J. Hornegger, and A. K. Maier. “Epipolar Consistency in Transmission Imaging”. *IEEE Transactions on Medical Imaging*, Vol. 34, No. 11, pp. 2205–2219, 2015.
- [Aich 15b] A. Aichert, J. Wang, R. Schaffert, A. Dörfler, J. Hornegger, and A. Maier. “Epipolar Consistency in Fluoroscopy for Image-Based Tracking”. In: *Proceedings of the British Machine Vision Conference 2015*, 2015.
- [Andr 08] A. Andriotis, A. Zifan, M. Gavaises, P. Liatsis, I. Pantos, A. Theodorakakos, E. P. Efstathopoulos, and D. Katritsis. “A new method of three-dimensional coronary artery reconstruction from X-ray angiography: Validation against a virtual phantom and multislice computed tomography”. *Catheterization and Cardiovascular Interventions*, Vol. 71, No. 1, pp. 28–43, 2008.
- [Arms 06] P. W. Armstrong. “A comparison of pharmacologic therapy with/without timely coronary intervention vs. primary percutaneous intervention early after ST-elevation myocardial infarction: the WEST (Which Early ST-elevation myocardial infarction Therapy) study”. *European Heart Journal*, Vol. 27, No. 13, pp. 1530–1538, 2006.
- [Baka 14] N. Baka, C. Metz, C. J. Schultz, R.-J. van Geuns, W. J. Niessen, and T. van Walsum. “Oriented Gaussian mixture models for nonrigid 2D/3D coronary artery registration”. *IEEE Transactions on Medical Imaging*, Vol. 33, No. 5, pp. 1023–1034, 2014.
- [Baka 15] N. Baka, B. Lelieveldt, C. Schultz, W. Niessen, and T. van Walsum. “Respiratory motion estimation in x-ray angiography for improved guidance during coronary interventions”. *Physics in Medicine and Biology*, Vol. 60, No. 9, p. 3617, 2015.
- [Barr 04] J. F. Barrett and N. Keat. “Artifacts in CT: recognition and avoidance 1”. *Radiographics*, Vol. 24, No. 6, pp. 1679–1691, 2004.
- [Baye 14] Bayer Pharma AG. “Ultravist®-370”. [http://labeling.bayerhealthcare.com/html/products/pi/Ultravist\\_PI.pdf](http://labeling.bayerhealthcare.com/html/products/pi/Ultravist_PI.pdf), 2014. Accessed: 2017-03-09.
- [Bent 02] Y. Bentoutou, N. Taleb, M. C. El Mezouar, M. Taleb, and L. Jetto. “An invariant approach for image registration in digital subtraction angiography”. *Pattern Recognition*, Vol. 35, No. 12, pp. 2853–2865, 2002.

- [Berg 14] M. Berger, C. Forman, C. Schwemmer, J. H. Choi, K. Müller, A. Maier, J. Hornegger, and R. Fahrig. “Automatic removal of externally attached fiducial markers in cone beam C-arm CT”. In: *Bildverarbeitung für die Medizin 2014*, pp. 318–323, Springer, 2014.
- [Berg 16] M. Berger, K. Müller, A. Aichert, M. Unberath, J. Thies, J.-H. Choi, R. Fahrig, and A. Maier. “Marker-free motion correction in weight-bearing cone-beam CT of the knee joint”. *Medical Physics*, Vol. 43, No. 3, pp. 1235–1248, 2016.
- [Berg 17] M. Berger, Y. Xia, W. Aichinger, K. Mentl, M. Unberath, A. Aichert, C. Riess, J. Hornegger, R. Fahrig, and A. Maier. “Translational Motion Compensation for Cone-Beam CT Using Fourier Consistency Conditions”. *Physics in Medicine and Biology*, 2017. (under revision).
- [Bett 13] G. J. Betts *et al.* *Anatomy & Physiology*. Open Stax College, 2013.
- [Bier 16] B. Bier, M. Berger, J. Maier, M. Unberath, S. Hsieh, S. Bonaretti, R. Fahrig, M. E. Levenston, G. E. Gold, and A. Maier. “Object Removal in Gradient Domain of Cone-Beam CT Projections”. In: *Proc. IEEE Nuclear Science Symposium & Medical Imaging Conference (NSS/MIC)*, 2016.
- [Bier 17a] B. Bier, A. Aichert, L. Felsner, M. Unberath, M. Levenston, G. Gold, R. Fahrig, and A. Maier. “Epipolar Consistency Conditions for Motion Correction in Weight-Bearing Imaging”. In: *Bildverarbeitung für die Medizin 2017*, pp. 209–214, Springer, 2017.
- [Bier 17b] B. Bier, M. Berger, A. Maier, M. Kachelrieß, L. Ritschl, K. Müller, J.-H. Choi, and R. Fahrig. “Scatter Correction Using a Primary Modulator on a Clinical Angiography C-arm CT System”. *Medical Physics*, 2017.
- [Bier 17c] B. Bier, M. Unberath, T. Geimer, J. Maier, G. Gold, M. Levenston, R. Fahrig, and A. Maier. “Motion Compensation using Range Imaging in C-arm Cone-Beam CT”. In: *Proc. Medical Image Understanding and Analysis*, Springer, 2017. (under review).
- [Blon 04] C. Blondel, R. Vaillant, G. Malandain, and N. Ayache. “3D tomographic reconstruction of coronary arteries using a precomputed 4D motion field”. *Physics in Medicine and Biology*, Vol. 49, No. 11, pp. 2197–2208, 2004.
- [Blon 06] C. Blondel, G. Malandain, R. Vaillant, and N. Ayache. “Reconstruction of coronary arteries from a single rotational X-ray projection sequence.”. *IEEE Transactions on Medical Imaging*, Vol. 25, No. 5, pp. 653–63, 2006.
- [Blue 08] D. A. Bluemke, S. Achenbach, M. Budoff, T. C. Gerber, B. Gersh, L. D. Hillis, W. G. Hundley, W. J. Manning, B. F. Printz, M. Stuber, *et al.* “Noninvasive Coronary Artery Imaging”. *Circulation*, Vol. 118, No. 5, pp. 586–606, 2008.
- [Boge 16] M. Bögel, S. Gehrisch, T. Redel, C. Rohkohl, P. Hölter, A. Dörfler, A. Maier, and M. Kowarschik. “Patient-individualized boundary conditions for CFD simulations using time-resolved 3D angiography”. *International Journal of Computer Assisted Radiology and Surgery*, Vol. 11, No. 6, pp. 1061–1069, 2016.

- [Bopp 16] J. Bopp, M. Unberath, S. Steidl, R. Fahrig, I. Oliveira, A. Kleyer, and A. Maier. “Automatic Finger Joint Detection for Volumetric Hand Imaging”. In: *Bildverarbeitung für die Medizin 2016*, pp. 104–109, Springer, 2016.
- [Boyk 01] Y. Boykov, O. Veksler, and R. Zabih. “Fast approximate energy minimization via graph cuts”. *IEEE Transactions on Pattern Analysis and Machine Intelligence*, Vol. 23, No. 11, pp. 1222–1239, 2001.
- [Broo 76] R. A. Brooks and G. Di Chiro. “Beam hardening in x-ray reconstructive tomography”. *Physics in Medicine and Biology*, Vol. 21, No. 3, p. 390, 1976.
- [Bros 10] A. Brost, R. Liao, N. Strobel, and J. Hornegger. “Respiratory motion compensation by model-based catheter tracking during EP procedures”. *Medical Image Analysis*, Vol. 14, No. 5, pp. 695–706, 2010.
- [Bros 15] R. Brosig, S. G. Hariharan, D. Volpi, M. Kowarschik, S. Carlier, N. Navab, and S. Demirci. “Implicit Background Subtraction for Cardiac Digital Angiography”. In: *Joint MICCAI workshops on Computing and Visualization for Intravascular Imaging and Computer-Assisted Stenting*, pp. 50–57, 2015.
- [Buda 13] A. Budai, R. Bock, A. Maier, J. Hornegger, and G. Michelson. “Robust Vessel Segmentation in Fundus Images”. *International Journal of Biomedical Imaging*, Vol. 2013, 2013.
- [Buzu 08] T. M. Buzug. *Computed Tomography: From Photon Statistics to Modern Cone-Beam CT*. Springer Berlin Heidelberg, 1 Ed., 2008.
- [Byrn 02] C. Byrne. “Iterative oblique projection onto convex sets and the split feasibility problem”. *Inverse Problems*, Vol. 18, No. 2, p. 441, 2002.
- [Cai 15] N. Cai, Z. Su, Z. Lin, H. Wang, Z. Yang, and B. W.-K. Ling. “Blind inpainting using the fully convolutional neural network”. *The Visual Computer*, pp. 1–13, 2015.
- [Cann 86] J. Canny. “A computational approach to edge detection”. *IEEE Transactions on Pattern Analysis and Machine Intelligence*, No. 6, pp. 679–698, 1986.
- [Card 12] R. Cardenas, A. Novikov, J. Gunn, R. Hose, and A. F. Frangi. “3D reconstruction of coronary arteries from rotational X-ray angiography”. In: *Proc. International Symposium on Biomedical Imaging (ISBI) 2012*, pp. 618–621, IEEE, 2012.
- [Cham 11] A. Chambolle and T. Pock. “A first-order primal-dual algorithm for convex problems with applications to imaging”. *Journal of Mathematical Imaging and Vision*, Vol. 40, No. 1, pp. 120–145, 2011.
- [Chan 04] F. Chang, C.-J. Chen, and C.-J. Lu. “A linear-time component-labeling algorithm using contour tracing technique”. *Computer Vision and Image Understanding*, Vol. 93, No. 2, pp. 206–220, 2004.
- [Chen 08] G.-H. Chen, J. Tang, and S. Leng. “Prior image constrained compressed sensing (PICCS): a method to accurately reconstruct dynamic CT images from highly undersampled projection data sets”. *Medical Physics*, Vol. 35, No. 2, pp. 660–663, 2008.

- [Chen 12] G.-H. Chen, P. Thériault-Lauzier, J. Tang, B. Nett, S. Leng, J. Zambelli, Z. Qi, N. Bevins, A. Raval, S. Reeder, *et al.* “Time-resolved interventional cardiac C-arm cone-beam CT: An application of the PICCS algorithm”. *IEEE Transactions on Medical Imaging*, Vol. 31, No. 4, pp. 907–923, 2012.
- [Chil 81] W. A. Chilcote, M. T. Modic, W. A. Pavlicek, J. Little, A. J. Furlan, P. Duchesneau, and M. Weinstein. “Digital subtraction angiography of the carotid arteries: a comparative study in 100 patients.”. *Radiology*, Vol. 139, No. 2, pp. 287–295, 1981.
- [Choi 14] J.-H. Choi, A. Maier, A. Keil, S. Pal, E. J. McWalter, G. S. Beaupré, G. E. Gold, and R. Fahrig. “Fiducial marker-based correction for involuntary motion in weight-bearing C-arm CT scanning of knees. II. Experiment”. *Medical Physics*, Vol. 41, No. 6, 2014.
- [Chun 04] C. S. Chung, M. Karamanoglu, and S. J. Kovács. “Duration of diastole and its phases as a function of heart rate during supine bicycle exercise.”. *American Journal of Physiology. Heart and Circulatory Physiology*, Vol. 287, No. 5, pp. H2003–8, 2004.
- [Cies 84] A. Cieslinski, W. Hui, P. Oldershaw, G. Gregoratos, and D. Gibson. “Interaction between systolic and diastolic time intervals in atrial fibrillation”. *British Heart Journal*, Vol. 51, No. 4, pp. 431–437, 1984.
- [Cime 16a] S. Çimen, A. Gooya, M. Grass, and A. F. Frangi. “Reconstruction of coronary arteries from X-ray angiography: A review”. *Medical Image Analysis*, Vol. 32, pp. 46–68, 2016.
- [Cime 16b] S. Çimen, A. Gooya, N. Ravikumar, Z. A. Taylor, and A. F. Frangi. “Reconstruction of Coronary Artery Centrelines from X-Ray Angiography Using a Mixture of Student’s t-Distributions”. In: *Proc. Medical Image Computing and Computer Assisted Intervention (MICCAI) 2016*, pp. 291–299, Springer, 2016.
- [Cime 17] S. Çimen, A. F. Frangi, A. Maier, and M. Unberath. “CoronARe: Coronary Artery Reconstruction Challenge”. <http://www.miccai2017.org/satellite-events>, 2017. Accessed: 2017-03-20.
- [Cond 13] L. Condat. “A primal–dual splitting method for convex optimization involving Lipschitzian, proximable and linear composite terms”. *Journal of Optimization Theory and Applications*, Vol. 158, No. 2, pp. 460–479, 2013.
- [Cond 14] L. Condat. “A generic proximal algorithm for convex optimization—application to total variation minimization”. *IEEE Signal Processing Letters*, Vol. 21, No. 8, pp. 985–989, 2014.
- [Debb 13] C. Debbeler, N. Maass, M. Elter, F. Dennerlein, and T. M. Buzug. “A new CT rawdata redundancy measure applied to automated misalignment correction”. In: *Proc. Fully Three-Dimensional Image Reconstruction in Radiology and Nuclear Medicine*, pp. 264–267, 2013.
- [Dehk 11] M. T. Dehkordi, S. Sadri, and A. Doosthoseini. “A review of coronary vessel segmentation algorithms”. *Journal of Medical Signals and Aensors*, Vol. 1, No. 1, p. 49, 2011.
- [Denn 13] F. Dennerlein and A. Maier. “Approximate truncation robust computed tomography – ATTRACT”. *Physics in Medicine and Biology*, Vol. 58, No. 17, p. 6133, 2013.



- [Dijk 59] E. W. Dijkstra. “A note on two problems in connexion with graphs”. *Numerische mathematik*, Vol. 1, No. 1, pp. 269–271, 1959.
- [Edho 86] P. R. Edholm, R. M. Lewitt, and B. Lindholm. “Novel Properties Of The Fourier Decomposition Of The Sinogram”. In: *Proc. SPIE 0671*, pp. 8–18, 1986.
- [Fahr 06] R. Fahrig, R. Dixon, T. Payne, R. L. Morin, A. Ganguly, and N. Strobel. “Dose and image quality for a cone-beam C-arm CT system”. *Medical Physics*, Vol. 33, No. 12, pp. 4541–4550, 2006.
- [Feld 84] L. A. Feldkamp, L. C. Davis, and J. W. Kress. “Practical cone-beam algorithm”. *Journal of the Optical Society of America A*, Vol. 1, No. 6, pp. 612–619, 1984.
- [Fisc 15] P. Fischer, T. Pohl, A. Maier, and J. Hornegger. “Surrogate-Driven Estimation of Respiratory Motion and Layers in X-Ray Fluoroscopy”. In: *Proc. Medical Image Computing and Computer-Assisted Intervention (MICCAI) 2015*, pp. 282–289, 2015.
- [Fitz 88] J. M. Fitzpatrick, J. J. Grefenstette, D. R. Pickens, M. Mazer, and J. M. Perry. “A system for image registration in digital subtraction angiography”. In: *Information Processing in Medical Imaging*, pp. 415–435, Springer, 1988.
- [Fran 98] A. F. Frangi, W. J. Niessen, K. L. Vincken, and M. A. Viergever. “Multiscale vessel enhancement filtering”. In: *Proc. Medical Image Computing and Computer-Assisted Intervention (MICCAI) 1998*, pp. 130–137, Springer, 1998.
- [Frys 15] R. Frysck and G. Rose. “Rigid Motion Compensation in Interventional C-arm CT Using Consistency Measure on Projection Data”. In: N. Navab, J. Hornegger, M. W. Wells, and F. A. Frangi, Eds., *Proc. Medical Image Computing and Computer-Assisted Intervention*, pp. 298–306, Springer, 2015.
- [Gao 16] Z. Gao, Y. Zeng, J. Sun, J. Yang, Y. Zhou, M. Zhou, and T. Song. “Application of low injection rate and low contrast agent dose in three-dimensional rotational digital subtraction angiography of the intracranial aneurysm”. *Interventional Neuroradiology*, Vol. 22, No. 3, pp. 287–292, 2016.
- [Geim 16] T. Geimer, M. Unberath, O. Taubmann, C. Bert, and A. Maier. “Combination of Markerless Surrogates for Motion Estimation in Radiation Therapy”. In: *Computer Assisted Radiology and Surgery (CARS) 2016, Congress and Exhibition*, pp. 59–60, 2016.
- [Geim 17a] T. Geimer, A. Birlutiu, M. Unberath, O. Taubmann, C. Bert, and A. Maier. “A Kernel Ridge Regression Model for Respiratory Motion Estimation in Radiotherapy”. In: *Bildverarbeitung für die Medizin 2017*, pp. 155–160, Springer, 2017.
- [Geim 17b] T. Geimer, M. Unberath, A. Birlutiu, O. Taubmann, J. Wölfelschneider, C. Bert, and A. Maier. “A Kernel-based Framework for Intra-fractional Respiratory Motion Estimation in Radiation Therapy”. In: *Proc. International Symposium on Biomedical Imaging*, 2017. (to appear).
- [Gray 18] H. Gray. *Anatomy of the human body*. Lea & Febiger, 1918.

- [Grec 12] M. Grech, J. Debono, R. G. Xuereb, A. Fenech, and V. Grech. “A comparison between dual axis rotational coronary angiography and conventional coronary angiography”. *Catheterization and Cardiovascular Interventions*, Vol. 80, No. 4, pp. 576–580, 2012.
- [Guyt 11] J. Guyton and J. E. Hall. “Textbook of Medical Physiology”. 2011.
- [Hans 08a] E. Hansis, D. Schäfer, O. Dössel, and M. Grass. “Automatic optimum phase point selection based on centerline consistency for 3D rotational coronary angiography”. *International Journal of Computer Assisted Radiology and Surgery*, Vol. 3, No. 3, pp. 355–361, 2008.
- [Hans 08b] E. Hansis, D. Schafer, O. Dossel, and M. Grass. “Evaluation of iterative sparse object reconstruction from few projections for 3-D rotational coronary angiography”. *IEEE Transactions on Medical Imaging*, Vol. 27, No. 11, pp. 1548–1555, 2008.
- [Harr 78] F. J. Harris. “On the use of windows for harmonic analysis with the discrete Fourier transform”. *Proceedings of the IEEE*, Vol. 66, No. 1, pp. 51–83, 1978.
- [Hart 04] R. Hartley and A. Zisserman. *Multiple view geometry in computer vision*. Cambridge University Press, 2 Ed., 2004.
- [Helg 80] S. Helgason. “Support of Radon transforms”. *Advances in Mathematics*, Vol. 38, No. 1, pp. 91–100, Oct 1980.
- [Hett 10] H. Hetterich, T. Redel, G. Lauritsch, C. Rohkohl, and J. Rieber. “New X-ray imaging modalities and their integration with intravascular imaging and interventions”. *The International Journal of Cardiovascular Imaging*, Vol. 26, No. 7, pp. 797–808, 2010.
- [Hoff 00] K. R. Hoffmann, A. Sen, L. Lan, K.-G. Chua, J. Esthappan, and M. Mazzucco. “A system for determination of 3D vessel tree centerlines from biplane images”. *The International Journal of Cardiac Imaging*, Vol. 16, No. 5, pp. 315–330, 2000.
- [Hopp 08] S. Hoppe. *Accurate cone-beam image reconstruction in C-Arm computed tomography*. PhD thesis, Friedrich-Alexander-Universität Erlangen-Nürnberg, 2008.
- [Horn 16] J. Hornegger, A. Maier, and M. Kowarschik. *CT Image Reconstruction Basics*, pp. 01–09. LWW, Alphen aan den Rijn, Netherlands, 1 Ed., 2016.
- [Hoss 06] H. G. Hosseini, D. Luo, and K. J. Reynolds. “The comparison of different feed forward neural network architectures for ECG signal diagnosis”. *Medical Engineering & Physics*, Vol. 28, No. 4, pp. 372–378, 2006.
- [Hu 12] Y. Hu, M. Jung, A. Oukili, G. Yang, J.-C. Nunes, J. Fehrenbach, G. Peyré, M. Bedossa, L. Luo, C. Toumoulin, *et al.* “Sparse reconstruction from a limited projection number of the coronary artery tree in X-ray rotational imaging”. In: *Proc. IEEE International Symposium on Biomedical Imaging (ISBI) 2012*, pp. 804–807, IEEE, 2012.
- [Huan 16] Y. Huang, O. Taubmann, X. Huang, V. Haase, G. Lauritsch, and A. Maier. “A new scale space total variation algorithm for limited angle tomography”. In: *Proc. 4th International Meeting on image formation in X-ray Computed Tomography*, pp. 149–52, 2016.

- [Husm 07] L. Husmann, I. Valenta, O. Gaemperli, O. Adda, V. Treyer, C. A. Wyss, P. Veit-Haibach, F. Tatsugami, G. K. von Schulthess, and P. A. Kaufmann. “Feasibility of low-dose coronary CT angiography: first experience with prospective ECG-gating”. *European Heart Journal*, 2007.
- [Jand 09] U. Jandt, D. Schäfer, M. Grass, and V. Rasche. “Automatic generation of 3D coronary artery centerlines using rotational X-ray angiography”. *Medical Image Analysis*, Vol. 13, No. 6, pp. 846–858, 2009.
- [Kak 01] A. C. Kak and M. Slaney. *Principles of computerized tomographic imaging*. Society for Industrial and Applied Mathematics, Philadelphia, PA, USA, 2001.
- [Keck 14] B. Keck. *High Performance Iterative X-Ray CT with Application in 3-D Mammography and Interventional C-arm Imaging Systems*. PhD thesis, Friedrich-Alexander-Universität Erlangen-Nürnberg, 2014.
- [Keil 09a] A. Keil, J. Vogel, G. Lauritsch, and N. Navab. “Dynamic cone-beam reconstruction using a variational level set formulation”. In: *Proc. Fully Three-Dimensional Image Reconstruction in Radiology and Nuclear Medicine*, pp. 323–326, 2009.
- [Keil 09b] A. Keil, J. Vogel, G. Lauritsch, and N. Navab. “Dynamic cone beam reconstruction using a new level set formulation”. In: *Proc. Medical Image Computing and Computer Assisted Intervention (MICCAI) 2009*, pp. 389–397, Springer, 2009.
- [Kerk 16] A. Kerkeni, A. Benabdallah, A. Manzanera, and M. H. Bedoui. “A coronary artery segmentation method based on multiscale analysis and region growing”. *Computerized Medical Imaging and Graphics*, Vol. 48, pp. 49–61, 2016.
- [Klei 11] A. J. Klein, J. A. Garcia, P. A. Hudson, M. S. Kim, J. C. Messenger, I. P. Casserly, O. Wink, B. Hattler, T. T. Tsai, S. Chen, *et al.* “Safety and efficacy of dual-axis rotational coronary angiography vs. standard coronary angiography”. *Catheterization and Cardiovascular Interventions*, Vol. 77, No. 6, pp. 820–827, 2011.
- [Klug 17] A. Klugmann, J. Fotouhi, B. Fuerst, K. Müller, A. Maier, and M. Unberath. “Automatic Respiratory Motion Correction for Liver Perfusion Imaging”. *Computerized Medical Imaging and Graphics*, 2017. (in preparation).
- [Kohl 14] R. Köhler, C. Schuler, B. Schölkopf, and S. Harmeling. “Mask-specific inpainting with deep neural networks”. In: *German Conference on Pattern Recognition*, pp. 523–534, Springer, 2014.
- [Koll 95] T. Koller, G. Gerig, G. Szekely, and D. Dettwiler. “Multiscale detection of curvilinear structures in 2-D and 3-D image data”. In: *IEEE International Conference on Computer Vision (ICCV) 1995*, pp. 864–869, IEEE, 1995.
- [Krus 56] J. B. Kruskal. “On the shortest spanning subtree of a graph and the traveling salesman problem”. *Proceedings of the American Mathematical Society*, Vol. 7, No. 1, pp. 48–50, 1956.
- [Land 94] C. Landau, R. A. Lange, and L. D. Hillis. “Percutaneous transluminal coronary angioplasty”. *New England Journal of Medicine*, Vol. 330, No. 14, pp. 981–993, 1994.

- [Laur 06] G. Lauritsch, J. Boese, L. Wigstrom, H. Kemeth, and R. Fahrig. “Towards cardiac C-arm computed tomography”. *IEEE Transactions on Medical Imaging*, Vol. 25, No. 7, pp. 922–934, 2006.
- [Lehm 06] G. C. Lehmann, D. W. Holdsworth, and M. Drangova. “Angle-independent measure of motion for image-based gating in 3D coronary angiography”. *Medical Physics*, Vol. 33, No. 5, pp. 1311–1320, 2006.
- [Li 02] M. Li, H. Yang, and H. Kudo. “An accurate iterative reconstruction algorithm for sparse objects: application to 3D blood vessel reconstruction from a limited number of projections”. *Physics in Medicine and Biology*, Vol. 47, No. 15, p. 2599, 2002.
- [Li 04] M. Li, H. Kudo, J. Hu, and R. H. Johnson. “Improved iterative algorithm for sparse object reconstruction and its performance evaluation with micro-CT data”. *IEEE Transactions on Nuclear Science*, Vol. 51, No. 3, pp. 659–666, 2004.
- [Li 07] T. Li, A. Koong, and L. Xing. “Enhanced 4D cone-beam CT with inter-phase motion model”. *Medical Physics*, Vol. 34, No. 9, p. 3688, 2007.
- [Li 11] J. Li and L. D. Cohen. “Reconstruction of 3D tubular structures from cone-beam projections”. In: *Proc. International Symposium on Biomedical Imagin (ISBI) 2011*, pp. 1162–1166, IEEE, 2011.
- [Liao 10] R. Liao, D. Luc, Y. Sun, and K. Kirchberg. “3-D reconstruction of the coronary artery tree from multiple views of a rotational X-ray angiography”. *The International Journal of Cardiovascular Imaging*, Vol. 26, No. 7, pp. 733–749, 2010.
- [Liu 14] B. Liu, F. Zhou, and X. Bai. “Improved C-arm cardiac cone beam CT based on alternate reconstruction and segmentation”. *Biomedical Signal Processing and Control*, Vol. 13, pp. 113–122, 2014.
- [Liu 15] X. Liu, F. Hou, A. Hao, and H. Qin. “A parallelized 4D reconstruction algorithm for vascular structures and motions based on energy optimization”. *The Visual Computer*, Vol. 31, No. 11, pp. 1431–1446, 2015.
- [Liu 16] B. Liu, X. Bai, and F. Zhou. “Local motion-compensated method for high-quality 3D coronary artery reconstruction”. *Biomedical Optics Express*, Vol. 7, No. 12, pp. 5268–5283, 2016.
- [Lu 15] Y. Lu, J. Geret, M. Unberath, M. Manhart, Q. Ren, R. Fahrig, J. Hornegger, and A. Maier. “Projection-based material decomposition by machine learning using image-based features for computed tomography”. In: *The 13th International Meeting on Fully Three-Dimensional Image Reconstruction in Radiology and Nuclear Medicine*, pp. 448–451, 2015.
- [Ludw 66] D. Ludwig. “The Radon transform on Euclidean space”. *Communications on Pure and Applied Mathematics*, Vol. 19, No. 1, pp. 49–81, 1966.
- [Lync 10] Lynch, Patrick J. “Coronary arteries”. [https://commons.wikimedia.org/wiki/File:Coronary\\_arteries.svg](https://commons.wikimedia.org/wiki/File:Coronary_arteries.svg), 2010. Accessed: 2017-02-28, licensed under Creative Commons Attribution-Share Alike 3.0 Unported.
- [Maas 09] C. Maaß, M. Baer, and M. Kachelrieß. “Image-based dual energy CT using optimized precorrection functions: A practical new approach of material decomposition in image domain”. *Medical Physics*, Vol. 36, No. 8, pp. 3818–3829, 2009.

- [Maas 14] N. Maass, F. Dennerlein, A. Aichert, and A. Maier. “Geometrical Jitter Correction in Computed Tomography”. In: F. Noo, Ed., *Proc. The Third International Meeting on image formation in X-ray Computed Tomography*, pp. 338–342, Jun 2014.
- [Maie 11] A. Maier, J.-H. Choi, A. Keil, C. Niebler, M. Sarmiento, A. Fieselmann, G. Gold, S. Delp, and R. Fahrig. “Analysis of vertical and horizontal circular C-arm trajectories”. In: *Proc. SPIE Medical Imaging*, p. 796123, International Society for Optics and Photonics, 2011.
- [Maie 12] A. Maier, B. Scholz, and F. Dennerlein. “Optimization-based extrapolation for truncation correction”. In: *Proc. 2th International Meeting on image formation in X-ray Computed Tomography*, pp. 390–394, 2012.
- [Maie 13] A. Maier, H. G. Hofmann, M. Berger, P. Fischer, C. Schwemmer, H. Wu, K. Müller, J. Hornegger, J.-H. Choi, C. Riess, *et al.* “CONRAD—A software framework for cone-beam imaging in radiology”. *Medical Physics*, Vol. 40, No. 11, 2013.
- [Maie 16] A. Maier and R. Fahrig. *GPU Denoising for Computed Tomography*, pp. 129–148. CRC Press, Boca Raton, FL, 1 Ed., 2016.
- [Mari 16] E. Marinetto, M. Brehler, A. Sisniega, Q. Cao, J. H. Stayman, J. Yorkston, J. H. Siewerdsen, and W. Zbijewski. “Quantification of bone microarchitecture in ultra-high resolution extremities cone-beam CT with a CMOS detector and compensation of patient motion”. In: *Proc. Computer Assisted Radiology and Surgery (CARS) 2016*, 2016.
- [Mazi 10] S. R. Mazin and N. J. Pelc. “Fourier properties of the fan-beam sinogram”. *Medical Physics*, Vol. 37, No. 4, pp. 1674–1680, Apr 2010.
- [McCl 13] J. McClelland, D. Hawkes, T. Schaeffter, and A. King. “Respiratory motion models: A review”. *Medical Image Analysis*, Vol. 17, No. 1, pp. 19–42, 2013.
- [McGi 08] H. C. McGill, C. A. McMahan, and S. S. Gidding. “Preventing heart disease in the 21st century”. *Circulation*, Vol. 117, No. 9, pp. 1216–1227, 2008.
- [Melt 05] T. Meltzer, C. Yanover, and Y. Weiss. “Globally optimal solutions for energy minimization in stereo vision using reweighted belief propagation”. In: *IEEE International Conference on Computer Vision (ICCV) 2005*, pp. 428–435, IEEE, 2005.
- [Mess 00] J. C. Messenger, S. J. Chen, J. D. Carroll, J. Burchenal, K. Kioussopoulos, and B. M. Groves. “3D coronary reconstruction from routine single-plane coronary angiograms: clinical validation and quantitative analysis of the right coronary artery in 100 patients”. *The International Journal of Cardiac Imaging*, Vol. 16, No. 6, pp. 413–427, 2000.
- [Mir 14] H. Mir, P. Xu, and P. Van Beek. “An extensive empirical evaluation of focus measures for digital photography”. In: *Proc. SPIE Electronic Imaging*, pp. 90230I–90230I, International Society for Optics and Photonics, 2014.
- [Mohr 13] F. W. Mohr, M.-C. Morice, A. P. Kappetein, T. E. Feldman, E. Ståhle, A. Colombo, M. J. Mack, D. R. Holmes, M.-a. Morel, N. Van Dyck, *et al.* “Coronary artery bypass graft surgery versus percutaneous coronary

- intervention in patients with three-vessel disease and left main coronary disease: 5-year follow-up of the randomised, clinical SYNTAX trial”. *The Lancet*, Vol. 381, No. 9867, pp. 629–638, 2013.
- [Mova 07] B. Movassaghi, M. Grass, D. Schaefer, V. Rasche, O. Wink, G. Schoonenberg, J. Chen, J. Garcia, B. Groves, J. Messenger, *et al.* “4D coronary artery reconstruction based on retrospectively gated rotational angiography: First in-human results”. In: *Proc. SPIE Medical Imaging*, pp. 65090P–65090P, International Society for Optics and Photonics, 2007.
- [Moza 16] D. Mozaffarian, E. J. Benjamin, A. S. Go, D. K. Arnett, M. J. Blaha, M. Cushman, S. R. Das, S. de Ferranti, J.-P. Després, H. J. Fullerton, *et al.* “Heart disease and stroke statistic – 2016 update”. *Circulation*, Vol. 133, No. 4, pp. e38–e360, 2016.
- [Mull 16] K. Müller, M. Ahmad, M. Spahn, J.-H. Choi, S. Reitz, N. Köster, Y. Lu, R. Fahrig, and A. Maier. “Towards material decomposition on large field-of-view flat panel photon-counting detectors—First in-vivo results”. In: *Proc. 4th International Meeting on image formation in X-ray Computed Tomography*, pp. 479–482, 2016.
- [Naka 11] S. Nakatani. “Left Ventricular Rotation and Twist: Why Should We Learn?”. *Journal of Cardiovascular Ultrasound*, Vol. 19, No. 1, pp. 1–6, 2011.
- [Nati 16] National Heart, Lung, and Blood Institute (NIH NHLBI). “What Is Atherosclerosis?”. <https://www.nhlbi.nih.gov/health/health-topics/topics/atherosclerosis/signs>, 2016. Accessed: 2017-02-28.
- [Natt 86] F. Natterer. *The Mathematics of Computerized Tomography*. Springer, Berlin, Germany, 1986.
- [Neja 14] M. Nejati and H. Pourghassem. “Multiresolution image registration in digital X-Ray angiography with intensity variation modeling”. *Journal of medical systems*, Vol. 38, No. 2, p. 10, 2014.
- [Ohne 00] B. Ohnesorge, T. Flohr, K. Schwarz, J. Heiken, and K. Bae. “Efficient correction for CT image artifacts caused by objects extending outside the scan field of view”. *Medical Physics*, Vol. 27, No. 1, pp. 39–46, 2000.
- [Orth 08] R. C. Orth, M. J. Wallace, M. D. Kuo, T. A. C. of the Society of Interventional Radiology, *et al.* “C-arm cone-beam CT: general principles and technical considerations for use in interventional radiology”. *Journal of Vascular and Interventional Radiology*, Vol. 19, No. 6, pp. 814–820, 2008.
- [Ostc 11] Y. Ostchega, K. S. Porter, J. Hughes, C. F. Dillon, and T. Nwankwo. *Resting pulse rate reference data for children, adolescents, and adults: United States, 1999-2008*. US Department of Health and Human Services, Centers for Disease Control and Prevention, National Center for Health Statistics, 2011.
- [Pack 04] J. D. Pack, F. Noo, and H. Kudo. “Investigation of saddle trajectories for cardiac CT imaging in cone-beam geometry”. *Physics in Medicine and Biology*, Vol. 49, No. 11, p. 2317, 2004.
- [Park 82] D. L. Parker. “Optimal short scan convolution reconstruction for fan beam CT”. *Medical Physics*, Vol. 9, No. 2, pp. 254–257, 1982.

- [Poly 12] M. Polyanskayaa, C. Schwemmera, A. Linartha, G. Lauritschb, and J. Horneggera. “Robust lumen segmentation of coronary arteries in 2D angiographic images”. In: *Proc. SPIE Medical Imaging*, pp. 83142N–83142N, International Society for Optics and Photonics, 2012.
- [Pour 16] A. Pourmorteza, H. Dang, J. Siewerdsen, and J. W. Stayman. “Reconstruction of difference in sequential CT studies using penalized likelihood estimation”. *Physics in Medicine and Biology*, Vol. 61, No. 5, p. 1986, 2016.
- [Pras 09] H. Prashanth, H. Shashidhara, and B. M. KN. “Image scaling comparison using universal image quality index”. In: *Advances in Computing, Control, & Telecommunication Technologies, 2009. International Conference on*, pp. 859–863, IEEE, 2009.
- [Prum 06] M. Prümmer, L. Wigstroem, J. Hornegger, J. Boese, G. Lauritsch, N. Strobel, and R. Fahrig. “Cardiac C-arm CT: Efficient Motion Correction for 4D-FBP”. In: *IEEE Nuclear Science Symposium Conference Record (NSS) 2006*, pp. 2620–2628, 2006.
- [Rama 71] G. Ramachandran and A. Lakshminarayanan. “Three-dimensional reconstruction from radiographs and electron micrographs: application of convolutions instead of Fourier transforms”. *Proceedings of the National Academy of Sciences*, Vol. 68, No. 9, pp. 2236–2240, 1971.
- [Rasc 06a] V. Rasche, B. Movassaghi, M. Grass, D. Schäfer, and A. Buecker. “Automatic selection of the optimal cardiac phase for gated three-dimensional coronary X-ray angiography”. *Academic Radiology*, Vol. 13, No. 5, pp. 630–640, 2006.
- [Rasc 06b] V. Rasche, B. Movassaghi, M. Grass, D. Schäfer, H. P. Köhl, R. W. Günther, and A. Buecker. “Three-dimensional X-ray coronary angiography in the porcine model: A feasibility study”. *Academic Radiology*, Vol. 13, No. 5, pp. 644–651, 2006.
- [Ries 13] C. Riess, M. Berger, H. Wu, M. Manhart, R. Fahrig, and A. Maier. “TV or not TV? That is the question”. *Proc. Fully Three-Dimensional Image Reconstruction in Radiology and Nuclear Medicine*, pp. 341–344, 2013.
- [Ries 16] C. Riess, M. Unberath, F. Naderi, S. Pfaller, M. Stamminger, and E. Angelopoulou. “Handling multiple materials for exposure of digital forgeries using 2-D lighting environments”. *Multimedia Tools and Applications*, pp. 1–18, 2016.
- [Rit 09a] S. Rit, M. van Herk, and J.-J. Sonke. “Fast distance-driven projection and truncation management for iterative cone-beam CT reconstruction”. In: *Proc. International Meeting on Fully Three-Dimensional Image Reconstruction in Radiology Nuclear Medicine*, pp. 49–52, 2009.
- [Rit 09b] S. Rit, J. W. Wolthaus, M. van Herk, and J.-J. Sonke. “On-the-fly motion-compensated cone-beam CT using an a priori model of the respiratory motion”. *Medical Physics*, Vol. 36, No. 6, pp. 2283–2296, 2009.
- [Rits 11] L. Ritschl, F. Bergner, C. Fleischmann, and M. Kachelrieß. “Improved total variation-based CT image reconstruction applied to clinical data”. *Physics in Medicine and Biology*, Vol. 56, No. 6, p. 1545, 2011.



- [Rodr 13] A. Rodríguez-Molinero, L. Narvaiza, J. Ruiz, and C. Gálvez-Barrón. “Normal respiratory rate and peripheral blood oxygen saturation in the elderly population”. *Journal of the American Geriatrics Society*, Vol. 61, No. 12, pp. 2238–2240, 2013.
- [Roes 07] E. Roessl and R. Proksa. “K-edge imaging in x-ray computed tomography using multi-bin photon counting detectors”. *Physics in Medicine and Biology*, Vol. 52, No. 15, p. 4679, 2007.
- [Rohk 08] C. Rohkohl, G. Lauritsch, A. Nottling, M. Prummer, and J. Hornegger. “C-arm ct: Reconstruction of dynamic high contrast objects applied to the coronary sinus”. In: *IEEE Nuclear Science Symposium Conference Record (NSS) 2008*, pp. 5113–5120, IEEE, 2008.
- [Rohk 09] C. Rohkohl, G. Lauritsch, M. Prümmer, and J. Hornegger. “Interventional 4-D motion estimation and reconstruction of cardiac vasculature without motion periodicity assumption”. In: *Proc. Medical Image Computing and Computer-Assisted Intervention (MICCAI) 2009*, pp. 132–139, Springer, 2009.
- [Rohk 10a] C. Rohkohl, G. Lauritsch, L. Biller, and J. Hornegger. “ECG-Gated Cardiac Reconstruction for Non-Periodic Motion”. In: *Proc. 1st International Meeting on image formation in X-ray Computed Tomography*, pp. 272–275, 2010.
- [Rohk 10b] C. Rohkohl, G. Lauritsch, L. Biller, M. Prümmer, J. Boese, and J. Hornegger. “Interventional 4D motion estimation and reconstruction of cardiac vasculature without motion periodicity assumption”. *Medical Image Analysis*, Vol. 14, No. 5, pp. 687–694, 2010.
- [Rohk 10c] C. Rohkohl, G. Lauritsch, A. Keil, and J. Hornegger. “CAVAREV—an open platform for evaluating 3D and 4D cardiac vasculature reconstruction”. *Physics in Medicine and Biology*, Vol. 55, No. 10, p. 2905, 2010.
- [Rohk 11] C. Rohkohl. *Motion Estimation and Compensation for Interventional Cardiovascular Image Reconstruction*. PhD thesis, Friedrich-Alexander-Universität Erlangen-Nürnberg, 2011.
- [Rohk 17] C. Rohkohl. “CArdiac VASculature Reconstruction EValuation, Score-board”. <https://www5.cs.fau.de/research/software/cavarev/>, 2017. Accessed: 2017-03-14.
- [Romh 68] D. W. Romhilt and E. H. Estes. “A point-score system for the ECG diagnosis of left ventricular hypertrophy”. *American Heart Journal*, Vol. 75, No. 6, pp. 752–758, 1968.
- [Rooi 08] W. J. van Rooij, M. Sprengers, A. N. de Gast, J. Peluso, and M. Sluzewski. “3D rotational angiography: the new gold standard in the detection of additional intracranial aneurysms”. *American Journal of Neuroradiology*, Vol. 29, No. 5, pp. 976–979, 2008.
- [Sand 16] J. Sanders, P. Ritt, T. Kuwert, A. H. Vija, and A. Maier. “Fully Automated Data-Driven Respiratory Signal Extraction from SPECT Images Using Laplacian Eigenmaps”. *IEEE Transactions on Medical Imaging*, Vol. 35, No. 11, pp. 2425–2435, 2016.



- [Scha 06] D. Schafer, J. Borgert, V. Rasche, and M. Grass. “Motion-compensated and gated cone beam filtered back-projection for 3-D rotational X-ray angiography”. *IEEE Transactions on Medical Imaging*, Vol. 25, No. 7, pp. 898–906, 2006.
- [Scha 09] M. Schaap, C. T. Metz, T. van Walsum, A. G. van der Giessen, A. C. Weustink, N. R. Mollet, C. Bauer, H. Bogunović, C. Castro, X. Deng, *et al.* “Standardized evaluation methodology and reference database for evaluating coronary artery centerline extraction algorithms”. *Medical Image Analysis*, Vol. 13, No. 5, pp. 701–714, 2009.
- [Sche 07] H. Scherl, B. Keck, M. Kowarschik, and J. Hornegger. “Fast GPU-based CT reconstruction using the common unified device architecture (CUDA)”. In: *Nuclear Science Symposium Conference Record, 2007. IEEE*, pp. 4464–4466, IEEE, 2007.
- [Sche 16] F. Schebesch, M. Unberath, I. Andersen, and A. Maier. “Breast Density Assessment Using Wavelet Features on Mammograms”. In: *Bildverarbeitung für die Medizin 2016*, pp. 38–43, Springer, 2016.
- [Schi 17] F. Schirrmacher, O. Taubmann, M. Unberath, and A. Maier. “Towards Understanding Preservation of Periodic Object Motion in Computed Tomography”. In: *Bildverarbeitung für die Medizin 2017*, pp. 116–121, Springer, 2017.
- [Scho 09] G. A. Schoonenberg, J. A. Garcia, and J. D. Carroll. “Left coronary artery thrombus characterized by a fully automatic three-dimensional gated reconstruction”. *Catheterization and Cardiovascular Interventions*, Vol. 74, No. 1, pp. 97–100, 2009.
- [Schw 13a] C. Schwemmer, C. Rohkohl, G. Lauritsch, K. Müller, and J. Hornegger. “Residual motion compensation in ECG-gated interventional cardiac vasculature reconstruction”. *Physics in Medicine and Biology*, Vol. 58, No. 11, p. 3717, 2013.
- [Schw 13b] C. Schwemmer, C. Rohkohl, G. Lauritsch, K. Müller, J. Hornegger, and J. Qi. “Opening windows: increasing window size in motion-compensated ECG-gated cardiac vasculature reconstruction”. In: *Proc. International Meeting on Fully Three-Dimensional Image Reconstruction in Radiology Nuclear Medicine*, pp. 50–53, 2013.
- [Sega 01] W. P. Segars, B. Tsui, D. Lalush, E. Frey, M. King, and D. Manocha. “Development and application of the new dynamic Nurbs-based Cardiac-Torso (NCAT) phantom”. 2001.
- [Sega 08] W. P. Segars, M. Mahesh, T. J. Beck, E. C. Frey, and B. M. Tsui. “Realistic CT simulation using the 4D XCAT phantom”. *Medical Physics*, Vol. 35, No. 8, pp. 3800–3808, 2008.
- [Serr 06] P. W. Serruys, M. J. Kutryk, and A. T. Ong. “Coronary-artery stents”. *New England Journal of Medicine*, Vol. 354, No. 5, pp. 483–495, 2006.
- [Shec 03] G. Shechter, F. Devernay, E. Coste-Manière, A. Quyyumi, and E. R. McVeigh. “Three-dimensional motion tracking of coronary arteries in biplane cineangiograms”. *IEEE Transactions on Medical Imaging*, Vol. 22, No. 4, pp. 493–503, 2003.

- [Shec 04] G. Shechter, C. Ozturk, J. R. Resar, and E. R. McVeigh. “Respiratory motion of the heart from free breathing coronary angiograms”. *IEEE Transactions on Medical Imaging*, Vol. 23, No. 8, pp. 1046–1056, 2004.
- [Shec 06] G. Shechter, J. R. Resar, and E. R. McVeigh. “Displacement and velocity of the coronary arteries: cardiac and respiratory motion”. *IEEE Transactions on Medical Imaging*, Vol. 25, No. 3, pp. 369–375, 2006.
- [Sidk 06] E. Y. Sidky, C.-M. Kao, and X. Pan. “Accurate image reconstruction from few-views and limited-angle data in divergent-beam CT”. *Journal of X-ray Science and Technology*, Vol. 14, No. 2, pp. 119–139, 2006.
- [Sidk 08] E. Y. Sidky and X. Pan. “Image reconstruction in circular cone-beam computed tomography by constrained, total-variation minimization”. *Physics in Medicine and Biology*, Vol. 53, No. 17, p. 4777, 2008.
- [Siem 14] Siemens Healthcare GmbH. “Data Sheet VC21, Artis zeego”. <http://www.deltamedicalsystems.com/DeltaMedicalSystems/media/Product-Details/Artis-zeego-Data-Sheet.pdf>, 2014. Accessed: 2017-02-13.
- [Siem 17] Siemens Healthcare GmbH. “syngo DynaCT, Technical Details”. <https://www.healthcare.siemens.com/angio/options-and-upgrades/clinical-software-applications/syngo-dynact/technical-details>, 2017. Accessed: 2017-02-11.
- [Siew 05] J. Siewerdsen, D. Moseley, S. Burch, S. Bisland, A. Bogaards, B. Wilson, and D. Jaffray. “Volume CT with a flat-panel detector on a mobile, isocentric C-arm: Pre-clinical investigation in guidance of minimally invasive surgery”. *Medical Physics*, Vol. 32, No. 1, pp. 241–254, 2005.
- [Sisn 16a] A. Sisniega, J. W. Stayman, Q. Cao, J. Yorkston, J. H. Siewerdsen, and W. Zbijewski. “Motion estimation using a penalized image sharpness criterion for resolution recovery in extremities cone-beam CT”. In: *Proc. 4th International Meeting on Image Formation in X-ray CT*, pp. 549–52, 2016.
- [Sisn 16b] A. Sisniega, J. Stayman, Q. Cao, J. Yorkston, J. Siewerdsen, and W. Zbijewski. “Image-based motion compensation for high-resolution extremities cone-beam CT”. In: *Proc. SPIE Medical Imaging*, p. 97830K, International Society for Optics and Photonics, 2016.
- [Soil 04] P. Soille. “Filtering”. In: *Morphological Image Analysis*, pp. 241–265, Springer, 2004.
- [Song 07] J. Song, Q. H. Liu, G. A. Johnson, and C. T. Badea. “Sparseness prior based iterative image reconstruction for retrospectively gated cardiac micro-CT”. *Medical Physics*, Vol. 34, No. 11, pp. 4476–4483, 2007.
- [Sonk 05] J.-J. Sonke, L. Zijp, P. Remeijer, and M. van Herk. “Respiratory correlated cone beam CT”. *Medical Physics*, Vol. 32, No. 4, p. 1176, 2005.
- [Sore 48] T. Sørensen. “A method of establishing groups of equal amplitude in plant sociology based on similarity of species and its application to analyses of the vegetation on Danish commons”. *Biologiske Skrifter*, Vol. 5, pp. 1–34, 1948.

- [Sour 05] K. Sourbelle, M. Kachelrieß, and W. A. Kalender. “Reconstruction from truncated projections in CT using adaptive detruncation”. *European radiology*, Vol. 15, No. 5, pp. 1008–1014, 2005.
- [Stay 12] J. W. Stayman, Y. Otake, J. L. Prince, A. J. Khanna, and J. H. Siewerdsen. “Model-based tomographic reconstruction of objects containing known components”. *IEEE Transactions on Medical Imaging*, Vol. 31, No. 10, pp. 1837–1848, 2012.
- [Stim 17a] B. Stimpel, M. Unberath, J. Wetzl, M. Schmidt, A. Maier, and C. Forman. “Automatic Coronary Artery Ostia Detection in Magnetic Resonance Angiography”. In: *International Society for Magnetic Resonance in Medicine (ISMRM), Annual Meeting & Exhibition*, 2017. (to appear).
- [Stim 17b] B. Stimpel, J. Wetzl, C. Forman, A. Maier, M. Schmidt, and M. Unberath. “Automated Reformation of the Proximal Coronary Arteries in MR Angiography”. *IEEE Transactions on Medical Imaging*, 2017. (under review).
- [Tagu 08] K. Taguchi and H. Kudo. “A simple motion tracking backprojection for a class of affine transformation”. In: *Proc. SPIE Medical Imaging*, pp. 69131V–69131V, International Society for Optics and Photonics, 2008.
- [Tagu 13] K. Taguchi and J. S. Iwanczyk. “Vision 20/20: Single photon counting x-ray detectors in medical imaging”. *Medical Physics*, Vol. 40, No. 10, 2013.
- [Taub 16] O. Taubmann, G. Lauritsch, G. Krings, and A. Maier. “Convex temporal regularizers in cardiac C-arm CT”. In: *Proc. 4th International Meeting on image formation in X-ray Computed Tomography*, pp. 545–8, 2016.
- [Taub 17a] O. Taubmann, V. Haase, G. Lauritsch, Y. Zheng, G. Krings, J. Hornegger, and A. Maier. “Assessing Cardiac Function from Total-Variation-Regularized 4-D C-arm CT in the Presence of Angular Undersampling”. *Physics in Medicine and Biology*, 2017. (in press).
- [Taub 17b] O. Taubmann, G. Lauritsch, G. Krings, and A. Maier. “Background Matters: A Correction Scheme for Dynamic Iterative CBCT with Limited Grid Size”. In: *Proc. International Meeting on Fully Three-Dimensional Image Reconstruction in Radiology Nuclear Medicine*, 2017. (under review).
- [Taub 17c] O. Taubmann, M. Unberath, G. Lauritsch, S. Achenbach, and A. Maier. “Spatio-temporally regularized 4-D Cardiovascular C-arm CT Reconstruction Using a Proximal Algorithm”. In: *Proc. International Symposium on Biomedical Imaging (ISBI) 2017*, 2017. (to appear).
- [Toma 98] C. Tomasi and R. Manduchi. “Bilateral filtering for gray and color images”. In: *IEEE International Conference on Computer Vision (ICCV) 1998*, pp. 839–846, IEEE, 1998.
- [Tuy 83] H. K. Tuy. “An inversion formula for cone-beam reconstruction”. *SIAM Journal on Applied Mathematics*, Vol. 43, No. 3, pp. 546–552, 1983.
- [Unbe 15a] M. Unberath, J.-H. Choi, M. Berger, A. Maier, and R. Fahrig. “Image-based compensation for involuntary motion in weight-bearing C-arm cone-beam CT scanning of knees”. In: *Proc. SPIE Medical Imaging*,

- pp. 94130D–94130D, International Society for Optics and Photonics, 2015.
- [Unbe 15b] M. Unberath, A. Maier, D. Fleischmann, J. Hornegger, and R. Fahrig. “Open-source 4D statistical shape model of the heart for x-ray projection imaging”. In: *Proc. International Symposium on Biomedical Imaging (ISBI) 2015*, pp. 739–742, IEEE, 2015.
  - [Unbe 15c] M. Unberath, K. Mentl, O. Taubmann, S. Achenbach, R. Fahrig, J. Hornegger, and A. Maier. “Torsional heart motion in cone-beam computed tomography reconstruction”. In: *Proc. International Meeting on Fully Three-Dimensional Image Reconstruction in Radiology Nuclear Medicine*, pp. 651–654, 2015.
  - [Unbe 16a] M. Unberath, S. Achenbach, and A. Maier. “Exhaustive Graph Cut-based Vasculature Reconstruction”. In: *Proc. International Symposium on Biomedical Imaging (ISBI) 2016*, pp. 1143–1146, 2016.
  - [Unbe 16b] M. Unberath, A. Aichert, S. Achenbach, and A. Maier. “Improving Segmentation Quality in Rotational Angiography Using Epipolar Consistency”. In: *Joint MICCAI workshops on Computing and Visualisation for Intravascular Imaging and Computer-Assisted Stenting*, 2016.
  - [Unbe 16c] M. Unberath, A. Aichert, S. Achenbach, and A. Maier. “Virtual Single-frame Subtraction Imaging”. In: *Proc. 4th International Meeting on image formation in X-ray Computed Tomography*, pp. 89–92, 2016.
  - [Unbe 16d] M. Unberath, E. Goppert, O. Taubmann, and A. Maier. “Mitigating Medialness Responses from Non-tubular Structures Using Entropy”. In: *Computer Assisted Radiology and Surgery (CARS) 2016, Congress and Exhibition*, pp. 211–212, 2016.
  - [Unbe 17a] M. Unberath, A. Aichert, S. Achenbach, and A. Maier. “Consistency-based Respiratory Motion Estimation in Rotational Angiography”. *Medical Physics*, 2017. (in press).
  - [Unbe 17b] M. Unberath, M. Berger, A. Aichert, and A. Maier. “Fourier Consistency-Based Motion Estimation in Rotational Angiography”. In: *Bildverarbeitung für die Medizin 2017*, pp. 110–115, Springer, 2017.
  - [Unbe 17c] M. Unberath, O. Taubmann, S. Achenbach, and A. Maier. “Prior-free Respiratory Motion Estimation in Rotational Angiography”. *IEEE Transactions on Medical Imaging*, 2017. (in preparation).
  - [Unbe 17d] M. Unberath, O. Taubmann, B. Bier, T. Geimer, M. Hell, S. Achenbach, and A. Maier. “Respiratory Motion Compensation in Rotational Angiography: Graphical Model-based Optimization of Auto-focus Measures”. In: *Proc. International Symposium on Biomedical Imaging (ISBI) 2017*, 2017. (to appear).
  - [Unbe 17e] M. Unberath, O. Taubmann, M. Hell, S. Achenbach, and A. Maier. “Symmetry, Outliers, and Geodesics in Coronary Artery Centerline Reconstruction from Rotational Angiography”. *Medical Physics*, 2017. (under revision).
  - [Veks 99] O. Veksler. *Efficient graph-based energy minimization methods in computer vision*. PhD thesis, Cornell University, 1999.

- [Wall 07] M. J. Wallace, R. Murthy, P. P. Kamat, T. Moore, S. H. Rao, J. Ensor, S. Gupta, K. Ahrar, D. C. Madoff, S. E. McRae, *et al.* “Impact of C-arm CT on hepatic arterial interventions for hepatic malignancies”. *Journal of Vascular and Interventional Radiology*, Vol. 18, No. 12, pp. 1500–1507, 2007.
- [Wall 08] M. J. Wallace, M. D. Kuo, C. Glaiberman, C. A. Binkert, R. C. Orth, G. Soulez, T. A. C. of the Society of Interventional Radiology, *et al.* “Three-dimensional C-arm cone-beam CT: applications in the interventional suite”. *Journal of Vascular and Interventional Radiology*, Vol. 19, No. 6, pp. 799–813, 2008.
- [Wang 95] Y. Wang, S. J. Riederer, and R. L. Ehman. “Respiratory motion of the heart: kinematics and the implications for the spatial resolution in coronary imaging”. *Magnetic Resonance in Medicine*, Vol. 33, No. 5, pp. 713–719, 1995.
- [Wang 99] Y. Wang, E. Vidan, and G. W. Bergman. “Cardiac Motion of Coronary Arteries: Variability in the Rest Period and Implications for Coronary MR Angiography 1”. *Radiology*, Vol. 213, No. 3, pp. 751–758, 1999.
- [Wick 12] J. Wicklein, H. Kunze, W. A. Kalender, and Y. Kyriakou. “Image features for misalignment correction in medical flat-detector CT”. *Medical Physics*, Vol. 39, No. 8, pp. 4918–4931, 2012.
- [Worl 16] World Health Organization. “Cardiovascular diseases, Fact sheet”. <http://www.who.int/mediacentre/factsheets/fs317/en/>, 2016. Accessed: 2017-02-28.
- [Wu 11] H. Wu, C. Rohkohl, and J. Hornegger. “Total variation regularization method for 3D rotational coronary angiography”. In: *Bildverarbeitung für die Medizin 2011*, pp. 434–438, Springer, 2011.
- [Wu 16] H. Wu, M. Berger, A. Maier, and D. Lohmann. “A Memory Management Library for CT-Reconstruction on GPUs”. In: *Bildverarbeitung für die Medizin 2016*, pp. 206–211, Springer, 2016.
- [Xia 14] Y. Xia, H. Hofmann, F. Dennerlein, K. Müller, C. Schwemmer, S. Bauer, G. Chintalapani, P. Chinnadurai, J. Hornegger, and A. Maier. “Towards Clinical Application of a Laplace Operator-based Region of Interest Reconstruction Algorithm in C-arm CT”. *IEEE Transactions on Medical Imaging*, Vol. 33, No. 3, pp. 593–606, 2014.
- [Xia 15] Y. Xia, S. Bauer, A. Maier, M. Berger, and J. Hornegger. “Patient-bounded extrapolation using low-dose priors for volume-of-interest imaging in C-arm CT”. *Medical Physics*, Vol. 42, No. 4, pp. 1787–1796, 2015.
- [Xie 12] J. Xie, L. Xu, and E. Chen. “Image denoising and inpainting with deep neural networks”. In: *Advances in Neural Information Processing Systems*, pp. 341–349, 2012.
- [Yi 17] H. J. Yi, J. H. Sung, D. H. Lee, S. W. Kim, and S. W. Lee. “Analysis of radiation doses and dose reduction strategies during cerebral digital subtraction angiography”. *World Neurosurgery*, 2017.
- [Zbij 06] W. Zbijewski and F. J. Beekman. “Efficient Monte Carlo based scatter artifact reduction in cone-beam micro-CT”. *IEEE Transactions on Medical Imaging*, Vol. 25, No. 7, pp. 817–827, 2006.

- [Zeng 10] G. L. Zeng. *Medical Image Reconstruction: A Conceptual Tutorial*. Springer Berlin Heidelberg, 1 Ed., 2010.
- [Zeng 14] G. L. Zeng. “Noise-weighted spatial domain FBP algorithm”. *Medical Physics*, Vol. 41, No. 5, 2014.
- [Zhou 08] J. Zhou, A. Bousse, G. Yang, J.-J. Bellanger, L. Luo, C. Toumoulin, and J.-L. Coatrieux. “A blob-based tomographic reconstruction of 3D coronary trees from rotational X-ray angiography”. In: *Proc. SPIE Medical Imaging*, pp. 69132N–69132N, International Society for Optics and Photonics, 2008.
- [Zijp 04] L. Zijp, J.-J. Sonke, and M. van Herk. “Extraction of the respiratory signal from sequential thorax cone-beam X-ray images”. In: *Proc. International Conference on the Use of Computers in Radiation Therapy*, pp. 507–509, 2004.
- [Zink 10] M. Zinkevich, M. Weimer, L. Li, and A. J. Smola. “Parallelized stochastic gradient descent”. In: *Advances in Neural Information Processing Systems*, pp. 2595–2603, 2010.